Mechatronic Design and Feedback Control for Quality-assured Laser Powder Bed Fusion Additive Manufacturing

Tianyu Jiang

A dissertation
submitted in partial fulfillment of the
requirements for the degree of

Doctor of Philosophy

University of Washington

2021

Reading Committee:

Xu Chen, Chair

Santosh Devasia

Ramulu Mamidala

Program Authorized to Offer Degree:

Mechanical Engineering

University of Washington

Abstract

Mechatronic Design and Feedback Control for Quality-assured Laser Powder Bed Fusion Additive Manufacturing

Tianyu Jiang

Chair of the Supervisory Committee:
Associate Professor Xu Chen
Department of Mechanical Engineering

Despite continuous technological enhancements and emerging applications of laser powder bed fusion (LPBF) additive manufacturing, the lack of repeatability and stability still represents a barrier to industrial breakthrough. This dissertation developed new mechatronic design of process monitoring and capabilities of robust control to reduce process variation and ensure part quality.

By building a sensor-rich feedback-centric LPBF platform, this study enables access to crucial process signatures (e.g., powder bed temperature, melting pool image) and manipulation of various process parameters (e.g., heater power, scan velocity) to provide the opportunity for model-based controls.

Leveraging the established mechatronic design, we investigated control algorithms and data interpretation frameworks for attenuating mechanical vibrations, thermal transfer fluctuations, and laser-material interaction imperfections. Specifically:

- We introduced a model-inverse free local loop shaping control for disturbance rejection in the laser scanning process. We proposed and verified filter designs for attenuating both narrow- and broad-band vibrations in the position output of the scanner, leading to higher accuracy of part geometry.

- We proposed a model-based multi-zone heating control algorithm for minimizing the powder

bed temperature deviation in the presence of part-geometry induced cross-layer thermal disturbance, leading to a more homogeneous part mechanical property.

- We created an image analytics framework for defect identification, part quality evaluation, and process signature filtering, which paves the road towards online implementable laser-material interaction control.

NOMENCLATURE

3D: three dimensional

AM: additive manufacturing

API: application programming interface

CAD: computer-aided design

CLAHE: contrast-limited adaptive histogram equalization

DAC: digital analog converter

DC: direct current

DOB: disturbance observer

FFC: flat-field correction

FIR: finite impulse response

FMSDOB: forward model selective disturbance observer

FOV: field of view

FPGA: field-programmable gate array

GUI: graphical user interface

HAZ: heat-affected zone

IR: infrared

LLS: local loop shaping

LTI: linear time invariant

LPBF: laser powder bed fusion

MPC: model predictive control

PA: polyamide

PAA: parameter adaptation algorithm

PC: polycarbonateand

PCA: principal component analysis

PCL: polycaprolactone

PEEK: polyetheretherketone

PID: proportional-integral-derivative

PWM: pulse-width modulation

ROI: region of interest

RTD: resistance temperature detector

SE: structuring element

YK: Youla-Kucera

TABLE OF CONTENTS

LIST OF FIGURES

LIST OF TABLES

ACKNOWLEDGMENTS

First and foremost, I would like to express my sincere gratitude and respect to my major academic advisor Prof. Xu Chen. I appreciate his guidance, patience, encouragement, and support for my graduate career. His immense knowledge, insightful advice, and meticulous scrutiny have helped to a very great extent to accomplish this work. Under the advisement of Prof. Chen over these years, I have learned things that benefit my academic research and positively affect my attitude towards the challenges and barriers in real life. This is a most rewarding experience, which I will cherish and preserve in my mind. I am also extending my hearty thanks to his family for the holiday gatherings and numerous warm gifts.

I would like to express my gratitude to my associated academic advisors, Prof. Santosh Devasia, Prof. Ramulu Mamidala, Prof. Dwayne Arola, and Prof. Jennifer Mankoff, for their precious time serving on my committee. Their keen insight, helpful advice, and critiques on my research project give tremendous value to me. Special thanks to Prof. Jennifer Mankoff for accepting my invitation under health conditions. I am also thankful for Prof. Tang Jiong, who gave me great suggestions on this dissertation. I would like to acknowledge the National Science Foundation, GE Fellowship for Innovation for generously supporting this study.

I thank the following former and current labmates in the Mechatronics, Automation, and Control Systems Laboratory, for their support during the time we were together – Dan Wang, Hui Xiao, Feifei Yang, and Thomas Chu. Also, it has been a pleasure for me to mentor and work with the master and undergraduate students Thomas Chessman, Mengying Leng, Jinghao Chen, Hongkuan Lin, and Jason Xie.

Last but not least, I would express my greatest gratitude to my parents Yanqing Zhang and Ruihua Jiang for their unconditional love and constant support. Profound thanks to Tong Shen for

her company, support, and love along this journey. Thank my cat Sphynx for bringing enormous happiness to my life. Also, thanks to all my other friends at the University of Connecticut and the University of Washington. May our friendship lasts forever. My sincere thanks also go to Liting Sun for referring me to this Ph.D. program.

Chapter 1

INTRODUCTION

Laser Powder bed fusion (LPBF) is one of the additive manufacturing (AM) (also known as 3D printing) processes, where 3D objects are built from thin layers of materials. During the processing of each layer, a high-power laser moves along predefined trajectories at several meters per second to sinter/melt the powder particles (Fig. 1.1(a)). After consolidation, the powder bed is lowered by the thickness of a thin layer. New powders are then spread over the current deposit via a powder deposition system (a.k.a. recoater) to start the next repetition (Fig. 1.1(b)).

Since its first invention and commercialization, LPBF has demonstrated a wide range of competitive advantages over conventional manufacturing methods. For instance, LPBF can process a broad range of materials (including polymers, metals, ceramics, and composites) [4], and can create parts with complex features at reduced weight [5, 6]. Despite such capabilities and countless emerging applications, limited reliability and reproducibility are hindering broader adoption of this manufacturing technology, especially in such industries as medical device manufacturing and aviation. LPBF process is susceptible to disturbances such as external vibrations, environmental temperature fluctuations, process byproducts (fumes and spatters), and imperfect laser-material interactions [7–9]. Unpredictable process variations can result in various part defects, including excessive porosity, high surface roughness, thermal cracking and delamination, geometric error, microstructural inhomogeneity, etc. [10]. As a result, the same part can come out differently from different machines or even from the same machine on a different day. Indeed, reducing variability in quality metrics has been recognized as a major need to advance AM technologies [7, 11, 12].

A well-recognized solution to address quality assurance is the development of effective real-time monitoring and closed-loop feedback control [13]. It would be ideal to be able to monitor part quality, detect defect formations, and make corrections or repairs as a part is being built [7, 14]. To

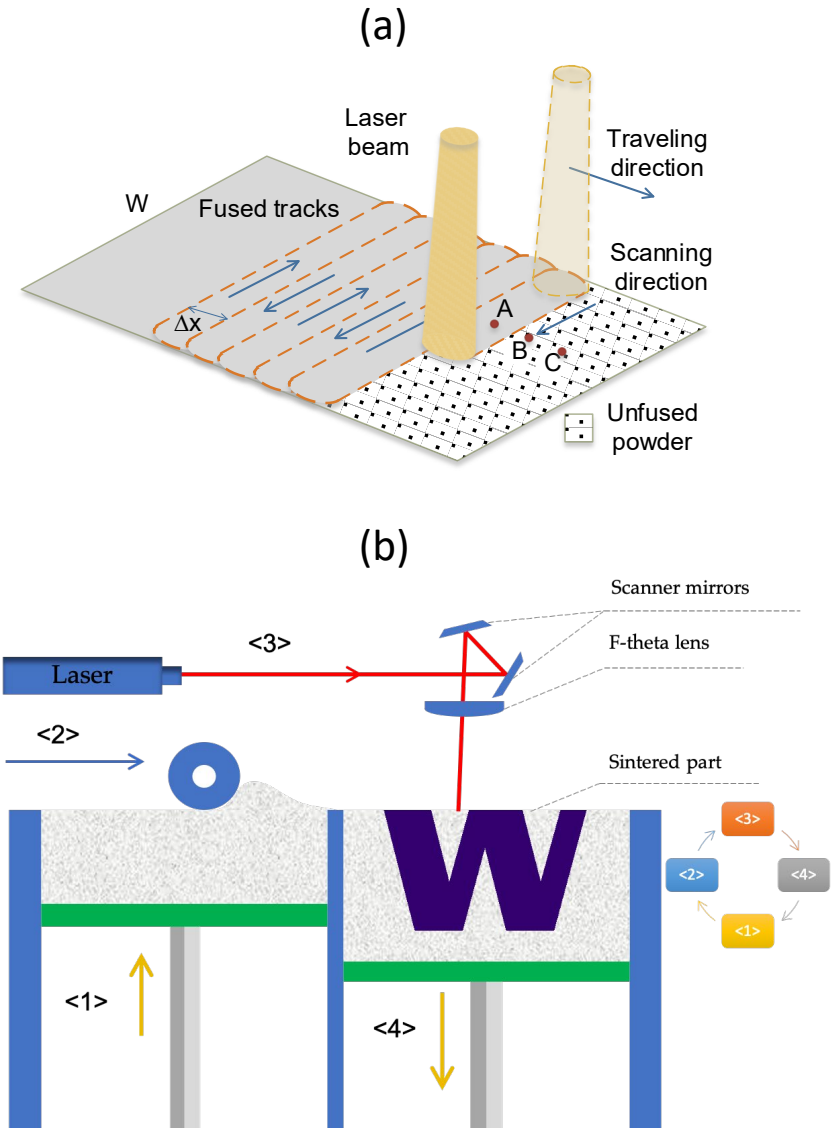

Figure 1.1: Illustration of the LPBF process. (a). In-layer process. (b). Fabrication cycle.

realize this long-felt goal, we need

1. In-situ sensing and process monitoring modalities that measure the process signatures, or more specifically 'dynamic characteristics of the powder heating, melting, and solidification processes as they occur during the build' [12].

2. An efficient data analytics framework that makes sense of the large amount of data to quickly detect the defect formation and determine the quality and stability of the process.

3. Control algorithms that adapt the process parameters based on in-situ measured quantities and, when possible, implement closed-loop repairing actions.

There have been many studies that propose various sensing strategies and modalities, such as optical imaging [9, 15, 16], thermography [17–19], spectrometry [20–22], optical coherence tomography (OCT) [23, 24], and acoustic techniques [25, 26]. These sensors can be classified broadly as spatially integrated (i.e., photodiodes and pyrometers) or spatially resolved (i.e., cameras) and can be employed with moving (coaxial) or fixed references. Fewer studies reported the analytical methods for in-process defect detection and quality evaluation. In [27], the melt pool area and intensity values were measured and correlated to the local measured quality in terms of geometrical accuracy and roughness. Similarly, [22] showed a spatial mapping of melt pool morphological properties to highlight the scan path where anomaly occurs. Principal Component Analysis (PCA) for image data was used in [10] to detect local over-heating phenomena. Even fewer studies have been published so far regarding the development of either reactive, corrective, or feedback control actions. In addition, these limited control efforts mostly focus on the laser-material interaction process but ignore systematic model-based disturbance rejection for other important physical processes (e.g., laser positioning, powder bed preheating).

We envision that a control-oriented mechatronics design provides an opportunity for progress in the robustness and reliability of LPBF AM. In pursuit of such benefit, we first developed a polymer LPBF metrology testbed with the goal of enabling access and manipulation of key manufacturing process parameters to implement control algorithms online. Building upon this platform, we proposed and validated algorithms that addressed some salient disturbances in the LPBF process. Specifically, we 1) developed a disturbance rejection framework and attenuated the vibrations of the LPBF scanning system for improved motion accuracy, 2) proposed a multi-zone control method that controls the temperature distribution of the powder bed surface in the presence of part geometry-induced cross-layer thermal disturbance, and 3) created an efficient image processing

infrastructure for extracting features that elucidate defect precursors and filtering signatures that advance feedback control implementation.

Major Contributions

Control-oriented mechatronic design

One major contribution of the dissertation is establishing a sensor-rich feedback-centric control platform, from mechanisms to the hardware/software interface. Such a research testbed allows researchers to build data-based models, implement model-based online control of the LPBF process, and discover problems hidden in commercial black-box systems.

Loop-shaping Control for Laser Scanning Vibration Disturbance

Positioning accuracy in LPBF systems directly defines the achievable part geometry. Stringent requirements and high safety considerations in industrial sectors such as medical and aerospace set a number of challenges from the viewpoint of sensing, actuation, and control algorithms. This dissertation considers control algorithms for precision positioning. Pioneering an integration of the interpolation theory with a model-based parameterization of the closed loop, the work proposed a filter design that allows strong and flexible local loop shaping for systems with nonminimum-phase zeros. The presented algorithms were evaluated on a precision galvo scanner system in LPBF for attenuating both narrow- and wide-band vibration disturbances.

Multi-zone Control for Powder Bed Thermal Disturbance

Leveraging the multi-zone radiation heating design of the developed platform, this dissertation presented a control-oriented heating model based on the process physics. Building upon the created model, we proposed a multi-zone heating algorithm for controlling powder bed temperature distribution. In the experiment of polymer powder preheating in the presence of different forms of cross-layer thermal disturbances, we verified the benefits of the proposed control as (1) improved accuracy over the state of the art method, (2) comparative performance with optimization-based

model predictive control with reduced computation cost, and (3) flexible extensions to adaptive control schemes.

Image Analytics for Defect Detection and Fusion Process Control

This dissertation discussed a first-of-its-kind image data processing workflow for coaxial visual camera monitoring for LPBF using light-color material. Building on the in-house developed image database, we first proposed a set of pre-processing algorithms to improve the signal-noise ratio of data and then identified the morphological component of laser-material interaction area. From there, we created new features that are correlated to the formation of an overheating defect and part geometry quality metrics. We also discussed the filtering process signature with a Kalman filter for implementing real-time closed-loop control of LPBF.

Chapter 2

CONTROL-ORIENTED MECHATRONIC DESIGN

2.1 Introduction

In LPBF, the physics of the non-contact energy deposition is a union of thermal balance, phase change, and solid mechanics (Fig.2.1). Pre-process high-fidelity simulations can map out an initial parameter space, and post-process material analysis can reveal the internal quality of the built parts; however, mitigation of various in-process disturbances and uncertainties ultimately hinges on real-time in-process controls. Such controls have remained a long-felt but not fully realized vista in LPBF, because a major disconnection exists between existing architectures of online controls and the modeling of this complicated multi-physical process. There are two distinct worlds for such modeling. In the first, the much larger world of numerical methods [28–31], weak forms of the governing equations are obtained by physics-based order reduction. Successful approaches include: (1) removing or combining weak couplings such as surface convection and radiation [32, 33]; (2) Gaussian modeling of the heat source [34]; (3) polynomial or static approximation of the nonlinear parameter variations; and (4) assuming very localized or numerically canceled latent heat from phase change. Finite element and difference methods are then employed to solve the models numerically. In the second, very small world of control-oriented modeling, the sparse attempts that exist use lumped parameter modeling. Low-order linearized models have been proposed [9, 35] based on input-output system identification of a black-box transfer function. The development of such high-fidelity physics-based models relies on accurate measurements of process parameters and process signatures, many of which are difficult to obtain.

With the inaccuracy and complexity of numerical modeling at one hand and the difficulty of obtaining accurate measurements in the physical world at the other, we envision that a fully accessible LPBF metrology testbed can provide unique opportunities for the development of control-

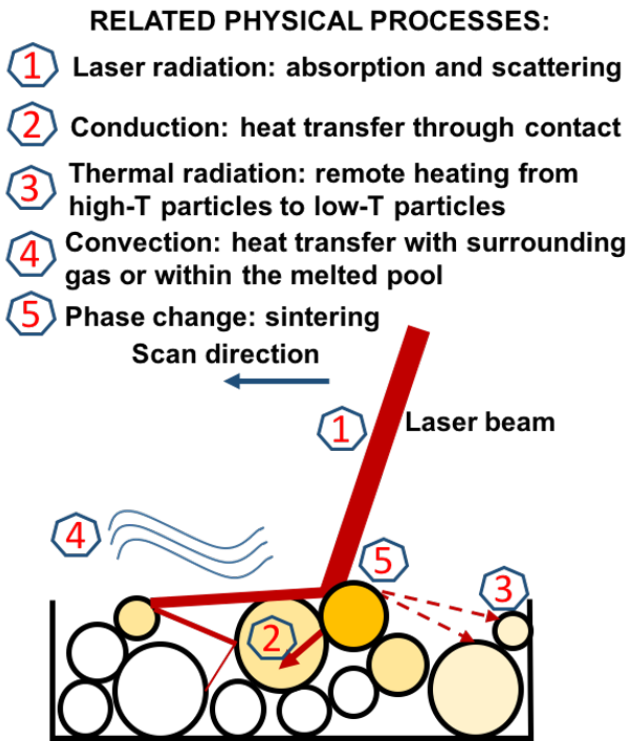

Figure 2.1: Physical processes in LPBF.

oriented modeling and real-time feedback control. It is anticipated that the creation of such a platform will enable researchers to access as well as manipulate key manufacturing process parameters, build online implementable process models, and discover problems hidden in commercial black box-systems. The ultimate goal is to underpin revolutionary progress in ensuring the quality of final parts and reducing the need for costly, time-consuming post-process inspection.

This chapter describes the functional requirements and design solutions to address these objectives. Specifically, we discuss mechatronic designs employed to control some important yet difficult-to-manipulate process parameters, such as the powder bed's temperature, the build cylinder's temperature, and layer thickness. We also present the in-process monitoring methodologies implemented to gather key process information required to perform defect detection and real-time feedback control. We use a fusion of vision camera/pyrometer imaging and infrared thermography

to measure the complex melting pool dynamics and the thermal history of the powder bed. The system control software, built on a real-time data acquisition architecture, provides full access to process data for in-situ monitoring and controls. We validated these mechatronic designs in actual 3D printing of PA12 (Nylon 12).

2.2 Data Acquisition Modalities for the Multi-physical Process

Fig.2.2 provides an overall CAD model and physical view of the developed machine. The machine is designed for polymer LPBF process. Processable materials include but are not limited to PA (polyamide), PEEK (polyetheretherketone), PC (polycarbonateand), and PCL (polycaprolactone). Fig. 2.3 illustrates some sample parts fabricated by the developed testbed. A 100 W Coherent GEM100A CO_2 laser functions as the fusion energy source, which has a high absorption rate for most polymer materials. Before entering the process chamber through a Zinc selenide (ZnSe) window, the laser beam is steered by a Scanlab intelliSCAN14 galvano scanner, which has an $f = 400$ mm F-theta lens that focuses the beam across the effective building area. The powder handling is carried out by a feed cylinder, a build cylinder, and a recoating arm. Servo motors drive the pistons in the powder cylinders with high-ratio gearboxes. The build plate can be manually adjusted to correct for tilt using a screw-spring assembly. The motion of the recoating arm is controlled by timing belt. A modular design for the arm allows for interchanges between recoating using either a blade or a counter-rotating roller. The recoating arm can be adjusted for tilt along the direction perpendicular to the direction of spread. The process chamber is designed to be airtight with flexible heat-insulating ceramic materials attached to the walls and the ceiling to provide an inert gas atmosphere with elevated temperatures for the laser-material interaction process. During operation, heated nitrogen is used to purge air out of the process chamber and provides a positive pressure (controlled by a relief valve). Table 2.1 summarizes the general technical specifications of this LPBF testbed.

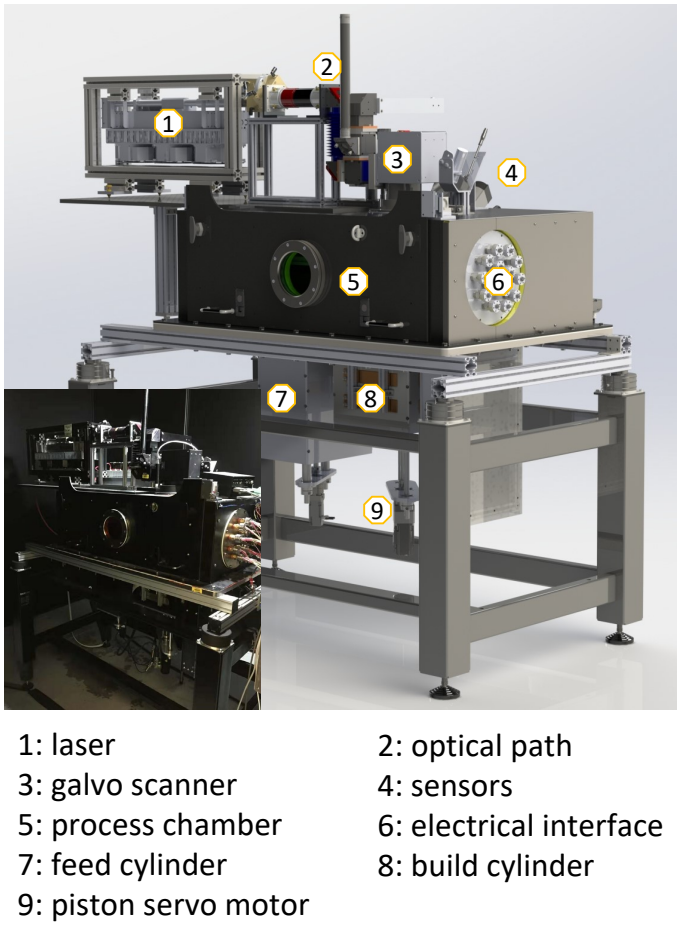

Figure 2.2: Overview of the developed testbed.

2.2.1 Controllable Process Parameters

Process parameters are inputs to the LPBF process and they are either predefined or controllable. Predefined parameters, for example, part geometry, material, powder size distribution, powder packing density, and laser absorptivity, can not be changed during the process. Controllable parameters (e.g., laser and scanning parameters, the layer thickness, and powder bed temperatures) are adjustable online. They generally correlate to the observable and derived process signatures (e.g., melt-pool size, temperature, porosity, or residual stress) by affecting the heating, melting, and solidification processes. Process signatures determine the final product qualities (geometric,

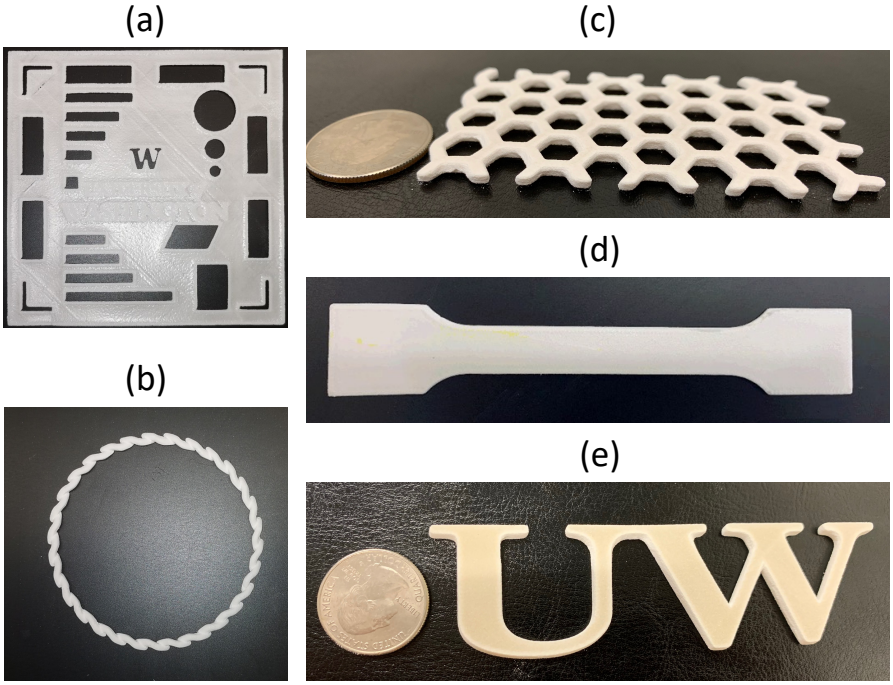

Figure 2.3: Sample parts fabricated by the developed testbed. (a). Single-layer test pattern. (b). Twisted ring. (c). Honeycomb pattern. (d). Type 4 tensile bar. (e). UW logo.

mechanical, and physical). In the category of controllable parameters, some parameters can be more easily adjusted by changing certain variables in software implementation. For example, tuning the duty cycle of pulse-width modulation (PWM) signal can change laser power from track to track. However, many other controllable parameters that are closely related to final part quality metrics require more dedicated mechatronics design efforts.

Powder bed temperature

The temperature of powder bed surface is arguably one of the most significant process parameters as it directly impacts the laser-material interaction. Maintaining a stable and homogeneous temperature across the whole build region is crucial for controlling the heating and cooling rate of the heat affected zone (HAZ), which in turn contributes to mitigated internal stress and isotropic mechanical

Table 2.1: GENERAL TECHNICAL SPECIFICATIONS OF THE DEVELOPED POLYMER LPBF MACHINE.

Material	polymer (PA12, PEEK, PCL, etc.)
Effective building volume	250 × 250 × 150 mm
Feed volume	250 × 178 × 300 mm
Layer thickness	20 μm and above
Laser type	CO_2 100 W
Scan speed	up to 10 m/s
Build plate temperature	up to 300 °C
Process chamber temperature	up to 200 °C
System controller	host computer and NI cRIO9035
Scanning controller	Scanlab RTC5 control board
Software	in-house developed LabVIEW program

properties of the final part. In the developed platform, this is achieved by two control loops that impact the powder bed temperature via thermal radiation and convection, respectively, as shown in Fig. 2.4.

One control loop comprises a multi-zone radiant heater, a non-contact infrared sensor, and an infrared camera. The radiant heater (Fig. 2.5), right above the powder bed, is used to preheat the polymer powder surface to a temperature between the material's cooling onset temperature T_c^{Onset} and melting onset temperature T_m^{Onset} before the start of laser exposure. We integrated nine heating zones, including four corner zones, four side zones, and one center zone (Fig. 2.5). Each zone is composed of one or two quartz heaters. The radiation powder for different zones can be independently adjusted using a 16-channel analog voltage output DAC (Digital-to-Analog Converter), thereby making it possible to minimize temperature gradient across the powder bed surface with control algorithms (discussed in Chapter 4).

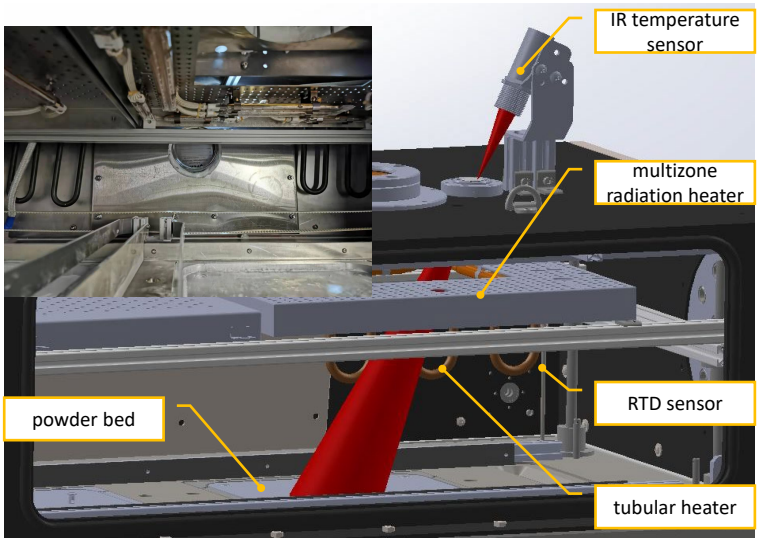

Figure 2.4: Powder bed temperature control setup.

The surface temperature can either be measured by an infrared temperature sensor with a close focus lens that provides a large field of view (red beam in Fig. 2.4). The measurement is an averaged value for an area on the build surface. The principle of such a sensor is to measure the infrared radiation emitted from the powder bed and calculate the corresponding temperature according to Planck's law[1]. However, the radiant heater is also a strong radiation source and a portion of the radiation is reflected by the powder surface. As a result, the sensor receives both emitted and reflected radiation. Therefore, it is important for the sensor to be able to filter out the reflected portion to generate correct measurement. Alternatively, the temperature of the full powder bed can be measured by a thermal camera with resolution 320×240, which provides spatially-resolved thermal profile information. The setup of the thermal camera is discussed in detail in Section 2.2.2.

The other control loop impacts the power bed temperature by controlling the ambient temperature in the process chamber. This is achieved by controlling the power of two tubular heaters (maximum power 1000 W) mounted on the back wall (Fig. 2.4). Two Pt-100 RTD (resistance temperature detector) sensors, one located at the back right corner and the other at the front left corner,

[1]This is also the working principle of the thermal camera.

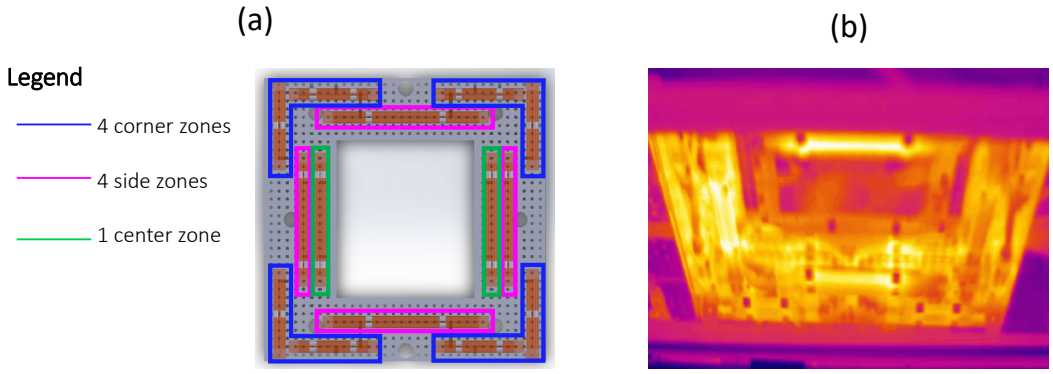

Figure 2.5: Multi-zone radiation heater. (a). Heating zone layout. (b). Thermal image of the working heater.

measure the atmosphere temperature. The control goal here is to match the temperature between the atmosphere and powder surface to reduce the heat convection between fused powder and environment. This is beneficial from the standpoint of decreasing cooling rate and mitigating residual stress. Controlling the ambient temperature also reduces the disturbances and uncertainties for different locations of the part, thereby contributing to homogeneous part properties.

Build cylinder temperature

Post-fusion thermal history is also proved to be an impact factor to part mechanical properties [8, 36, 37]. For polymer LPBF, the finished part is contained in the build cylinder and cools down within a couple of hours to a day. To control the cool-down phase and reduce temperature gradient-induced distortion, the build cylinder is also featured with closed-loop control. We implemented multiple resistive strip heaters and RTDs to the build plate and the walls of the build cylinder, as shown in Fig. 2.6.

The heater for the build plate is a 700 W mica heater (Fig. 2.6(b)) and is capable of heating the plate up to 300 °C. An RTD is placed into a slot under the build plate to be as close to the build surface as possible so that the measurement error induced by the thermal gradient in the plate is

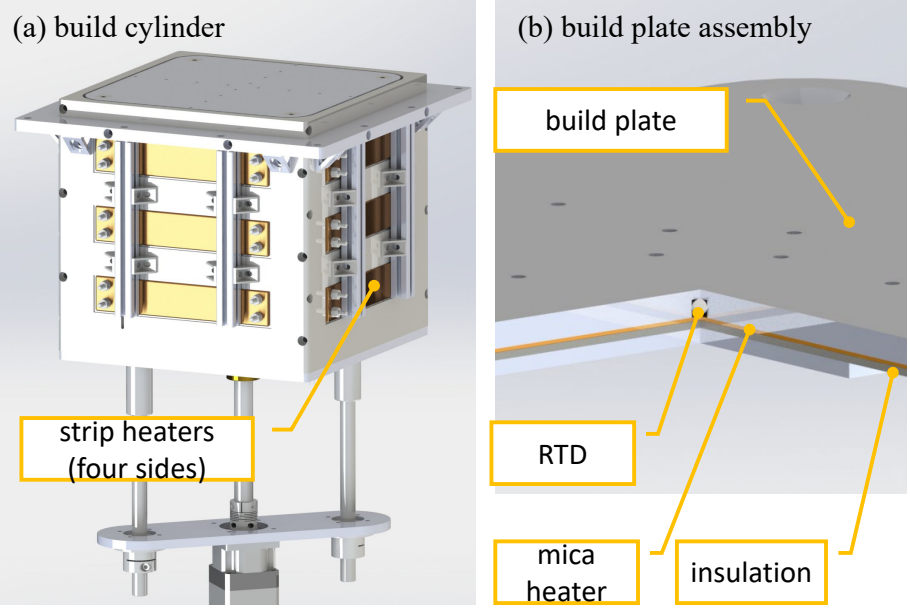

Figure 2.6: Build cylinder temperature control design.

negligible. Three 500 W strip heaters are used for each side of the cylinder wall, with an RTD placed between each heater and the wall. By their height levels, these heaters are categorized into three zones. All build cylinder heating zones are controlled by two industrial Watlow EZ-ZONE controllers with built-in PID controllers.

Layer thickness

Despite the build-plate position is controlled by a high-precision servo motor, additional disturbances and uncertainties can introduce variance to layer thickness. For example, due to the backlash of the leadscrew, the build plate position must be re-calibrated each time the travel direction reverses. For another example, as the build plate is supported by a spring assembly, the variation of friction between the plate insulation layer and the cylinder wall can induce uncertainty to the build plate position. As a result, additional control has to be considered to achieve micrometer-scale motion precision and reduce layer thickness variance. This is realized by utilizing a Keyence CCD laser displacement sensor, which measures powder bed surface displacement by emitting a laser

beam towards the target and measuring the receiving beam position on a light-receiving element. Leveraging a cylindrical lens, the sensor produces a laser spot with a size of approximately 290 × 8300 µm on the powder bed. The measured value is obtained by averaging across the spot region. Therefore, the surface roughness induced by polymer particle diameter is averaged out.

2.2.2 Process Monitoring

On the developed platform, we designed both coaxial and offaxial monitoring modalities to capture different process signatures.

Coaxial monitoring

The coaxial configuration is also referred to as Lagrangian frame of reference. The sensors employed coaxially exploit the optical path of the power source to observe the melt pool directly through the scan head. This configuration allows the melt pool instabilities and variation to be observed in real time. Spatially integrated sensor (such as pyrometer and photodiode) employed in this type of setup is sensitive to variations in laser power, powder layer thickness, scan spacing, and scan pattern, etc [9, 38]. Spatially resolved sensor (e.g., visual camera, thermal camera) in this mode can capture high lateral resolution images of important melting pool dynamics, such as melting pool shape, melting pool size, and thermal gradient that reflect numerous error modes and process variations. Fig. 2.7 shows the designed optical path for coaxial monitoring. This optical path allows for bidirectional beam/light propagation:

- *Forward propagation (laser beam)*: The laser beam (with 10.6 µm wavelength) from the laser head is first converted from a linearly polarized beam to a circularly polarized beam by a polarizer. Then the beam diameter is expanded from 3.8 mm to 14 mm by the collimator. These two modules optimize the shape and dimension of the final laser spot on the powder bed. After which, the laser beam transmits through a dichroic mirror and reaches the galvono mirrors, where it is reflected. At the exit pupil of the forward optical path, an F-theta lens

focuses the laser beam on the a flat plane–the powder bed surface. The distance between the F-theta lens and powder bed is adjustable for calibration purpose. The full propagation path of the laser beam is depicted by the red trace in Fig. 2.7(b).

- *Backward propagation*: The radiation from the melting pool (visible light) is reflected by galvo mirrors and then reflected by the dichroic mirror towards a beam splitter, which separates the radiation towards a photodiode (30%) and a high-speed visual camera (70%). Both sensors have a focal system. The focal length of the camera is adjustable. The full propagation path of the back reflection is depicted by the blue trace in Fig. 2.7(b).

The core component that realizes the functions described above is a ZnSe dichroic mirror with a carefully designed coating. The reflection rate of the dichroic mirror is lower than 0.5% for 10.6 μm (laser wavelength) and higher than 98.5% for 633 nm (illumination light wavelength) at an incidence angle of 45°. The camera can capture full-resolution images (1920 × 1080) at 1.2 kFPS (kilo frame per second) and even faster by reading out only region of interest (ROI). The photodiode has a spectral response wavelength range between 300 to 680 μm, with peak sensitivity at 640 μm. Its rise time is 1 μs, hence providing a 3 dB response frequency[2] of 0.35 MS/s (million sample per second).

Fig. 2.8 shows the sample images captured by the coaxial camera.

Offaxial thermographical monitoring

Offaxial monitoring is also referred as to Eulerian frame of reference. It is implemented in the developed testbed as a complementary approach that monitors a fixed area of the build surface. Compared to coaxial configuration, such setup brings unique advantages regarding process signatures related to thermal history. The thermal history of material strongly influences and in many cases is the primary determinant of the part's final physical and mechanical properties [7]. We proposed to use an FLIR A325sc longwave thermal camera, with 60 Hz frame rate at the full

[2]The frequency at which the photodiode output decreases by 3 dB is roughly approximated by $0.35/t_{rise}$

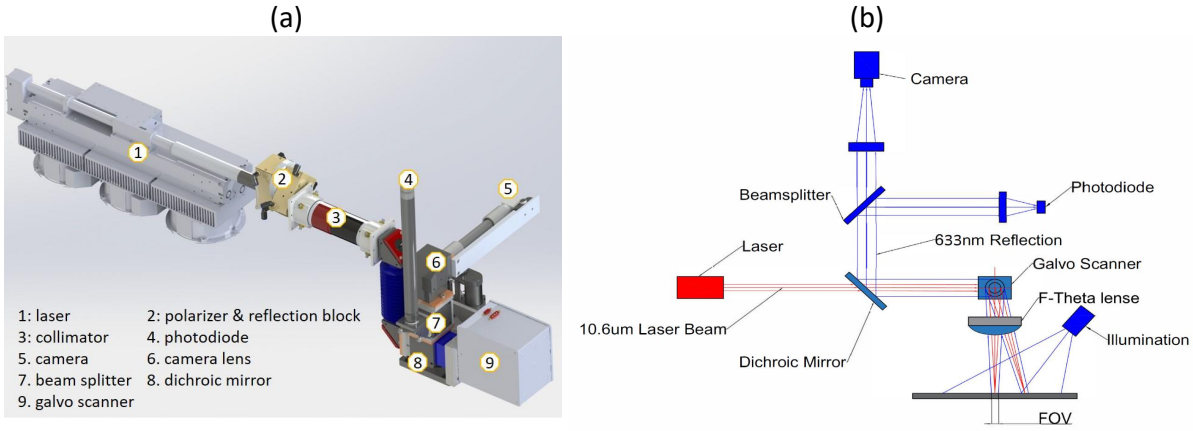

Figure 2.7: Coaxial optical path design. (a) CAD view. (b) Optical path illustration.

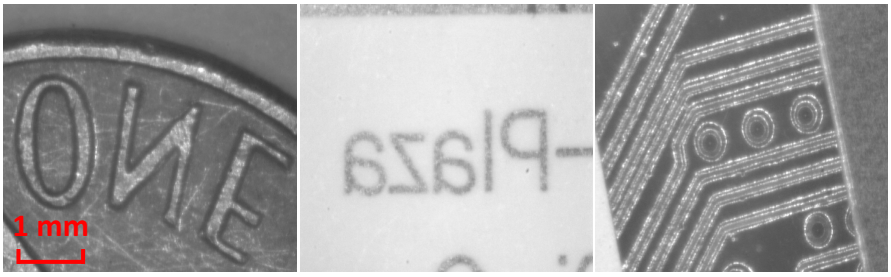

Figure 2.8: Sample images captured by the coaxially-aligned camera. (a) One dime coin. (b) Name card. (c) Printed circuit board.

resolution of 320 × 240 pixels. An important consideration in off-axis configuration is that the angle between the optical axis of the camera and the normal axis of the build bed can not exceed 45°. This is especially true for the thermal camera. Otherwise, large measurement errors will be induced by the variance of emissivity for different areas in the field of view.

2.3 Controller and Software Design

Fig. 2.9 shows the schematic of the designed control hierarchy. Three control cores comprise the control system of the platform:

1. *NI compactRIO (cRIO)*: real-time control platform, with multiple data I/O and acquisition modules (e.g., digital I/O, analog I/O, serial communication, temperature measurement, etc.).

2. *ScanLAB RTC5*: real-time scan system controller.

3. *Host computer*: Windows ×86 workstation.

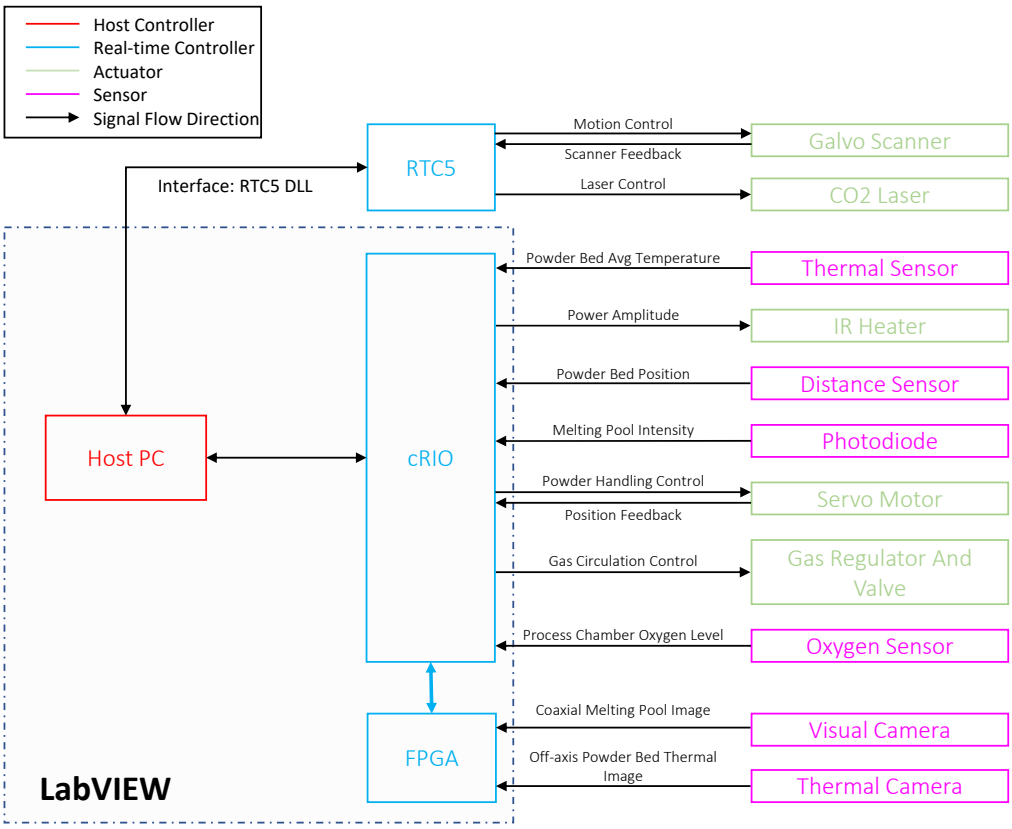

Figure 2.9: System control hierarchy.

The host computer performs non-time-critical high-level tasks, e.g., processing the pre-generated scanning path in the format of G-code, taking scan settings via GUI (graphical user interface). During printing, it monitors the process status and communicates with real-time controllers. The cRIO, on the other hand, performs time-critical low-level tasks, such as system temperature control (process

chamber, build chamber), oxygen level control, motion control of the piston and recoating arm, etc. RTC5 board directly controls the motion of galvo scanner and the output power of the CO_2 laser simultaneously. The host computer converts G-cod into scanning commands that are processable by RTC5 (jump command for G0 and mark command for G1) and stores them in the execution list buffer of the RTC5 board. This is realized by importing and calling API (application programming interface) functions in the LabVIEW environment.

The coaxial camera is triggered by an FPGA (Field-Programmable Gate Array)-based frame grabber. The advantages of FPGA are high data bandwidth and computation power. Using a four-connection CoaXPress CXP-12 interface, it provides up to 5000 MB/s camera data bandwidth, which allows the acquisition of full-resolution images (1920×1080) at 2kFPS. After which, the data is processed based on a First-In-First-Out (FIFO) principle with customized algorithms (discussed in detail in Chapter 5) that execute on the FPGA. The thermal image data acquisition and processing, with a much lower data bandwidth, is implemented by cRIO using vendor-supplied APIs.

Fig. 2.10 shows the flowchart for a typical printing job. Before printing, the process chamber is preheated and purged. The build plate is also heated by the mica heater. The procedures for printing each layer consist of recoating, IR preheating, and laser fusion. It is worth noting that compared with commercially available machines, where process parameters are typically kept constant through the whole job, many process parameters (e.g., laser power, scan velocity) can be changed for each scanning track.

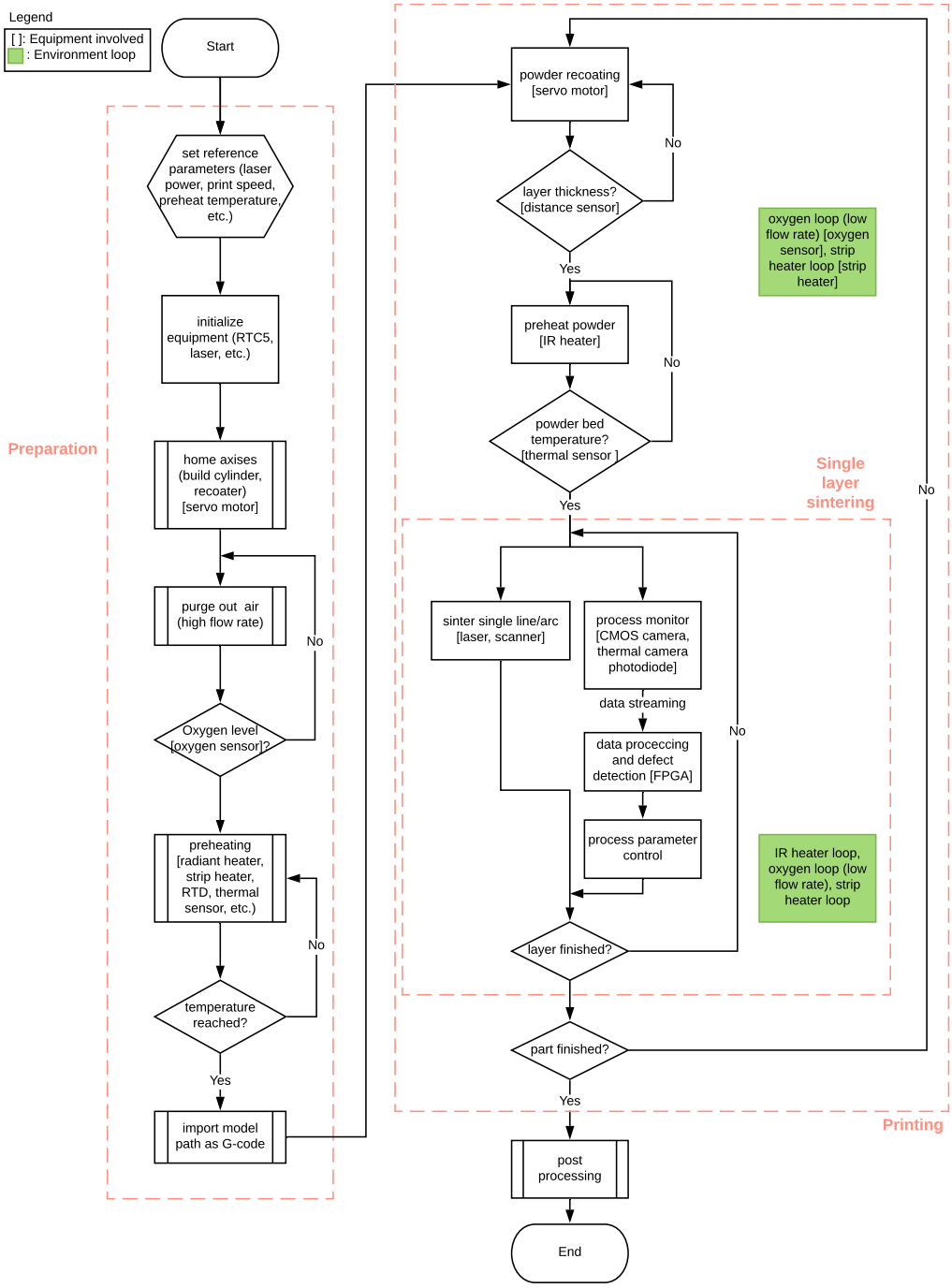

Figure 2.10: Flowchart for a printing job.

Chapter 3

LOOP-SHAPING CONTROL FOR LASER SCANNING VIBRATION DISTURBANCE

3.1 Introduction

Active and flexible shaping of dynamic system responses is central for modern precision systems and advanced manufacturing. For example, adaptive disturbance attenuation minimizes the position error of read/write head and achieves nm-scale motion control in modern hard disk drives [1, 39]; in smart headphones, active acoustic noise cancellation reduces acoustic disturbance transmission from the environment to human ears [40]. In LPBF additive manufacturing, a dual-axis galvo mirror scanning system positions the laser beam on the powder bed. The work diagram of such a scanner is shown in Fig. 3.1. With a scanning distance of $L = 400$ mm, an angular position error of $\theta = 0.2$ mrad can cause a dimension error of approximately 0.16 mm on the fused part, which can be easily beyond the dimension tolerance limit. On the other hand, strong external vibration disturbances exist that impacts the scanner position, including:

- vibration from cooling fans,
- cross-axis interference,
- complex environmental vibration.

In these applications, a certain form of output profile is desired given various band-limited disturbances, yielding the problem of local loop shaping (LLS).

Based on the target disturbance energy distribution, relevant LLS control algorithms can be generally classified into two categories: narrow- and wide-band loop shaping[1]. In the first category,

[1]The classification depends on the system of study. If the width of disturbance peak is comparable to the system

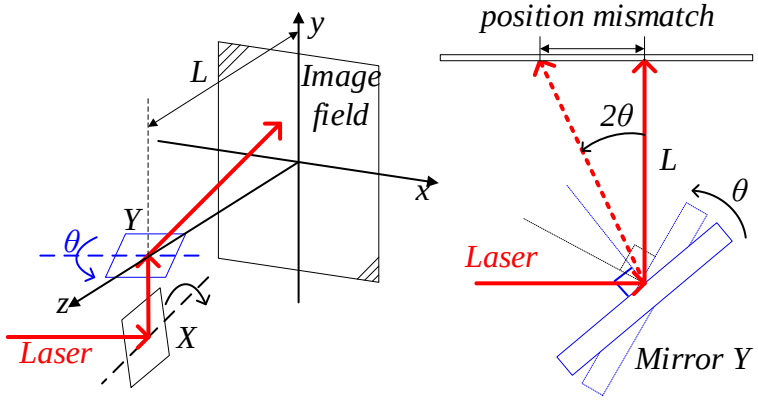

Figure 3.1: Schematic diagram of galvo scanner and position mismatch.

the energy of disturbance concentrates at one or several unknown and/or time-varying frequencies. Based on such characteristics, peak filter [41, 42], repetitive control [43, 44], narrow-band Youla-Kucera parameterization [45–47], $\mathscr{H}_\infty$ gain scheduling [48], and narrow-band disturbance observer (DOB) [39, 49, 50] generate deep but narrow notches in the closed-loop error-rejection functions at frequencies where the input disturbance energy dominates. For wide-band loop shaping, the disturbance energy spans over wide frequency bands in the spectrum. A narrow notch cannot provide sufficient attenuation to such inputs; yet a wide notch tends to cause undesired amplification at other frequencies (the fundamental waterbed effect in feedback control for linear time-invariant (LTI) systems [51–53]). In view of such challenges, [54] proposed to detune the notch depth and place fixed zeros according to the performance criterion; [1] utilized an online adaptation algorithm to estimate both frequency and notch width at the same time for optimal wide-band design.

Despite current research achievements, strong and flexible local loop shaping for systems with unstable zeros has remained challenging, particularly for wide-band applications. Consider controlling a single-input-single-output (SISO) LTI plant P with controller C in a negative feedback loop. Careful stability guarantees must be enforced for algorithms that directly update C [41–44, 48]. Focusing instead on performance and using a control architecture that guarantees stability

---

bandwidth, then the disturbance can be considered as "wide-band". In contrast, if the disturbance width is closed to system sampling time, then it may be classified as "narrow-band".

intrinsically, algorithms built on Youla parameterization [45, 54–57] have the benefit of directly shaping the closed-loop sensitivity function with $S = (1 - NQ/Y)/(1 + PC)$, where N and Y come from coprime factorizations of P and C. That is, instead of modifying C directly, Youla-based approaches shift the design focus to an affine parameter Q in the sensitivity function. For plants with a stable inverse, N and Y have been shown to be reducible to yield the minimum-order design-friendly factorization $S = (1 - z^{-m}Q)/(1 + PC)$. This is the approach proposed in the narrow-band DOB [39, 54, 58], which has achieved first-tier ranking in an international benchmark on adaptive regulation [47]. However, such benefit is currently infeasible for plants with nonminimum-phase zeros since such plants can not be directly inverted and implemented. Multiple strategies that create stable and realizable model inversion exist in modern literature. For example, nonminimum-phase zeros-ignore method [59], zero-phase-error-tracking control [60], and zero-magnitude-error-tracking control [61] find transfer function expression of the inversion by replacing the unstable zeros with stable substitutions; ILC-based (iterative learning control) method constructs inverse model by generating impulse response from feedforward signal [62]; time-domain strategies [63–66] aim at identifying the optimal control signal that minimizes the error between a given reference and the output. However, since the unstable zeros cannot be perfectly inverted into the denominator, the inversions are only accurate at certain frequencies.

In view of the importance of disturbance attenuation and the discussed challenges of control design, we propose a new local loop-shaping algorithm for shaping the closed-loop response. Compared with previous algorithms such as the DOB, this *forward model selective disturbance observer* (FMSDOB) avoids introducing an explicit plant model inversion, thereby offering freedom and flexibility of loop shaping for nonminimum-phase systems. Compared to other loop-shaping designs, the proposed algorithm inherits benefits of DOB design regarding design intuition and strong performance [47, 50]. This is achieved by pioneering an integration of the interpolation theory to Youla-parameterization and internal model controls, to design a class of Q filters that safely invert the nonminimum-phase plant frequency response locally. The result is that we can create strong notches flexibly in the closed-loop sensitivity function to reject both narrow- and wide-band disturbances. From there, to mitigate undesired amplification from the waterbed effect,

we then propose techniques to flexibly control the structure of this Q filter based on the disturbance energy spectrum, performance goals, and robustness of the system.

Augmenting these theoretical results, we conducted simulation and experimental verifications on a laser scan head in LPBF additive manufacturing. During the process, we found further that for minimum-phase plants, the proposed algorithm performs equally well with and even surpasses classical inverse-based disturbance observer.

The remainder of this chapter is organized as follows. Section 3.2 describes the principle, benefits, and limitations of conventional disturbance observer. Section 3.3 describes the proposed FMSDOB and illustrates the loop shaping philosophy. Section 3.4 discusses the selective inversion Q filter design for narrow-band disturbance, following which Section 3.5 develops the Q filter design extension for wide-band disturbance. Section 3.6 discusses the fundamental performance limitation and analyzes the stability and robustness of the proposed method. Section 3.7 provides the simulation and experimental verification results.

Notations. $P(z)$ and $P(e^{j\omega})$ denote, respectively, a discrete-time transfer function and its frequency response. The calligraphic $\mathfrak{R}$ and $\mathfrak{I}$ denote, respectively, the real and the imaginary parts of a complex number. The calligraphic $\mathscr{S}$ denotes the set of *stable proper rational transfer functions*; and $\mathscr{R}$ denotes the set of *proper rational transfer functions*. $S(\triangleq 1/(1+PC))$ denotes the sensitivity function (i.e., the transfer function from the output disturbance to the plant output) of a feedback loop consisting of a plant P stabilized by a LTI controller C. $T(\triangleq PC/(1+PC))$ denotes the complementary sensitivity function.

3.2 Conventional Inverse-based Disturbance Observer

3.2.1 Youla-Kucera parameterization

A conventional disturbance observer is a pseudo Youla-Kucera (YK) parameterization scheme-a formulation of all stabilizing controllers.

Let $G \in \mathscr{R}$. (N,D) is called a coprime factorization of G over $\mathscr{S}$ if: (i) $G = ND^{-1}$, (ii) $N(\in \mathscr{S})$ and $D(\in \mathscr{S})$ are coprime transfer functions, and (iii) $D^{-1} \in \mathscr{R}$.

Theorem 1. *(YK Parameterization [67, 68]). If a SISO plant $P = N/D$ can be stabilized by a negative-feedback controller $C = X/Y$, with (N,D) and (X,Y) being coprime factorizations over $\mathscr{S}$, then any stabilizing feedback controller of P can be parameterized as*

$$C_{all} = \frac{X + DQ}{Y - NQ} : Q \in \mathscr{S}, Y(\infty) - N(\infty)Q(\infty) \neq 0. \tag{3.1}$$

YK parameterization advantageously changes the principle of feedback design by rendering the new sensitivity function to:

$$\tilde{S} = \frac{1}{1 + PC_{all}} = \frac{1}{1 + PC}\left[1 - \frac{N}{Y}Q\right]. \tag{3.2}$$

Theorem 1 proposes an add-on scheme that decouples sensitivity function S to the product of the baseline sensitivity $1/(1+PC)$ and the add-on affine module $1 - NQ/Y$.

3.2.2 Disturbance observer-A pseudo YK design

Consider a plant whose relative degree is m. Let $X(z) = C(z)$, $Y(z) = 1$, $N(z) = z^{-m}$, and $D(z) = z^{-m}P^{-1}(z)$ in Theorem 1. **If $\mathbf{P^{-1}(z)}$ and $\mathbf{C(z)}$ are stable**, then the all stabilizing controllers (3.1) transfers to

$$C_{all} = \frac{C(z) + z^{-m}P^{-1}(z)Q(z)}{1 - z^{-m}Q(z)}, Q \in \mathscr{S}. \tag{3.3}$$

and the sensitivity function is

$$S = \frac{1 - z^{-m}Q(z)}{1 + P(z)C(z)} \triangleq S_0(z)\left(1 - z^{-m}Q(z)\right) \tag{3.4}$$

(3.4) reduces the add-on module in the sensitivity function to $1 - z^{-m}Q(z)$. The inverse-based parameterization has made the added module simple and depend little on $C(z)$ and $P(z)$ (only the delay z^{-m} appears here). This was achieved by confining to plants with **stable inverses**, and closed loops with stable baseline controllers. When a stable inverse P^{-1} is not available, a **chosen stable** estimate $\hat{P}^{-1}(z)$ can be used to form the new feedback controller:

$$\tilde{C} = \frac{C(z) + z^{-m}\hat{P}^{-1}(z)Q(z)}{1 - z^{-m}Q(z)}, Q \in \mathscr{S}. \tag{3.5}$$

Fig. 3.2 shows the control scheme based on (3.5). By block diagram analysis, one can show that when $r(k) = 0$ and $z^{-m}Q(z)|_{z=e^{j\omega_i}} \simeq 1$, $c(k)$ approximates $-d(k)$ at ω_i (hence canceling the disturbance). Such time-domain intuition can be used for tuning during implementations.

From the frequency-response perspective, if we design a Q-filter $Q(z^{-1})$ with its frequency response as shown in Fig. 3.3, then $1 - e^{-mj\omega}Q(e^{-j\omega})$ (replacing z^{-1} with $z^{-j\omega}$) in (3.4) will become zero at the center frequencies of $Q(z^{-1})$ namely, disturbances occurring at these frequencies will be strongly attenuated.

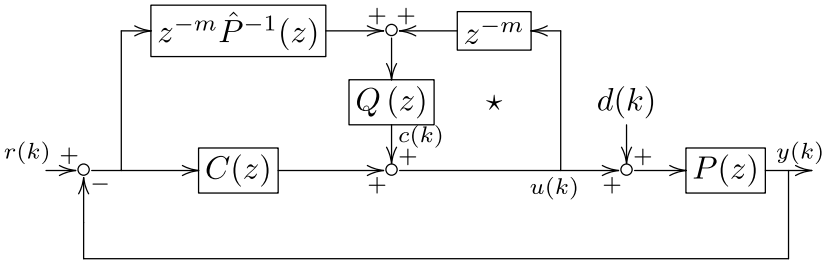

Figure 3.2: Block diagram of pseudo YK parameterization-based disturbance observer.

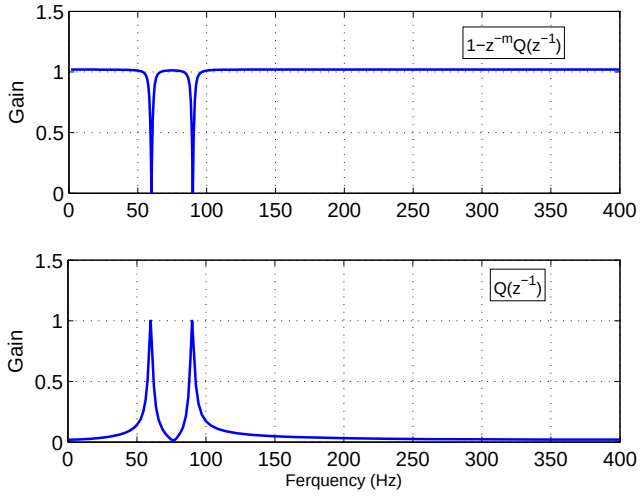

Figure 3.3: Frequency response of a Q-filter example.

The inverse-based disturbance observer is an intuitive design that leverages the decoupled error rejection principle of YK parameterization. It has good performance for structured vibration rejection.

However, note that it is central to have an accurate plant inverse $\hat{P}^{-1}(z)$ such that $\hat{P}^{-1}(z)P(z) = 1$. For a minimum-phase system (no unstable zeros), this is straightforward as long as a good plant estimation $\hat{P}(z)$ is constructed (based on modeling or system identification). For a system with nonminimum-phase (or unstable) zeros, $P^{-1}(z)$ is unstable and cannot be implemented directly. To find a stable, rational, and causal replacement $\hat{P}^{-1}(z)$ is thus a fundamental challenge in such design.

In view of such design challenge, we propose a new local loop-shaping algorithm for shaping the closed-loop response. Compared with the inverse-based algorithm, this forward model selective disturbance observer avoids introducing a explicit plant model inversion, thereby offering freedom and flexibility of loop shaping for nonminimum-phase systems.

3.3 Forward Model Selective Disturbance Observer

Fig. 3.4 shows the proposed control scheme. We have the following relevant signals and transfer functions:

- $P(z)$ and $\hat{P}(z)$: the plant and its identified model;
- $C(z)$: a baseline controller designed to provide a robustly stable closed loop;
- $d(k)$ and $\hat{d}(k)$: the actual (unmeasurable) vibration disturbance and its online estimate;
- $\tilde{u}(k)$ and $u(k)$: the control command with and without the compensation signal;
- $y(k)$: measured residual error;
- $c(k)$: the compensation signal that asymptotically rejects the disturbance $d(k)$.

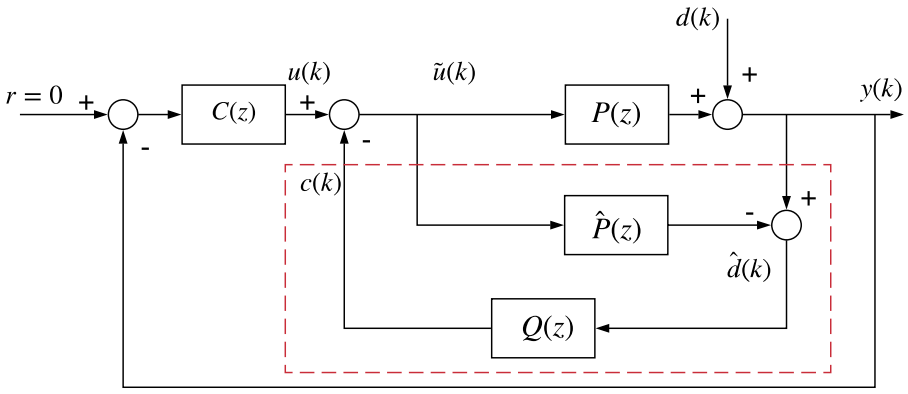

Figure 3.4: Proposed forward model selective disturbance observer scheme.

Assumption 2. *Focusing first on nonminimum-phase zeros, we assume that the transfer function $P(z)$ is rational, proper, and stable, but has unstable zeros. We will provide generalizations to unstable plants after introducing the main design principles of the Q filter.*

Assumption 3. *The magnitude of $P(e^{j\omega})$ is nonzero at the target frequencies (otherwise, the disturbance is directly blocked by the plant).*

The basic structure of the closed loop is a special version of YK parameterization (Theorem 1). Specifically, letting $X(z) = C(z)$, $Y(z) = 1$, $N(z) = P(z)$, and $D(z) = 1$ (this is feasible under Assumption 2) yields the stabilizing controller

$$C_{all}(z) = \frac{C(z) + Q(z)}{1 - P(z)Q(z)}, \tag{3.6}$$

and Fig. 3.4 presents one specific realization of the parameterization when $\hat{P}(z) = P(z)$.

Block-diagram analysis gives that if $\hat{P}(z) = P(z)$, then $\hat{d}(k) = d(k)$ in Fig. 3.4. If $Q(z)$ additionally inverts $P(z)$ at frequencies where $d(k)$ contain major spectral components, then passing $\hat{d}(k)$ through $Q(z)$ (dashed box in in Fig. 3.4) and then through $P(z)$ via the internal negative feedback yields disturbance attenuation.

From a loop shaping perspective, one can obtain the augmented plant dynamics

$$Y(z) = P(z)U(z) + (1 - P(z)Q(z))D(z). \tag{3.7}$$

When $r = 0$, by using $u(k) = -C(z)y(k)$ in (3.7), the closed-loop dynamics between $d(k)$ and $y(k)$, i.e., the sensitivity function, becomes

$$S(z) = \frac{1 - P(z)Q(z)}{1 + P(z)C(z)} \triangleq S_0(z)(1 - P(z)Q(z)), \tag{3.8}$$

Here, if the add-on module $1 - P(z)Q(z) = 0$, then the disturbance transmission is cut off entirely. Of course, in the focused problem setup, $1 - P(z)Q(z) = 0$ over the full frequency range is not achievable because it implies $Q(z) = P^{-1}(z)$, i.e., an unstable inverse. In the following sections, we will design Q to selectively invert the plant dynamics for controlling general band-limited disturbances. Then, we will circle back to discuss the case when the plant contains uncertainties (i.e., $P(z) \neq \hat{P}(z)$).

3.4 Q Filter Design for Narrow-band Disturbance

We consider first a pointwise inverse of P such that

$$Q(e^{j\omega_i})P(e^{j\omega_i}) = 1. \tag{3.9}$$

at a set of target frequencies $\{\omega_i : \omega_i \in (0,\pi), i = 1,2,\ldots,n\}$ $(\omega_i \neq \omega_j, \forall i \neq j)$.

Under Assumption 3, the equation translates to

$$Q(e^{j\omega_i}) = \frac{1}{P(e^{j\omega_i})} = \frac{\overline{P(e^{j\omega_i})}}{|P(e^{j\omega_i})|^2},$$

i.e.,

$$\begin{cases} \Im Q(e^{j\omega_i}) = -\frac{\Im P(e^{j\omega_i})}{|P(e^{j\omega_i})|^2} \\ \Re Q(e^{j\omega_i}) = \frac{\Re P(e^{j\omega_i})}{|P(e^{j\omega_i})|^2} \end{cases}, \; i = 1,2,\ldots,n. \tag{3.10}$$

Proposition 4. *Let*

$$Q(z) = b_0 + \sum_{l=1}^{m} b_l z^{-l}, \tag{3.11}$$

with

$$\begin{bmatrix} b_0 \\ \vdots \\ b_m \end{bmatrix} = \begin{bmatrix} 1 & \cos\omega_1 & \dots & \cos m\omega_1 \\ 0 & \sin\omega_1 & \dots & \sin m\omega_1 \\ \vdots & & & \vdots \\ \vdots & & & \vdots \\ 1 & \cos\omega_n & \dots & \cos m\omega_n \\ 0 & \sin\omega_n & \dots & \sin m\omega_n \end{bmatrix}^{-1} \begin{bmatrix} \frac{\Re P(e^{j\omega_1})}{|P(e^{j\omega_1})|^2} \\ \frac{\Im P(e^{j\omega_1})}{|P(e^{j\omega_1})|^2} \\ \vdots \\ \vdots \\ \frac{\Re P(e^{j\omega_n})}{|P(e^{j\omega_n})|^2} \\ \frac{\Im P(e^{j\omega_n})}{|P(e^{j\omega_n})|^2} \end{bmatrix}, \tag{3.12}$$

where $m = 2n-1$. *Then*

$$Q(e^{j\omega_i})P(e^{j\omega_i}) = 1,\ \forall i = 1,2,\dots,n.$$

Proof. Let $Q(e^{j\omega}) = b_0 + \sum_{l=1}^{m} b_l e^{-lj\omega}$, where $m(\in \mathbb{Z})$ is the order of the filter. Based on (3.10), we must have, for $i = 1,2,\dots,n$,

$$\begin{aligned} b_0 + \sum_{l=1}^{m} b_l \cos l\omega_i &= \frac{\Re P(e^{j\omega_i})}{|P(e^{j\omega_i})|^2} \\ \sum_{l=1}^{m} b_l \sin l\omega_i &= \frac{\Im P(e^{j\omega_i})}{|P(e^{j\omega_i})|^2}. \end{aligned}$$

In matrix form, the above is equivalent to

$$\begin{bmatrix} 1 & \cos\omega_i & \dots & \cos m\omega_i \\ 0 & \sin\omega_i & \dots & \sin m\omega_i \end{bmatrix} \begin{bmatrix} b_0 \\ \vdots \\ b_m \end{bmatrix} = \begin{bmatrix} \frac{\Re P(e^{j\omega_i})}{|P(e^{j\omega_i})|^2} \\ \frac{\Im P(e^{j\omega_i})}{|P(e^{j\omega_i})|^2} \end{bmatrix}. \tag{3.13}$$

There are n such equation sets, or $2n$ linear equations. When $\omega_i \in (0,\pi)$, the rows of the matrix on the left side are all linearly independent for different values of ω_i's. We thus have $2n$ linearly independent equations and $m+1$ unknowns, the minimum order of $Q(z)$ for the existence of a unique solution is $m+1 = 2n$. Under this case, the solutions of b_i's are given by (3.12). □

Proposition 4 relaxes the requirement of a full stable inverse by focusing on $P^{-1}(e^{j\omega_i})$ at selective regions based on the target disturbance profiles. For implementation, one can selectively measure the frequency response of the plant in regions where loop shaping is desired. Putting these

data into the vector on the right hand side of (3.12), one can obtain the Q solution for target loop shaping. Adaptation is further possible, given a known or online identified $P(e^{j\omega_i})$.

Example 5. The nominal transfer function for a galvo scanner is given by

$$P(z) = \frac{0.0282z^2 + 0.1504z + 0.1146}{z^4 - 1.3190z^3 + 0.929z^2 - 0.6073z - 0.0035}, \tag{3.14}$$

with a sampling time of $T_s = 2.5 \times 10^{-5}$ sec. Then for three narrow-band disturbances $\omega_1 = 0.1\pi$, $\omega_2 = 0.2\pi$, and $\omega_3 = 0.35\pi$ (or 2000Hz, 4000Hz, and 7000Hz), a Q filter with order $m = 5$ is needed. Solving (3.12) gives $\begin{bmatrix} b_0 & b_1 & b_2 & b_3 & b_4 & b_5 \end{bmatrix}^T = \begin{bmatrix} 22.6 & -88.0 & 149.7 & -147.1 & 82.9 & -21.7 \end{bmatrix}^T$. The comparison result between the frequency response of $P^{-1}(z)$ and $Q(z)$ is shown in Fig. 3.5. The intersection points at 2000Hz, 4000Hz, and 7000Hz show that (3.9) is achieved at the target frequencies.

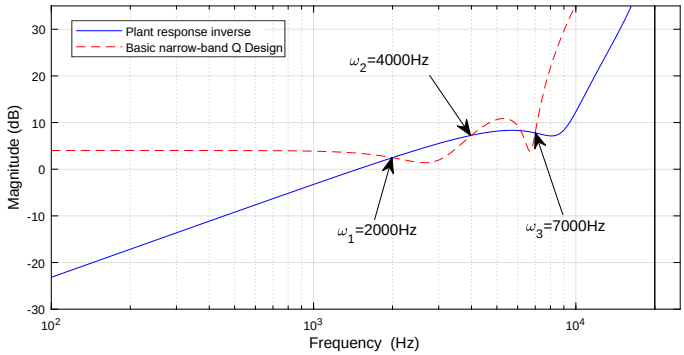

Figure 3.5: Comparison of the inverse frequency response of the plant and frequency response of proposed Q filter.

Proposition 4 provides an FIR filter design that achieves the desired disturbance rejection at ω_i. However, because there is no constraint on the overall magnitude of Q, this basic solution can induce disturbance amplification when $\omega \neq \omega_i$, especially at frequencies far away from the target frequency. Meanwhile, at frequencies where large model uncertainties and mismatches exist, high-performance control intrinsically has to be sacrificed for robustness based on robust control theory. Thus, we

propose to incorporate special band-pass characteristics to maintain the magnitude of $Q(e^{j\omega})$ small when $\omega \neq \omega_i$.

We propose the following lattice-structure [69] band-pass filter

$$Q_{BP}(z) = 1 - \frac{1}{2^n}\prod_{i=1}^{n}\frac{(1+k_{2,i})(1+2k_{1,i}z^{-1}+z^{-2})}{1+k_{1,i}(1+k_{2,i})z^{-1}+k_{2,i}z^{-2}}, \tag{3.15}$$

where $k_{1,i} = -\cos\omega_i$ and $k_{2,i} = [1-\tan(B_{w,i}/2)]/[1+\tan(B_{w,i}/2)]$, and $B_{w,i}$ (in radian) is the 3-dB bandwidth of $Q_{BP}(z)$ centered around ω_i. It can be shown that $Q_{BP}(e^{j\omega_i}) = 1\ \forall i = 1,2,\ldots,n$.

Applying (3.15) to (3.11) gives the improved design

$$Q(z) = Q_{BP}(z)(b_0 + \sum_{l=1}^{2n-1} b_l z^{-l}), \tag{3.16}$$

which not only reserves the disturbance rejection properties, but also avoids amplification of noises in $d(k)$ outside the target frequency ranges.

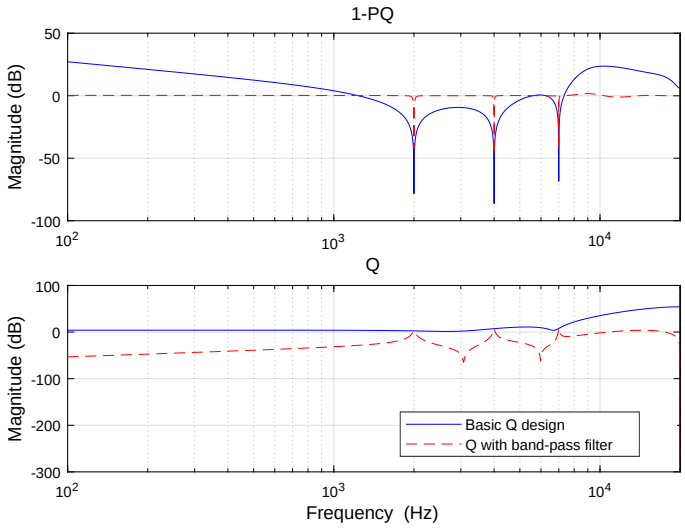

Figure 3.6: Comparison of frequency response for the Q filter with and without band-pass filter.

Applying the filter with center frequency $\omega = \begin{bmatrix} 0.1\pi & 0.2\pi & 0.35\pi \end{bmatrix}$ and the width of passbands $B_{w,i} = 2\times 10^{-3}\pi$ (or 40Hz when $T_s = 2.5\times 10^{-5}$sec) to Example 5, we obtain the frequency responses of $1-PQ$ and Q in Fig. 3.6. Compared with the basic design via (3.11), the proposed

Q enhancement not only possesses the needed band-pass shape but greatly mitigates the large magnitude amplification of $1-PQ$ at frequencies far from the centers of the pass bands, especially at low and high frequencies.

3.5 Q Filter Design for Wide-band Disturbance

Compared with single-frequency excitations, wide-band disturbances (see, e.g., Fig. 3.7) induce widely spanned spectral peaks in the energy spectrum. For such disturbances, pointwise inversion of the plant alone will not generate satisfying result. The reason, as can be seen in Fig. 3.5, is that the slew rate of the frequency responses of $P^{-1}(z)$ and $Q(z)$ differ from each other at the intersection points. In other words, because $Q(e^{j\omega})$ only interpolates $1/P(e^{j\omega})$ at ω_i, when the frequency deviates from these points, the difference between $1/P(e^{j\omega})$ and $Q(e^{j\omega})$ increases quickly. As a result, the frequency response of $1-PQ$, both magnitude and phase, can easily fall out of the desired performance threshold. To address the limitation, we propose an augmented Q filter to minimize the frequency response of $1-PQ$ in each frequency band by controlling both $1-P(e^{j\omega})Q(e^{j\omega})$ and its derivative. This yields a selective Hermite interpolation [70] of $1/P(e^{j\omega})$ and expands significantly the approximation region.

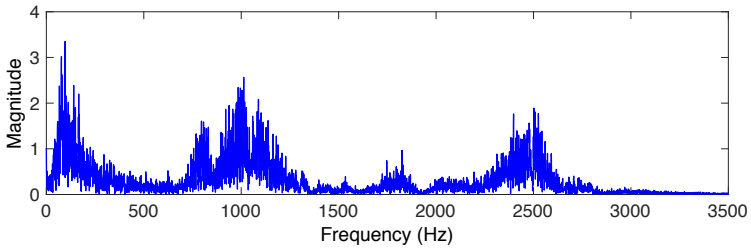

Figure 3.7: Example of wide-band disturbance spectrum [1].

Proposition 6. *Let $\omega_i \in (0,\pi)$, $i=1,2,\ldots,n$ be the center frequencies of the wide-band disturbance. Let (N,D) be a coprime factorization of $P(z)$ such that $P=ND^{-1}$, where $N=\sum_{u=0}^{p} c_u z^u$ and*

$D = z^q + \sum_{v=0}^{q-1} a_v z^v$. *Design* $Q(z) = b_0 + \sum_{l=1}^{m} b_l z^{-l}$ *with* $m = 4n-1$ *and*

$$\begin{bmatrix} b_0 \\ \vdots \\ b_m \end{bmatrix} = \begin{bmatrix} 1 & \cos\omega_1 & \cos 2\omega_1 & \dots & \cos m\omega_1 \\ 0 & \sin\omega_1 & \sin 2\omega_1 & \dots & \sin m\omega_1 \\ \vdots & & & & \vdots \\ 1 & \cos\omega_n & \cos 2\omega_n & \dots & \cos m\omega_n \\ 0 & \sin\omega_n & \sin 2\omega_n & \dots & \sin m\omega_n \\ 0 & \cos\omega_1 & 2\cos 2\omega_1 & \dots & m\cos m\omega_1 \\ 0 & \sin\omega_1 & 2\sin 2\omega_1 & \dots & m\sin m\omega_1 \\ \vdots & & & & \vdots \\ 0 & \cos\omega_n & 2\cos 2\omega_n & \dots & m\cos m\omega_n \\ 0 & \sin\omega_n & 2\sin 2\omega_n & \dots & m\sin m\omega_n \end{bmatrix}^{-1} \begin{bmatrix} \frac{\Re P(e^{j\omega_1})}{|P(e^{j\omega_1})|^2} \\ \frac{\Im P(e^{j\omega_1})}{|P(e^{j\omega_1})|^2} \\ \vdots \\ \frac{\Re P(e^{j\omega_n})}{|P(e^{j\omega_n})|^2} \\ \frac{\Im P(e^{j\omega_n})}{|P(e^{j\omega_n})|^2} \\ -\Re H(e^{j\omega_1}) \\ \Im H(e^{j\omega_1}) \\ \vdots \\ -\Re H(e^{j\omega_n}) \\ \Im H(e^{j\omega_n}) \end{bmatrix}, \tag{3.17}$$

where

$$H(e^{j\omega}) = \frac{(qe^{jq\omega} + \sum_{v=1}^{q-1} v a_v e^{jv\omega}) N(e^{j\omega}) - \sum_{u=1}^{p} u c_u e^{ju\omega} D(e^{j\omega})}{N^2(e^{j\omega})},$$

then

$$\begin{cases} 1 - P(e^{j\omega_i}) Q(e^{j\omega_i}) & = 0 \\ \frac{\mathrm{d}}{\mathrm{d}\omega}(1 - P(e^{j\omega}) Q(e^{j\omega}))\mid_{\omega=\omega_i} & = 0. \end{cases} \tag{3.18}$$

Proof. The first equation in (3.18) has been proved in Proposition 4 and the resulting properties have been reserved in (3.17). We only need to assure $\frac{\mathrm{d}}{\mathrm{d}\omega}(1 - P(e^{j\omega}) Q(e^{j\omega}))\mid_{\omega=\omega_i} = 0$, i.e.,

$$\begin{aligned} & \frac{\mathrm{d}}{\mathrm{d}\omega}(1 - P(e^{j\omega}) Q(e^{j\omega}))\mid_{\omega=\omega_i} \\ =& -\frac{\mathrm{d}}{\mathrm{d}\omega}(P(e^{j\omega}) Q(e^{j\omega}))\mid_{\omega=\omega_i} \\ =& -(\frac{\mathrm{d}P(e^{j\omega})}{\mathrm{d}\omega} Q(e^{j\omega}) + \frac{\mathrm{d}Q(e^{j\omega})}{\mathrm{d}\omega} P(e^{j\omega}))\mid_{\omega=\omega_i} \\ =& 0. \end{aligned} \tag{3.19}$$

Note that $1 - P(e^{j\omega_i}) Q(e^{j\omega_i}) = 0$. Under Assumption 3 ($P(e^{j\omega_i}) \neq 0$), (3.19) becomes

$$(\frac{\mathrm{d}P(e^{j\omega})}{\mathrm{d}\omega} \frac{1}{P(e^{j\omega})} + \frac{\mathrm{d}Q(e^{j\omega})}{\mathrm{d}\omega} P(e^{j\omega}))\mid_{\omega=\omega_i} = 0,$$

i.e.,

$$\frac{\mathrm{d}Q(e^{j\omega})}{\mathrm{d}\omega}|_{\omega=\omega_i}=-\frac{1}{P^2(e^{j\omega})}\frac{\mathrm{d}P(e^{j\omega})}{\mathrm{d}\omega}|_{\omega=\omega_i}=\frac{\mathrm{d}}{\mathrm{d}\omega}\frac{1}{P(e^{j\omega})}|_{\omega=\omega_i}. \tag{3.20}$$

Given $Q(z)=b_0+\sum_{l=1}^{m}b_l z^{-l}$, the left hand side of (3.20) is

$$\frac{\mathrm{d}Q(e^{j\omega})}{\mathrm{d}\omega}\ |_{\omega=\omega_i}=-\sum_{l=1}^{m}b_l l\sin l\omega_i - j\sum_{l=1}^{m}b_l l\cos l\omega_i. \tag{3.21}$$

Given the FIR coprime factorization of $P=ND^{-1}$, the right hand side of (3.20) becomes

$$\begin{aligned}
&\frac{\mathrm{d}}{\mathrm{d}\omega}\frac{1}{P(e^{j\omega})}\ |_{\omega=\omega_i}\\
=&\frac{\mathrm{d}}{\mathrm{d}z}\frac{1}{P(z)}\frac{\mathrm{d}z(=e^{j\omega})}{\mathrm{d}\omega}\ |_{\omega=\omega_i}\\
=&\frac{\mathrm{d}}{\mathrm{d}z}\frac{D(z)}{N(z)}\frac{\mathrm{d}e^{j\omega}}{\mathrm{d}\omega}\ |_{\omega=\omega_i}\\
=&j\frac{\frac{\mathrm{d}}{\mathrm{d}z}D(z)N(z)-\frac{\mathrm{d}}{\mathrm{d}z}N(z)D(z)}{N^2(z)}z\ |_{z=e^{j\omega_i}}\\
=&j\frac{(qz^q+\sum_{v=1}^{q-1}va_v z^v)N(z)-(\sum_{u=1}^{p}uc_u z^u)D(z)}{N^2(z)}|_{\ z=e^{j\omega_i}}\\
=&jH(e^{j\omega_i}).
\end{aligned} \tag{3.22}$$

Matching the real and the imaginary parts of (3.21) and (3.22) for $i=1,2,\ldots,n$ gives the lower half of (3.17). There are $4n$ linear independent equations in (3.17), the minimum order of Q for the existence of a unique solution is $m=4n-1$. □

For implementation, one can either substitute $P(z)$ with $\hat{P}(z)$ in Proposition 6 and calculate $H(e^{j\omega})$ based on the analytic transfer function, or directly calculate the derivative of $P^{-1}(e^{j\omega})$ in (3.20) using a measured frequency response.

Corollary 7. *If (3.18) is true, then*

$$\frac{\mathrm{d}}{\mathrm{d}\omega}\left|1-P(e^{j\omega})Q(e^{j\omega})\right|\ |_{\omega=\omega_i}=0.$$

Proof. Assume that $1-P(e^{j\omega})Q(e^{j\omega})=A(\omega)e^{j\theta(\omega)}$, where $A(\omega)$ and $\theta(\omega)$ are the magnitude and the phase responses, respectively. Then

$$\frac{\mathrm{d}}{\mathrm{d}\omega}(1-P(e^{j\omega})Q(e^{j\omega}))=\frac{\mathrm{d}A(\omega)}{\mathrm{d}\omega}e^{j\theta(\omega)}+jA(\omega)\frac{\mathrm{d}\theta(\omega)}{\mathrm{d}\omega}e^{j\theta(\omega)}.$$

Note that $A(\omega_i) = 0$. The above equation then gives

$$\frac{\mathrm{d}}{\mathrm{d}\omega}(1 - P(e^{j\omega})Q(e^{j\omega}))\,|_{\omega=\omega_i} = \frac{\mathrm{d}A(\omega)}{\mathrm{d}\omega} e^{j\theta(\omega)}\,|_{\omega=\omega_i} = 0,$$

which is equivalent to

$$\frac{\mathrm{d}A(\omega)}{\mathrm{d}\omega} = \frac{\mathrm{d}}{\mathrm{d}\omega}\left|1 - P(e^{j\omega})Q(e^{j\omega})\right|\,|_{\omega=\omega_i} = 0.$$

□

Therefore, the Q filter design in (3.17) guarantees that the first-order derivative of the magnitude response of $1 - PQ$ is zero at the target frequencies.

Consider again Example 5. Fig. 3.8 shows the frequency response of the proposed wide-band $Q(e^{j\omega})$ from (3.17). Compared to the basic solution (3.12), the magnitude response of the filter matches the inverse magnitude response of $P(z)$ within wide frequency ranges around the target frequencies. Therefore, $\left|1 - Q(e^{j\omega})P(e^{j\omega})\right| < \varepsilon$ within a wide band for a prescribed performance threshold ε. Indeed, in the magnitude response of $1 - PQ$ (Fig. 3.9), the filter design that incorporates the derivative dynamics gives wider notch shapes at all three disturbance frequencies. A zoom-in view of the notch shape of $1 - PQ$ in linear scale shows that the proposed design for wide-band disturbance indeed achieves zero derivative at the target frequencies, thereby inducing wider-range disturbance attenuation.

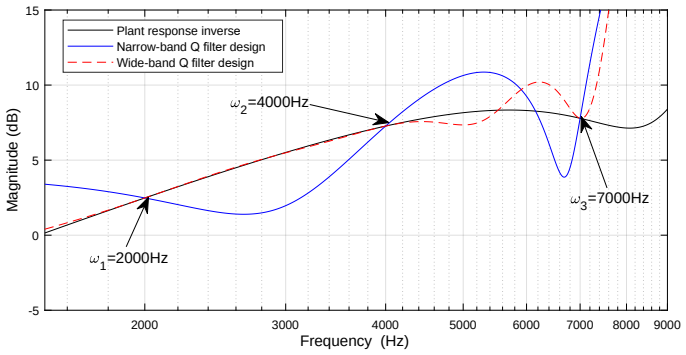

Figure 3.8: Comparison of magnitude response of Q for narrow- and wide-band designs.

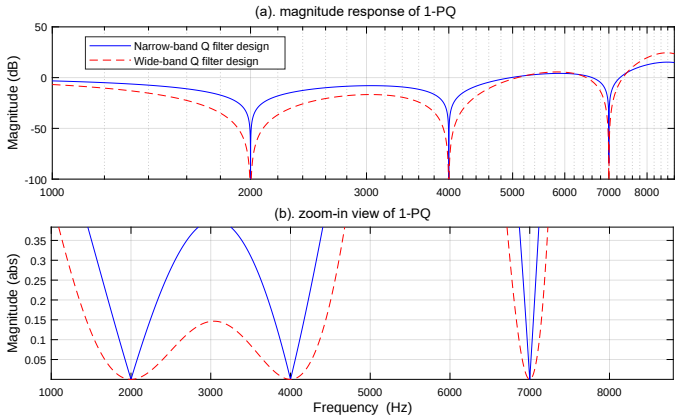

Figure 3.9: Comparison of magnitude response of $1-PQ$ for narrow- and wide-band designs. (a). Magnitude response of $1-PQ$. (b). Zoomed-in view of $1-PQ$.

Remark 8. (Extension to unstable plants) When P is unstable, instead of the discussed factorization $S=(1-PQ)/(1+PC)$, general Youla parameterization gives $S=(1-NQ/Y)/(1+PC)$, with $P=N/D$ and $C=X/Y$. The same design procedure applies to Q, with the replacement of P by N/Y in Proposition 4 and analogous modifications of H in Proposition 6.

3.6 Performance Limitation, Stability, and Robustness

Control of the waterbed effect

In Section 3.4, we proposed a band-pass filter that controls the undesired disturbance amplification. Note, however, that no practical band-pass filter is ideal (that is, having zero phase response and a rectangular magnitude response), especially when the passband gets wider. Therefore, it is infeasible for (3.16) to maintain 0 everywhere outside the target frequency bands. As a result, along with the desired notch shape, the magnitude of $1-P(e^{j\omega})Q(e^{j\omega})$ will exhibit the waterbed effect of exceeding 1. In this section, we discuss the frequency-domain closed-loop properties and how to control the relevant performance limitations.

Corollary 9. *Take any P and Q that are stable and causal. The magnitude response of* $1-P(e^{j\omega})Q(e^{j\omega})$

satisfies

$$\int_0^{\pi} \ln\left|1-P(e^{j\omega})Q(e^{j\omega})\right| \mathrm{d}\omega = \pi\left(\sum_{i=1}^{n_\gamma} \ln|\gamma_i| - \ln|\sigma+1|\right), \tag{3.23}$$

where $\{\gamma_i\}_{i=1}^{n_\gamma}$ $(n_\gamma \geq 0)$ *is the set of unstable zeros of* $1-P(z)Q(z)$ *(*$\{\gamma_i\}_{i=1}^{n_\gamma}$ *is the empty set if* $n_\gamma = 0$*), and*

$$\sigma = \lim_{z\to\infty} P(z)Q(z)/(1-P(z)Q(z)).$$

Proof. The proof is analogous to the one in [71] and is omitted here. □

For plants whose relative degree is zero, we have $\lim_{z\to\infty} P(z) \neq 0$. It is then possible that $\sigma > 0$ and the integral on the RHS of (3.23) is less than zero. However, for strictly proper plants (the more common case), $\lim_{z\to\infty} P(z) = 0$ and $\sigma = 0$; (3.23) simplifies to $\int_0^{\pi} \ln\left|1-P(e^{j\omega})Q(e^{j\omega})\right| \mathrm{d}\omega = \pi\sum_{i=1}^{n_\gamma} \ln|\gamma_i| \geq 0$. Then it is inevitable that there exist frequencies where $\left|1-P(e^{j\omega})Q(e^{j\omega})\right| > 1$. In other words, some disturbance energies are amplified in (3.7).

Although the overall area integral is constrained in (3.23), by proper structural design in $Q(z)$, the waterbed effect can be controlled based on the disturbance spectra, the performance goals, and the availability of accurate plant information in different regions. This is the primary reason for the band-pass design in (3.16). Further enhancement can be made, as we will now discuss in the following paragraphs.

The first method for enhanced waterbed control is to add fixed zeros to $Q(z)$ to constrain the magnitude of $1-P(e^{j\omega})Q(e^{j\omega})$. Fig. 3.10 shows the effect of placing a zero in $Q(z)$ near $z=1$ (DC gain). Recall the sensitivity function in (3.8). The induced small gain of $Q(e^{j\omega})$ at low frequency successfully reduces $\left|1-P(e^{j\omega})Q(e^{j\omega})\right|$ in the highlighted region in Fig. 3.10 and hence, reduces the magnitude response of the sensitivity function in (3.8) (note that at the same time, the induced fixed zero aggregates the disturbance amplification at high frequencies, due to the fundamental limitation described by (3.23)).

On the other hand, if the noise frequency is high, introducing a fixed zero near $z=-1$ provides enhanced small gain for $Q(e^{j\omega})$ at high frequencies. Furthermore, combined fixed zeros near the noise frequency can enhance the band-pass property. This method of zero modulation is especially effective when knowledge of noise spectrum in $d(k)$ is available.

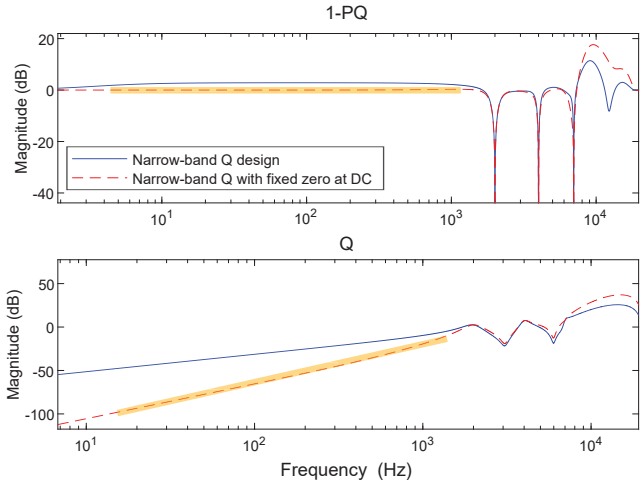

Figure 3.10: Effect of a fixed zero at low frequency region.

From the algorithmic viewpoint, a pair of fixed zeros $\rho e^{\pm j\omega_p}$, $\omega_p \in (0,\pi)$ translate to

$$Q(\rho e^{j\omega_p}) = b_0 + \sum_{l=1}^{m} b_l \left(\rho e^{j\omega_p}\right)^{-l} = 0,$$

namely

$$\Re Q(\rho e^{j\omega_p}) = b_0 + \sum_{l=1}^{m} b_l \frac{1}{\rho^l} \cos l\omega_p = 0$$
$$\Im Q(\rho e^{j\omega_p}) = \sum_{l=1}^{m} b_l \frac{1}{\rho^l} \sin l\omega_p = 0.$$

Two additional equations thus need to be added to (3.12):

$$\begin{bmatrix} 1 & \frac{1}{\rho}\cos\omega_p & \dots & \frac{1}{\rho^m}\cos m\omega_p \\ 0 & \frac{1}{\rho}\sin\omega_p & \dots & \frac{1}{\rho^m}\sin m\omega_p \end{bmatrix} \begin{bmatrix} b_0 \\ \vdots \\ b_m \end{bmatrix} = \begin{bmatrix} 0 \\ 0 \end{bmatrix}, \tag{3.24}$$

and the minimum order of $Q(z)$ becomes $m = 2n+1$ if $\omega_p \neq 0$ and $\omega_p \neq \pi$. When $\omega_p = 0$ or π, the second equation in (3.24) can be removed and the minimum order reduces to $m = 2n$. For the case with n_{p_0} added zeros at 0, n_{p_π} added zeros at π, and n_p added zeros elsewhere, the conditions for a minimum-order solution of $Q(z)$ are $m+1 = 2n+2n_p+n_{p_0}+n_{p_\pi}$, i.e., $m = 2n+2n_p+n_{p_0}+n_{p_\pi}-1$.

Another direct approach to reducing the overall waterbed amplification is to design first a regular Q filter in (3.11) and then detune the magnitude response by letting $\tilde{Q}(z) = kQ(z)$, $k \in (0, 1)$. Fig. 3.11 presents the effect of applying such a design with $k = 0.7$. The smaller gain at both low- and high-frequency regions shows that the amplification is indeed mitigated.

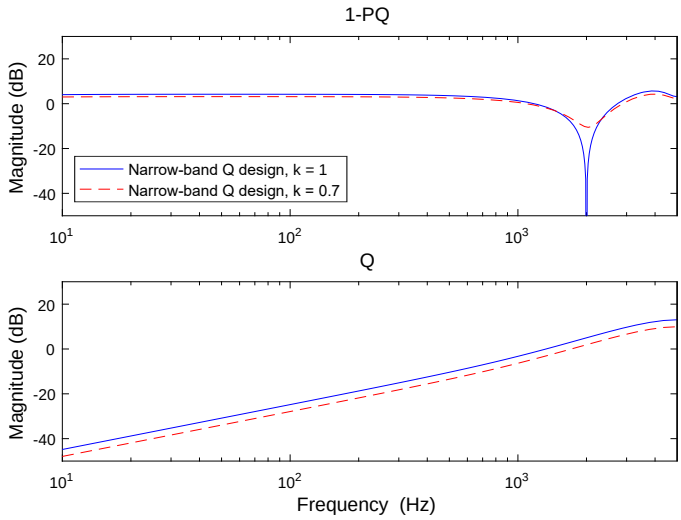

Figure 3.11: Effect of notch detuning for narrow-band loop shaping.

The proposed detuning relaxes the waterbed effect because unstable zeros of $1 - P(z)Q(z)$, if any, can be pulled into the unit circle by cascading the gain k. In fact, as $k \to 0$, the zeros of $1 - kP(z)Q(z)$ approximate the poles of $P(z)Q(z)$, which are all stable.

Stability and robustness

This section analyzes the closed-loop stability and robust stability of the proposed control scheme. For stability, we have the following result from closed-loop characteristic equation:

Proposition 10. *If $P(z)$ and $Q(z)$ are stable and $\hat{P}(z) = P(z)$, then the closed-loop system in Fig. 3.4 is stable.*

Proof. Apply block diagram analysis, we have the follwing relationships in Fig. 3.4

$$\begin{cases} U(z) = & -C(z)Y(z) \\ C(z) = & \left[((U(z)-C(z))(P(z)-\hat{P}(z))\right]Q(z) \\ Y(z) = & P(z)((U(z)-C(z))+D(z). \end{cases}$$

Eliminating $U(z)$ and $C(z)$ gives the closed-loop transfer function

$$Y(z)=\frac{1-P(z)Q(z)+Q(z)(P(z)-\hat{P}(z))}{1+P(z)C(z)+Q(z)(P(z)-\hat{P}(z))}D(z).$$

Let $P(z)=B_P(z)/A_P(z)$, $\hat{P}(z)=B_{\hat{P}}(z)/A_{\hat{P}}(z)$, $C(z)=B_C(z)/A_C(z)$, and $Q(z)=B_Q(z)/A_Q(z)$ be the coprime polynomial factorization of $P(z)$, $\hat{P}(z)$, $C(z)$, and $Q(z)$. When $\hat{P}(z)=P(z)$, the closed-loop characteristic equation becomes

$$A_Q(z)A_{\hat{P}}(z)[A_P(z)A_C(z)+B_P(z)B_C(z)]=0.$$

Hence the closed-loop poles are composed of the baseline closed-loop poles and the poles of $Q(z)$ and $\hat{P}(z)$. As the baseline feedback loop, $Q(z)$, and $\hat{P}(z)$ (=$P(z)$) are all stable, the new closed loop is thus stable. □

For *robust stability*, when the plant is perturbed to be $\tilde{P}(z)=P(z)(1+\Delta(z))=\hat{P}(z)(1+\Delta(z))$ (the uncertainty $\Delta(z)$ is assumed to be stable and has a bounded $\mathscr{H}_\infty$ norm), applying the Small Gain Theorem yields the following robust-stability condition

$$\|\Delta(z)T(z)\|_\infty < 1, \tag{3.25}$$

where T is the nominal complementary sensitivity function satisfying $T=1-S$. After substituting in (3.8), (3.25) becomes

$$\left\|\Delta(z)P(z)\frac{C(z)+Q(z)}{1+P(z)C(z)}\right\|_\infty < 1.$$

(3.25) implies that in order to preserve the robust stability, magnitude of the plant uncertainty has to be lower than that of $1/T(z)$. Fig. 3.12 shows the magnitude response of $1/T(z)$ when rejecting disturbance at 4000 Hz for the plant in (3.14) with different Q designs. The upper plot

indicates that compared to the baseline open-loop system, introducing the proposed FMSDOB largely preserves the robust stability bounds. The minimal value of $|\ 1/T(z)\ |$ for both the narrow- and wide-band designs is -0.15 dB at around 4097 Hz, i.e., the plant uncertainty can be as large as 98.3% at all frequencies without causing instability. The necessity of the band-pass filter in (3.15) is evident from the lower plot. Without the filter, the minimal value of $|\ 1/T(z)\ |$ decreases to -2.9 dB (71.6%) at the low-frequency region for narrow-band design and -12.82 dB (22.9%) at around 9001 Hz for wide-band design.

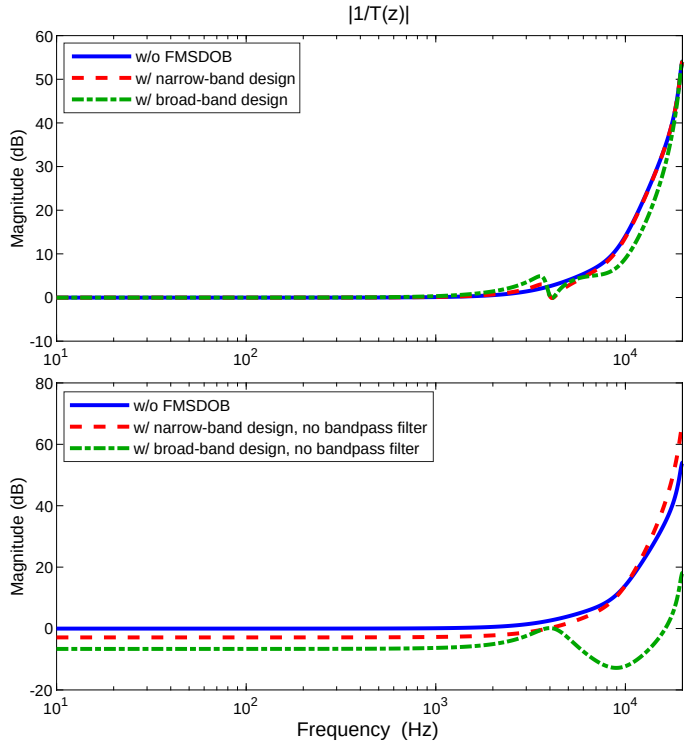

Figure 3.12: Magnitude response of $1/T(z)$, defines the upper bounds for plant uncertainty to preserve robust stability.

When rejecting multiple, especially wide-band and high-frequency disturbances, the requirement on the magnitude of uncertainty can be stringent to assure the stability. Such a trade-off between performance and robustness is more significant for nonminimum-phase system (recall (3.23)).

Engineering practice can balance such trade-offs by leveraging the proposed band-pass filter, detuning factor, and sometimes a low-pass filter that turns off the compensation at high frequency region. In Section 3.7, we provide an example implementation of the algorithm subject to model mismatch, and show that high performance can still be maintained with the design flexibility of the algorithms.

Summary and application recommendations

This section summarizes the theoretical results discussed above. We proposed a disturbance rejection scheme that can be used in systems with nonminimum-phase zero(s). Under this framework, two Q-filter designs based on local plant dynamics have been introduced. In general, when the disturbance energy concentrates at one or several individual frequencies, the narrow-band design in (3.12) is sufficient to reject the disturbance without introducing severe deterioration at other frequencies. The wide-band design as described in (3.17) is ideal when the disturbance energy spans over wide frequency bands.

The proposed scheme suits particularly for disturbance rejection that desires the following algorithmic properties:

- *No direct plant inversion*: The proposed design eliminates the parasitic complexity associated to a direct plant inversion in feedback applications. For instance, in a regular DOB, a plant cannot be directly inverted with the presence of nonminimum-phase zeros. In this case, a stable approximate inversion $\hat{P}^{-1}(z)$ is used. In the frequency region where large mismatch exists between $P^{-1}(z)$ (potentially unstable and unrealizable) and $\hat{P}^{-1}(z)$, the Q filter must be designed to have small gain and cannot successfully reject disturbance at that region. Such an explicit inverse model is not needed in the proposed FMSDOB. Based on (3.10), Q is a local pointwise inverse, which avoids the constraint of "fail region" induced by the mismatch discussed above.

- *Flexibility and accuracy:* Compared with existing plant inversion algorithms for nonminimum-phase system, the proposed method offers new flexibility and accuracy to feedback controls.

The proposed pointwise inverse allows for full disturbance rejection at selective regions. The design of Q requires only selective frequency responses (right hand side of (3.12) and (3.17)) instead of an inverse tranfer-function plant model, which may be difficult or even infeasible in practice.

- *Design intuition, performance, and extensions*: A regular inverse-based DOB structure with low-pass Q design focuses more on the magnitude and does not explicitly consider the phase compensation that can significantly deteriorate the achievable performance at high frequencies. In contrast, both the magnitude and phase compensations are taken into consideration in (3.9). Compared with other loop-shaping algorithms, the proposed scheme inherits the advantages of flexible intuitive design and high performance of the DOB [47, 58]. It also shares the capability of easy adaptation [58, 72]

Certainly, any control design is subject to trade-offs in practice. The fundamental limits of feedback control and plant uncertainties should still be respected. In practice, we recommend to test the basic solutions in Section 3.4 and Section 3.5 first and when the "waterbed"-induced amplifications are severe in the basic solutions, one can use such enhancement techniques as band-pass filters, fixed zeros, and tuning factors based on the disturbance spectra. We recommend to start with a baseline feedback loop (e.g., by forming a PID or H_∞ controller C in Fig. 3.4), then to iterate the LLS design until a satisfying frequency response of $1 - PQ$ is obtained.

3.7 Experiment Verification

In this section, we verify the proposed scheme for both narrow- and wide-band loop shaping in the laser beam steering for LPBF. Along the way, we compare the efficiency of the proposed FMSDOB with the conventional inverse-based DOB. We perform both simulation and experiment verification. In the simulation, an estimated plant model is used to build the scheme in Fig. 3.4 in MATLAB simulink. In the experiment, a dSPACE DS1104 board connects control designs in MATLAB with the servo drivers to send control signal and read position feedback in real time.

Galvo scanner platform

The experiment is performed on a galvo scanner platform, which is composed of two sets of mirrors, galvanometers, and control driver. The driver circuit diagram is shown in Fig. 3.13. The input signal is sent to the scanner drive stage circuit after passing through the input conditioning circuit. The position of the shaft (and it's attached mirror) is derived from the photo detector in the position detection circuit, which sends that signal to a position correction circuit. The position correction circuit compares the actual position of the mirror, with the position the mirror should be in according to the signal from the input conditioning circuit. It then generates an error correction signal and sends that to the scanner drive stage where it is combined with the input signal. The drive stage provides the current to the coils in the scanner to move the mirror. Therefore, the control circuit forms a closed-loop system from the control signal input (voltage) to the detected position signal (voltage). The closed-loop transfer function $\frac{L(z)}{1-L(z)}$ can be identified via system identification (see [73]) and the open loop transfer function $L(z)$ is interpreted as the plant dynamics $P(z)$ in the experiments.

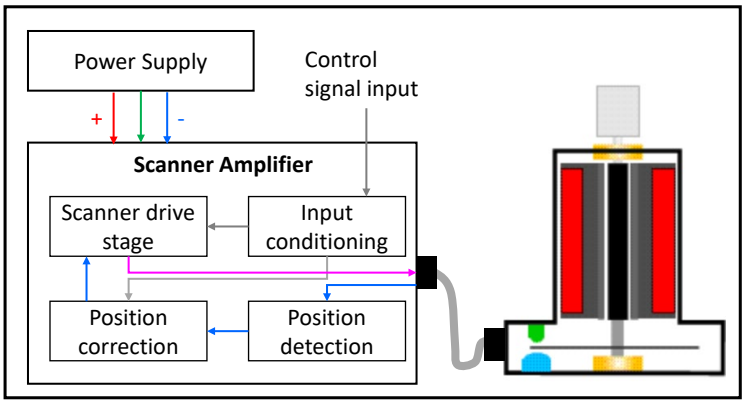

Figure 3.13: Galvo scanner embedded control diagram [2].

3.7.1 Narrow-band loop shaping and performance comparison

For a fair comparison with conventional inverse design algorithms we sample the system at a sampling time of $T_s = 1 \times 10^{-4}$ sec, yielding the following nominal model without unstable zeros:

$$\hat{P}(z) = \frac{0.5465z^3 + 0.4598z^2 - 0.0717z - 0.0721}{z^4 - 0.5221z^3 - 0.6208z^2 + 0.0730z + 0.0721}.$$

We set $C(z) = 1$ because a vendor-integrated baseline controller is already embedded in $P(z)$.

The measured and identified frequency responses are shown in Fig. 3.14. The identified model $\hat{P}(z)$ matches the measured response up to 10^4 Hz.

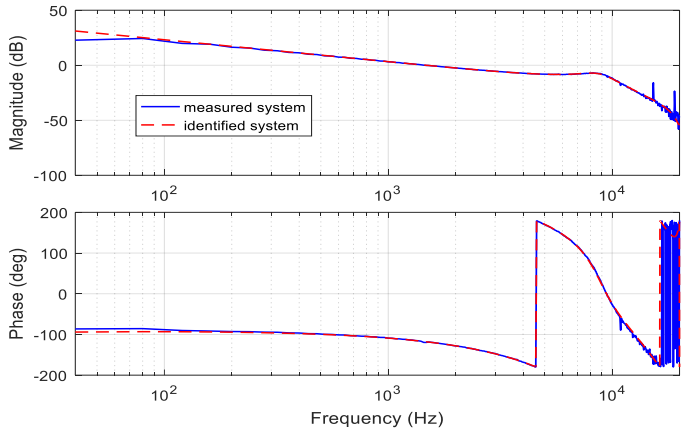

Figure 3.14: Frequency response of galvo scanner system..

A series of time-varying narrow-band vibrations is considered in both simulation and experiment. The disturbance frequency varies in the pattern of null→ 500 Hz→ 1500 Hz→500 Hz→3000 Hz→ 500 Hz→ null with step frequency changes between each disturbance section. The first disturbance is injected at 0.5 s and the duration time for each frequency is 0.3 s. The amplitude of the disturbance is 0.1 volt. The inherent disturbance estimation and local loop shaping design in the proposed algorithm enable easy adaptation of the controller parameters. Fig. 3.15 presents the online identified frequencies using a parameter adaptation algorithm (PAA) detailed in [58].

The upper plot of Fig. 3.16 shows the simulated time trace of the residual position errors. The proposed algorithm using a $Q(z)$ filter in (3.16), with the bandwidth of the lattice band-pass filter

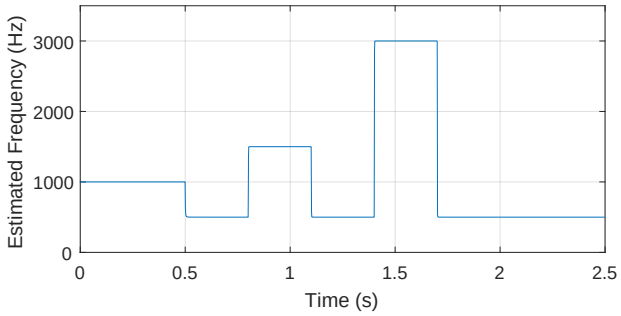

Figure 3.15: Identified frequencies using parameter adaptation algorithm.

Table 3.1: 2-NORM OF BASELINE NOISE AND RESIDUAL ERRORS.

Period (s)	0.39→0.49 (Baseline)	0.69→0.79 (500 Hz)	0.99→1.09 (1500 Hz)
$\|e_r\|_2^2$ ($\times 10^{-1}$V^2)	1.652	1.451	1.373
Period (s)	**1.29→1.39 (500 Hz)**	**1.59→1.69 (3000 Hz)**	**1.89→1.99 (500 Hz)**
$\|e_r\|_2^2$ ($\times 10^{-1}$V^2)	1.485	1.521	1.458

set as 50 Hz, is seen to provide rapid and strong vibration attenuation. Inspection of data at 0.79 s, 1.09 s, and 1.69 s indicates that the steady-state position errors indeed converge to zero. The experimental results of rejecting the same disturbance is shown in the lower plot of Fig. 3.16. There, the compensation scheme reduces steady-state errors to the same as or even smaller than the baseline case. This is also verified by calculating the 2-norm of the steady-state errors (denoted as $\|e_r\|_2^2$) in the time windows indicated by the dashed frames in the lower plot of Fig. 3.16. The corresponding results are given in Table 3.1. The physical system has nonstationary noises from the electric circuits and the operation environments, as well as small nonlinearities in position sensing (e.g., in the magnitude of mrad per optical/44°), hence the minor statistical variations in the numbers

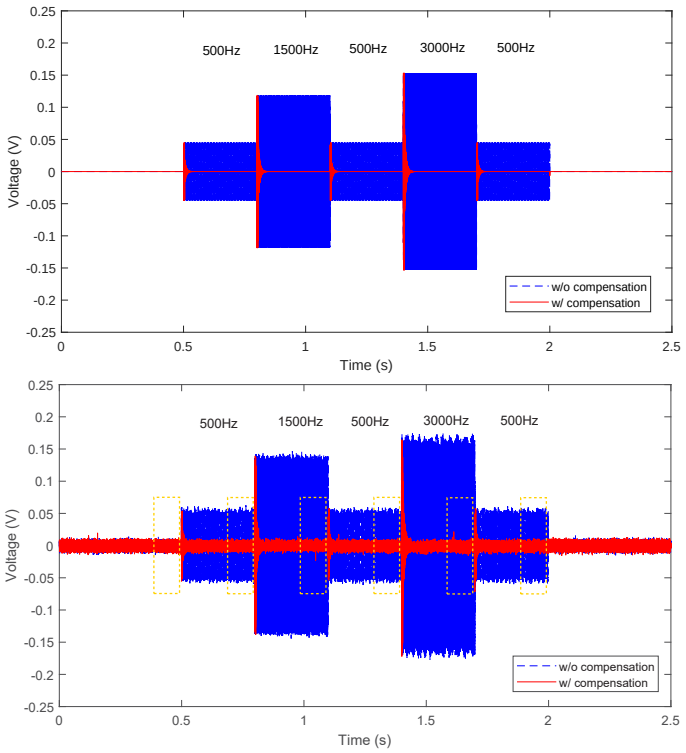

Figure 3.16: Simulation (upper plot) and experimental (lower plot) results of rejecting narrow-band disturbance with single step changing frequency.

in Table 3.1. Yet the controller has maintained its effectiveness in all time periods. For large-range motions, major galvo scanner vendors provide image field correction algorithms that can eliminate nonlinear scanning errors.

The steady-state error spectra further reveals the effectiveness of the proposed scheme. Fig. 3.17 shows that when the system is subjected to a 1500 Hz vibration, the proposed scheme reduces the spectral peak from around -18 dB to -101 dB, indicating an attenuation of about 83 dB. This is directly reflected by the red dashed line in Fig. 3.18(a). The sensitivity function with the proposed scheme exhibits a deep notch at 1500 Hz and at the same time, almost no amplification at other frequencies compared to the baseline case.

Despite that the galvoscanner system has highly accurate plant dynamics, to reveal robustness of

the proposed method, we perturbed the plant dynamics $P(z)$ by an uncertainty $\Delta(z)$ that is bounded by $\|1/T(z)\|_\infty$ (Fig. 3.18(c)). The weight of the uncertainty is filtered by a highpass filter so that it is

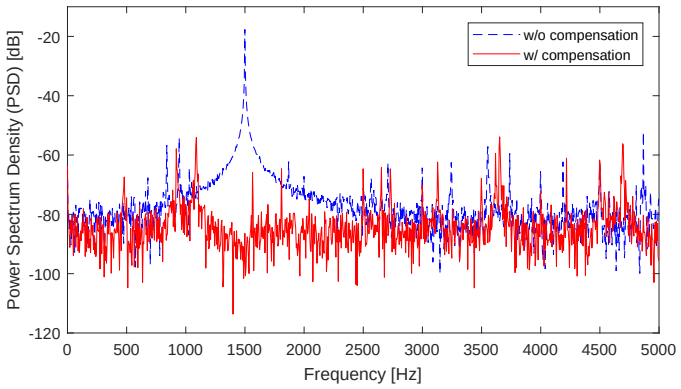

Figure 3.17: Experimental results of error spectra of rejecting a 1500 Hz vibration.

more significant at high frequencies and reaches maximum ($\|1/T(z)\|_\infty$) near the Nyquist frequency. Fig. 3.18(d) plots the Nyquist plot of $L(z) = \tilde{P}(z)C_{eq}(z)$, where $\tilde{P}(z)$ is the perturbed plant and $C_{eq}(z)$ is the equivalent feedback controller of the proposed scheme given by (3.6). Clearly, the perturbed plots remain far away from the point $(-1,0)$ and the original encirclement is not violated. In other words, the system remains robustly stable under the large perturbations. Fig. 3.18(a) and 3.18(b) show the impact of uncertainty on feedback performance. The magnitude response of the sensitivity function fluctuates slightly at regions of high uncertainties; however, the designed notch at 1500 Hz is largely preserved and the algorithm still successfully rejects the narrow-band disturbance. Note that if the plant uncertainty is large enough to violate (3.25), the closed-loop stability and disturbance rejection performance cannot be guaranteed and high-performance control intrinsically has to be traded off to robust stability.

Two more simulation tests are conducted with increased disturbance complexity. The disturbances now contain, respectively, two and three frequency components in each period. The corresponding time series of the residual errors are shown in Fig. 3.19. Again, one can observe that the proposed scheme achieves the desired disturbance rejection rapidly.

The aforementioned regulation performance transforms analogously to tracking control with

a nonzero reference. For laser scanning in additive manufacturing, Fig. 3.20 shows the rejection of two narrow-band frequencies when r in Fig. 3.4 (red solid line in Fig. 3.20) is a periodic in-fill pattern (e.g., the WEAVE scanning [4]). It can be seen that the disturbances are rapidly rejected similar to the regulation performance.

Fig. 3.21 compares the proposed algorithm with a conventional DOB [58] and presents the results of rejecting the disturbance series described in Fig. 3.19(a). Both methods achieve zero steady-state error. However, a zoom-in view in the lower plot of Fig. 3.21 shows that the average transient magnitude of the proposed scheme is lower than that of inverse-based DOB. This is further evaluated by computing two quantitative values: the 2-norm values of the transient errors (denoted as $\|e_t\|_2^2$) within the initial 15ms after injection of compensation signal (indicated by yellow dashed frames in Fig. 3.21) and the maximum values of residual errors (denoted as $|e_r|$, the corresponding time windows are marked by green dashed frames in Fig. 3.21). The results are presented in Table 3.2. The proposed algorithm yields better performance than the conventional DOB in both transient and steady-state responses, due largely to the inversion of the plant dynamics at only the needed locations.

3.7.2 Wide-band disturbance

We now increase the sampling frequency of the system to obtain

$$\hat{P}(z) = \frac{0.0282z^2 + 0.1504z + 0.1146}{z^4 - 1.3190z^3 + 0.929z^2 - 0.6073z - 0.0035},$$

with $T_s = 2.5 \times 10^{-5}$ s. Note that this is a nonminimum-phase system with an unstable zero at $z = -4.419$.

To illustrate the performance of rejecting wide-band vibrations, we feed a mockup disturbance signal (Fig. 3.22) as $d(k)$ in Fig. 3.4. The disturbance mockup is a scaled version of actual acoustic vibrations in high precision motion systems (Fig. 3.7), with three wide peaks centered around 100 Hz, 900 Hz, and 2500 Hz.

The baseline sensitivity function is capable to attenuate low-frequency disturbances. Thus, in the Q filter design, we only focus on the two faster disturbances (900 Hz and 2500 Hz). Fig.

Table 3.2: RESULTS OF DISTURBANCE REJECTION WITH FMSDOB AND INVERSE-BASED DOB.

Algorithm	**freq.** (kHz)	$\|e_t\|_2^2$ ($\times 10^{-1}$V^2)	max$\|e_r\|$ ($\times 10^{-5}$ V)
FMSDOB	null$\rightarrow$[0.9, 2.0]	0.788	0.748
	[0.9, 2.0]$\rightarrow$[1.5, 2.6]	3.083	1.478
	[1.5, 2.6]$\rightarrow$[0.9, 2.0]	4.477	1.596
	[0.9, 2.0]$\rightarrow$[2.1, 3.2]	3.663	1.215
	[2.1, 3.2]$\rightarrow$[0.9, 2.0]	3.454	1.845
Inverse DOB	null$\rightarrow$[0.9, 2.0]	2.280	1.348
	[0.9, 2.0]$\rightarrow$[1.5, 2.6]	4.338	2.817
	[1.5, 2.6]$\rightarrow$[0.9, 2.0]	5.380	3.012
	[0.9, 2.0]$\rightarrow$[2.1, 3.2]	5.049	2.594
	[2.1, 3.2]$\rightarrow$[0.9, 2.0]	5.696	3.405

3.23 shows the frequency responses of the Q filter and $1 - PQ$. As expected, two wide attenuation notches are located at the target frequencies in the upper plot. The red dashed line shows the result of applying lattice band-pass filters for mitigating the waterbed effect at high frequencies. The frequency domain disturbance rejection result is shown in Fig. 3.24. We can see that both the open- and closed-loop systems reject the energy peak at 100Hz thanks to the baseline sensitivity function; as the disturbance frequency increases, the baseline control becomes ineffective. On the other hand, the proposed scheme is able to effectively attenuate the large spectral peaks. The time series in Fig. 3.25 further show the significant performance of the proposed scheme, with a 3σ value of the residual position error as low as 0.38 compared with 0.90 in the baseline system (a 57% reduction).

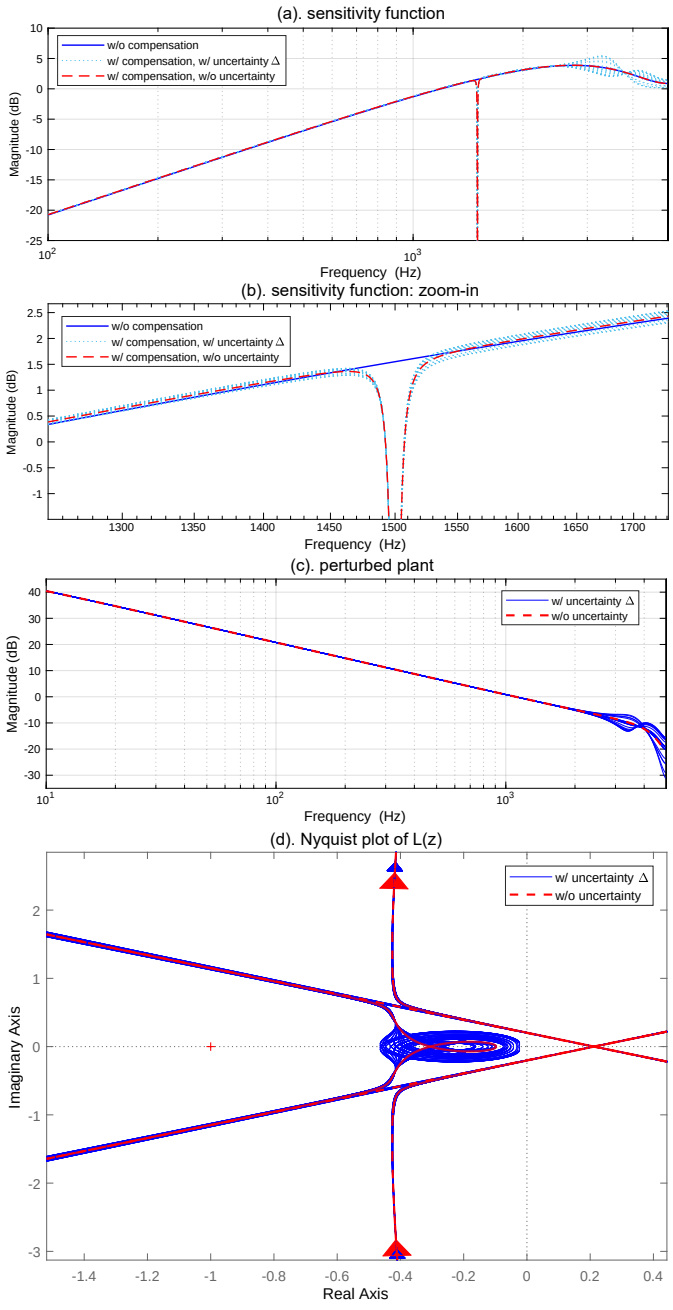

Figure 3.18: Sensitivity functions comparison and robust stability analysis: (a). magnitude responses of the sensitivity functions under different conditions; (b). zoom-in view of sensitivity function around distrubance frequency; (c). perturbed plant dynamics; (d). Nyquist plot of $L(z) = \tilde{P}(z)C_{eq}(z)$.

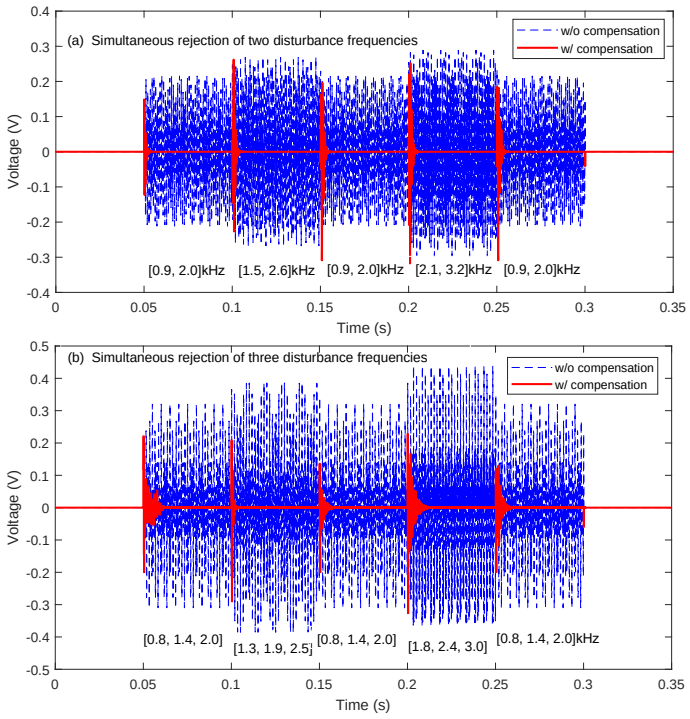

Figure 3.19: Simulation results of rejecting narrow-band disturbances with two (upper) and three (lower) step changing frequencies.

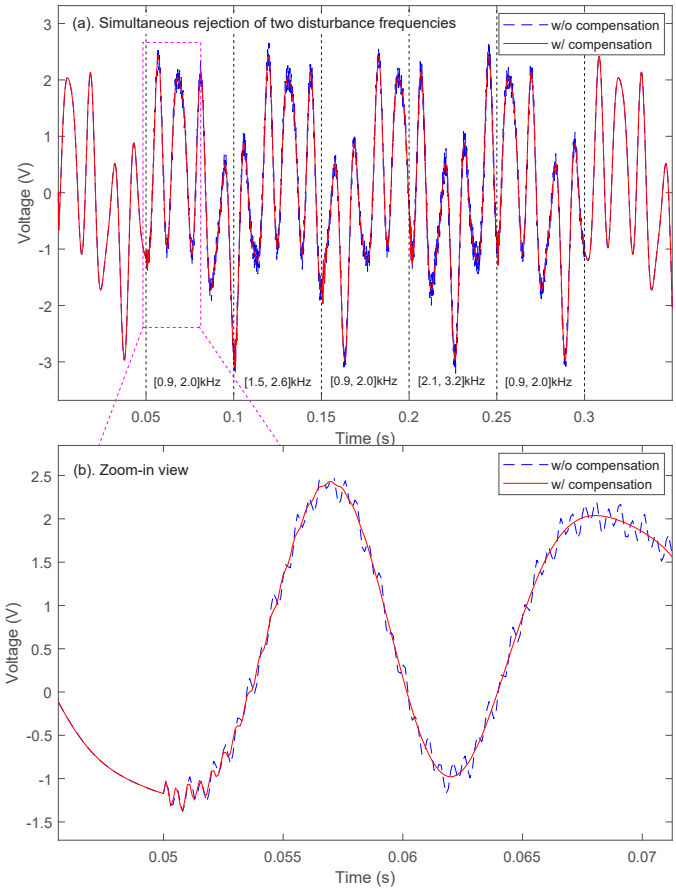

Figure 3.20: Simulation results of rejecting narrow-band disturbances with two step changing frequencies with nonzero input.

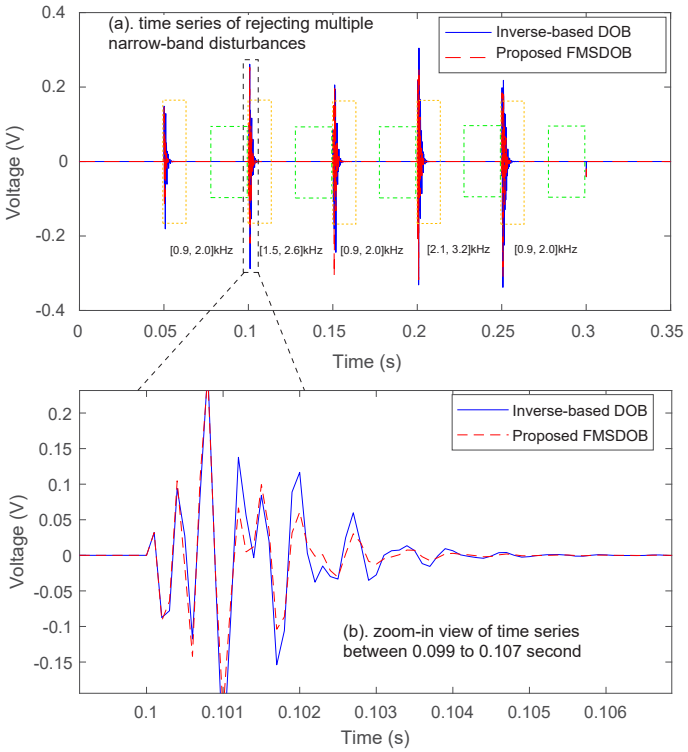

Figure 3.21: Comparison of FMSDOB and inverse-based DOB on rejecting disturbance with multiple narrow-band frequencies.

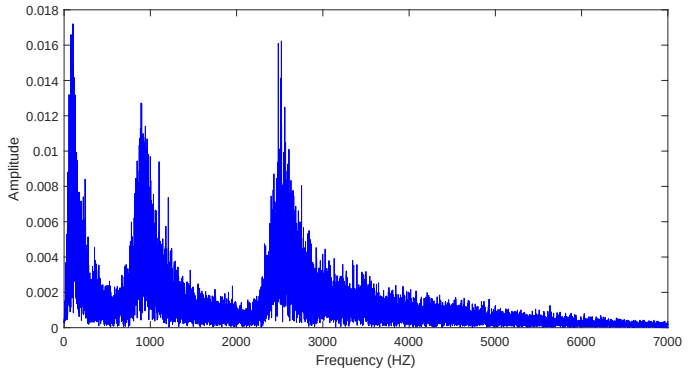

Figure 3.22: Wide-band disturbance in simulation.

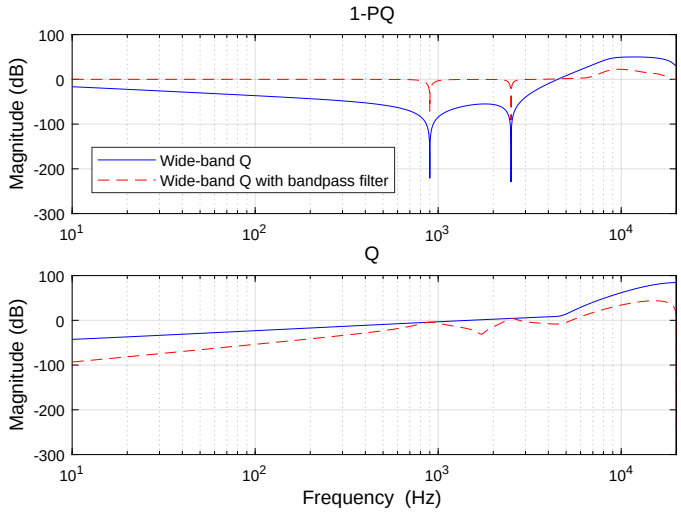

Figure 3.23: Magnitude response of the 1-PQ and Q with wide-band filter design.

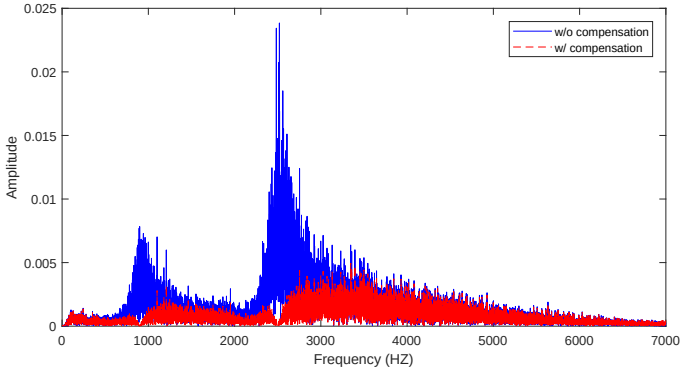

Figure 3.24: Spectrum comparison with and without the proposed wide-band Q compensator.

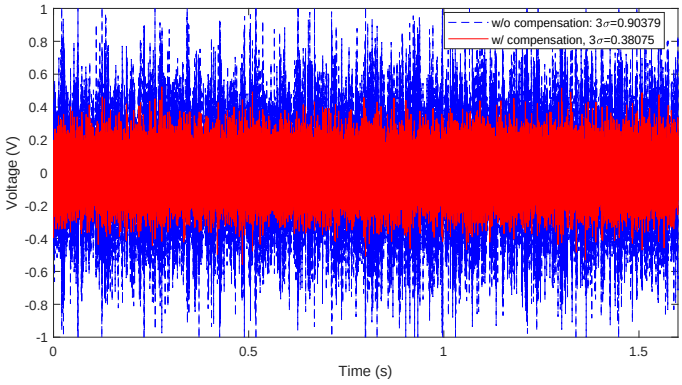

Figure 3.25: Performance of the wide-band Q filter in time domain.

Chapter 4

MULTI-ZONE CONTROL FOR POWDER BED THERMAL DISTURBANCE

4.1 Introduction

In LPBF of polymer materials, after powder recoating, the powder bed surface is preheated to a temperature close to the material's melting point before the laser scanning. The purposes of such preheating are:

1. To reduce cooling rate between the fused area and surrounding unfused powder and prevent defects such as balling and shrinkage.

2. To increase the laser scanning speed as the majority (usually >95%) of the energy required for the phase transition is deposited by the heater.

It is essential to achieve a homogeneous temperature profile across the powder bed with preheating as any thermal diffrence can directly transfer into the part mechanical property inhomogeneities. A significant thermal disturbance source in LPBF is the heating-cooling cycle of previously fused layers. The conducted heat from these layers largely defines the temperature profile of the surface layer. Such cross-layer thermal disturbance is particularly harmful to parts with abrupt geometric changes, such as overhang structures. In [74], we show that the melting pool width at the area with previously processed layers can be three times as large as that at the outside.

Homogeneous powder bed temperature is contingent on both heater design and control algorithm. In most polymer LPBF systems, radiative or/and resistive heaters are present for preheating. The resistive heater maintains an elevated ambient temperature and heats the powder via thermal convection. However, the convection dynamics are relatively slow and not efficient. On the other

hand, the radiative heater transfers energy at a much higher rate because it works at a significantly higher temperature than the powder bed surface.

Based on the number of individually controllable heating zones and the number of temperature sampling points on the powder bed, the IR heating system has the following possible configurations:

- SISO (single-input-single-output): one heating zone (or multiple heating zones with the same power setting), temperature measurement at one point or as an average.
- MISO (multi-input-single-output): multiple individually controllable heating zones, temperature measurement at one point or as an average.
- MIMO (multi-input-multi-output): multiple individually controllable heating zones, temperature measurement at multiple points.

The SISO configuration is most common in the state-of-the-art platforms. [19] shows that with such a configuration, the radiant heater has a very inhomogeneous temperature distribution and is not able to realize a homogeneous temperature distribution on the powder bed surface. With a reference temperature set as 174°C for PA2200, the deviation between the minimum and maximum powder bed temperature is as high as 7.5 °C, without cross-layer part geometry-induced thermal disturbance. In MISO configuration, different heating zones can have different controller gains to obtain homogeneous temperature distribution with a single temperature measurement.

Compared with SISO and MISO, the MIMO configuration is more flexible and intuitive. By controlling the heating power of multiple zones separately, the temperature at multiple sampling locations on the powder bed can be regulated simultaneously, rending the problem of global temperature deviation control as local deviation control. In this chapter, we created a control-oriented model for such a configuration. We proposed a multi-zone heating algorithm utilizing the decoupled form of this heating model. In the experiment, we compared its performance with SISO configuration and model predictive control (MPC) in the presence of different cross-layer thermal disturbances. Along this process, we also demonstrated the flexibility of the proposed design by incorporating an add-on parameter tuning scheme that is adaptive to the thermal disturbance profile.

Table 4.1: PARAMETERS OF POWDER BED HEAT TRANSFER GOVERNING EQUATION.

Parameter	Description	Unit
ρ	powder density	$\mathrm{kg/m^3}$
c_p	specific heat capacity	$\mathrm{J/kg/K}$
d	layer thickness	m
h_c	convection heat transfer coefficient	$\mathrm{W/m^2/K}$
ε	emissivity	n/a
σ_B	Stefan-Boltzmann constant	$\mathrm{W/m^2/K^4}$
q	input heat flux from a heating zone	$\mathrm{W/m^2}$
T_e	ambient temperature	K

The remainder of this chapter is organized as follows. Section 4.2 develops the model of multi-zone infrared heating. Section 4.3 describes the proposed multi-zone heating algorithm and the comparison algorithms–SISO control and MPC. Section 4.4 presents the experiment results on preheating PA12 material with different initial powder bed thermal profiles.

4.2 Multi-zone IR Heating Modeling

Fig. 4.1 illustrates the heat transfer processes during radiation heating. Consider a small target area A on the powder bed with the thickness of one layer d. The governing equation of the temperature for this area is:

$$\rho d c_p \frac{\mathrm{d}T(t)}{\mathrm{d}t} = q(t) + h_c\left(T_e - T(t)\right) + \varepsilon\sigma_B\left(T_e^4 - T^4(t)\right) \tag{4.1}$$

where the relevant parameters are described in Table 4.1. The term $h_c\left(T_e - T(t)\right)$ on the right hand side of (4.1) characterizes the heat convection between the powder surface and the ambient atmosphere. The term $\varepsilon\sigma_B\left(T_e^4 - T^4(t)\right)$ represents the heat input due to radiation. The governing equation ignores the heat conductivity in all three dimensions as the thermal conductivity coefficient of the powder material is low, and the dynamics are relatively slow.

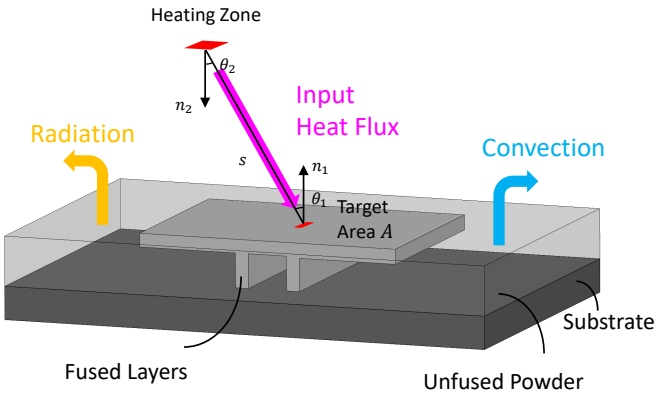

Figure 4.1: Schematic illustration of thermal transfer processes during preheating.

Assume that the power of the heating zone in Fig. 4.1 is u, then the heat flux absorbed by the target area can be expressed as

$$q(t) = F\varepsilon u(t) \tag{4.2}$$

where F is the view factor, defined as the proportion of the radiation which leaves the heating zone and strikes the target area A. It can be modeled as

$$F = \frac{\cos\theta_1 \cos\theta_2}{\pi s^2} = \frac{\cos^2\theta}{\pi s^2} \tag{4.3}$$

where θ is the angle between the surface normals and the ray between the heating zone and target area and s is their distance.

Proposition 11. *Given n heating zones and m target areas on the powder bed. The state space*

model of the heating process is an n-input-m-output system

$$\begin{gathered}\frac{\rho dc_p}{k_1}\frac{\mathrm{d}}{\mathrm{d}t}\begin{bmatrix}\tilde{T}_1(t)\\ \tilde{T}_2(t)\\ \vdots\\ \tilde{T}_m(t)\end{bmatrix} = I_{m\times m}\begin{bmatrix}\tilde{T}_1(t)\\ \tilde{T}_2(t)\\ \vdots\\ \tilde{T}_m(t)\end{bmatrix} + \varepsilon\begin{bmatrix}F_{11} & F_{21} & \cdots & F_{n1}\\ F_{12} & F_{22} & \cdots & F\\ \vdots & \vdots & \ddots & \vdots\\ F_{1m} & F_{2m} & \cdots & F_{nm}\end{bmatrix}\begin{bmatrix}u_1(t)\\ u_2(t)\\ \vdots\\ u_n(t)\end{bmatrix}\\ \begin{bmatrix}y_1(t)\\ y_2(t)\\ \vdots\\ y_m(t)\end{bmatrix} = I_{m\times m}\begin{bmatrix}\tilde{T}_1(t)\\ \tilde{T}_2(t)\\ \vdots\\ \tilde{T}_m(t)\end{bmatrix}\end{gathered} \tag{4.4}$$

where $\tilde{T}_i(t) = k_1 T_i(t) + k_2$*,* $T_i(t)$ *is the temperature of target area i,* $u_j(t)$ *is the power of heating zone j,* F_{ji} *is the view factor between heating zone j and target area i,* $k_1 = -(h_c + 4\varepsilon\sigma_B T_0^3)$*,* $k_2 = h_c T_e + \varepsilon\sigma_B T_e^4 + 3\varepsilon\sigma_B T_0^4$*, and* T_0 *is the reference preheating temperature.*

Proof. Consider a target area i, when there are n heating zones, combining (4.1) and (4.2) gives

$$\rho dc_p \frac{\mathrm{d}T_i(t)}{\mathrm{d}t} = \varepsilon\begin{bmatrix}F_{1i} & F_{2i} & \cdots & F_{ni}\end{bmatrix}\begin{bmatrix}u_1(t)\\ u_2(t)\\ \vdots\\ u_n(t)\end{bmatrix} + h_c\left(T_e - T_i(t)\right) + \varepsilon\sigma_B\left(T_e^4 - T_i^4(t)\right) \tag{4.5}$$

Select a working temperature point T_0, the nonlinear term of the right hand side can be linearized as $T_i^4(t) = T_0^4 + 4T_0^3\left(T_i(t) - T_0\right)$. Replacing the state variable $T_i(t)$ with $\tilde{T}_i(t)$, the constant terms at the right hand side of the governing equation can be eliminated. Expanding (4.5) to m target areas yields the state space model (4.4). □

Some parameters in (4.4) are constants, for example, emissivity for powder $\varepsilon = 0.9$, $\sigma_B = 5.67\times10^{-8}\ \mathrm{W/m^2/K^4}$ and can be determined *a priori*. Other parameters can be identified via system identification. Note that the number of elements in the view factor matrix can be reduced leveraging the symmetry of the system. For example, when there are nine heating zones and nine target areas, we have $F_{11} = F_{99}$, $F_{24} = F_{86}$.

4.3 Multi-zone IR Heating Control Algorithm

As described in Section 2.2.1, the developed testbed is featured with a nine-zone IR heater, where the heating power of each zone can be individually controlled. With a thermal camera measuring the powder bed thermal profile, we formulated a closed-loop control block diagram shown in Fig. 4.2.

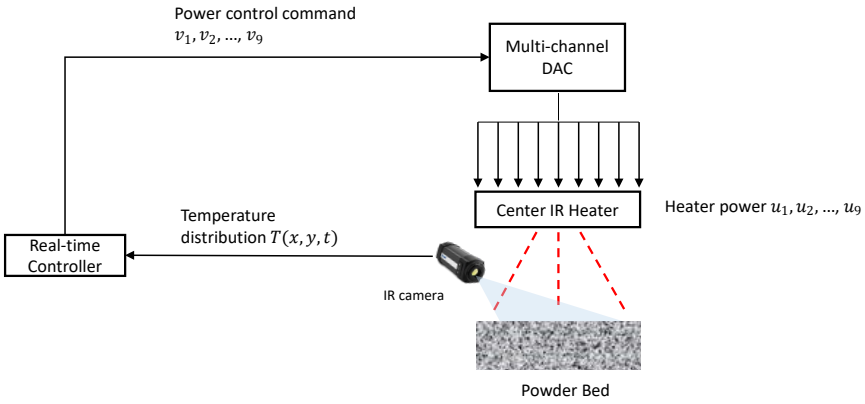

Figure 4.2: Block diagram of the closed-loop infrared heating system.

In the captured image, we sample the temperature at nine locations, as Fig. 4.3(a) shows, corresponding to the nine heating zones of the radiant heater. Note that the camera is employed in an offaixal (Eulerian) frame of reference with an incident angle not equal to 90°. Therefore, the raw image is corrected using coordinate transform to obtain image analogous to which is collected in a coaxial configuration, as shown in Fig. 4.3(b).

Fig. 4.4 shows the proposed multi-zone control structure built on the MIMO mechatronic design. The error signals $e_1(t), e_2(t), \cdots, e_9(t)$, are computed using the temperature measurements $T_1(t), T_2(t), \cdots, T_9(t)$ from the thermal image and the reference temperture $r(t)$. The error signal $e_j(t)$ is used as input to the independent controller (e.g., PID) of heating zone j.

The proposed design decouples the MIMO system into nine individual SISO systems. This is based on the observation of the structure of the view factor matrix in (4.4), which is a square matrix when $i = j = 9$. The view factors on the diagonal line are most significant. The reason is that the

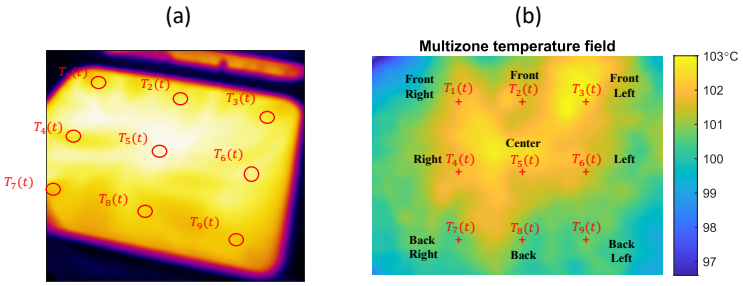

Figure 4.3: Selected sampling locations on the powder bed. (a). Raw thermal image. (b). Coordinate corrected image.

sampling locations in Fig. 4.3 are selected based on the layout of heating zones in Fig. 2.5. From heating zone i to sampling area i, the angle θ equals 0 and the distance s is shortest in (4.3), yielding the largest possible view factor as $\frac{1}{\pi s^2}$. In other words, a large portion of heat emitted from a heating zone is received by the area right below. Therefore, keeping only the diagonal elements of the input matrix, we got the decoupled heating model

$$\frac{\rho d c_p}{k_1}\frac{\mathrm{d}}{\mathrm{d}t}\begin{bmatrix}\tilde{T}_1(t)\\ \tilde{T}_2(t)\\ \vdots\\ \tilde{T}_m(t)\end{bmatrix} = I_{m\times m}\begin{bmatrix}\tilde{T}_1(t)\\ \tilde{T}_2(t)\\ \vdots\\ \tilde{T}_m(t)\end{bmatrix} + \frac{1}{\pi s^2}\begin{bmatrix}1 & 0 & \cdots & 0\\ 0 & 1 & \cdots & 0\\ \vdots & \vdots & \ddots & \vdots\\ 0 & 0 & \cdots & 1\end{bmatrix}\begin{bmatrix}u_1(t)\\ u_2(t)\\ \vdots\\ u_m(t)\end{bmatrix}$$

and developed the multi-zone design.

We also investigated two other control methods for comparison purpose:

1. *Single-loop control/SISO*: The average temperature over a large area is used as the feedback signal, and all heating zones share the same control output from one PID controller. The average temperature is from a pyrometer with a 10° field of view.

2. *Model predictive control*: A popular multivariable control that uses an internal dynamic model of the process and calculates a sequence of future control actions (control horizon) such that a cost function J over the prediction horizon is minimized.

All three control algorithms are compared in Section 4.4 for powder bed preheating with different initial thermal profiles.

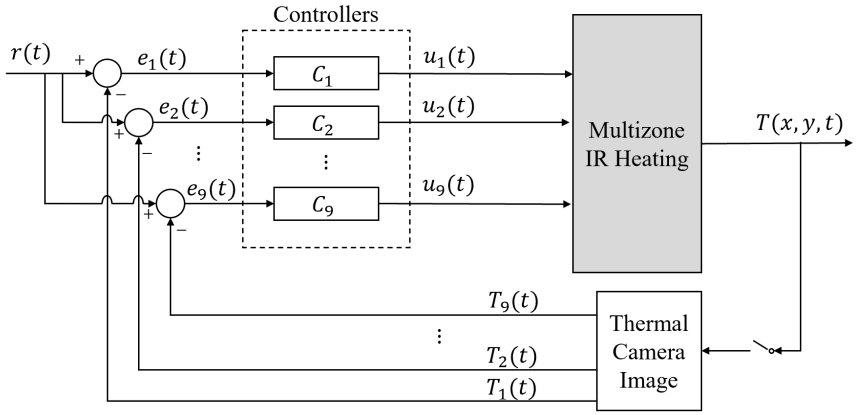

Figure 4.4: Block diagram of proposed multi-zone closed-loop control.

4.4 Experiment Verification

4.4.1 Experiment setup

In the experiment, we preheat the PA12 material. We select the preheating temperature as 150 °C, which is close to the material's melting temperature 176°C and at the same time, provides a safety margin to prevent melting caused by potentially large temperature overshoot. We considered different stages of fabrication and the impact of parts' geometry. Specifically, we performed preheating on three different temperature profiles after a new layer of powder material is spread and before the preheating starts, as demonstrated by Fig. 4.5:

- Fig. 4.5(a) corresponds to the initial layer of the fabrication, where there are no previously fused layers. The powder thickness is large enough so that the melt pool never reaches the underlying solid substrate.

- Fig. 4.5(b) represents the case when the part geometry-induced cross-layer thermal disturbance is around the center zone of the powder bed.

- Fig. 4.5(c) shows the case when the thermal disturbance is around the back and backleft corner.

Note that Fig. 4.5(b) and Fig. 4.5(c) can either be from two different layers/stages of the same part or two parts with different geometries.

The previously processed areas are seen to have higher temperature than the surrounding unprocessed area.

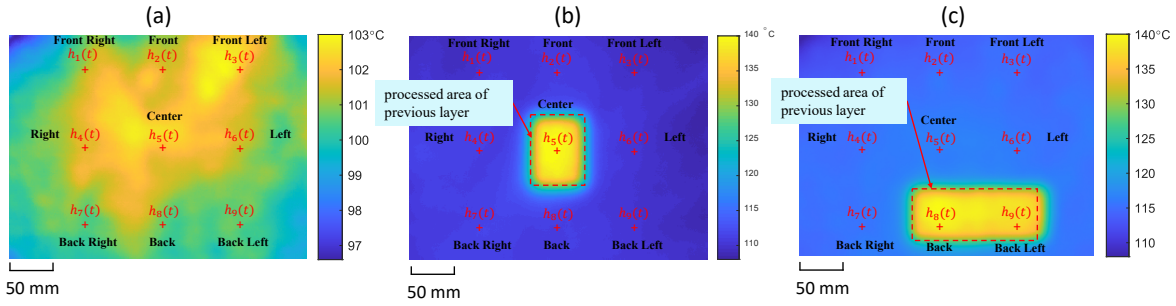

Figure 4.5: Illustration of experimentally tested thermal profiles. (a) Initial layer of the fabrication. (b) Thermal disturbance around the center. (c) Thermal disturbance around the back corner.

Table 4.2 shows the parameters of implemented control algorithms described in Section 4.3. Both single-loop and the proposed multi-zone methods used PID controller. The coefficients were selected using the Ziegler-Nichols tuning. To implement the MPC, we identified the heating process model (4.4). We first heated the powder bed near the operation point of 150°C using single-loop control and then perturbed all the nine heating zones with PRBS (pseudorandom binary sequence) signals. The model was then identified using subspace system identification toolbox in MATLAB.

Table 4.2: PARAMETERS OF THE HEATING CONTROL ALGORITHMS.

Single-loop/Multi-zone PID Control					
Parameter	P_c	P_i	P_d	Control input range	Sampling time
Value	15.22	2e-3	1e-3	0 – 4.5 V	200 ms
Model Predictive Control					
Parameter	Prediction horizon N_P	Control horizon N_C	Output weighting	Output lower limit	Output upper limit
Value	25	15	$I_{9\times9}$	0 °C	160 °C
Parameter	Input rate weighting	Input lower limit	Input upper limit	Sampling time	
Value	$0.1 \times I_{9\times9}$	0 V	4.5 V	1 sec	

4.4.2 Multi-zone heating result for initial layer

When there is no cross-layer thermal disturbance (case in Fig. 4.5(a)), all three control algorithms have similar performance. Fig. 4.6 shows the preheating result using the proposed multi-zone control. The temperature of all nine sampling points increased from 100 °C to the reference temperature 150 °C within sixty seconds. At the steady state, the temperature deviation is constrained within the envelope of $[148.5, 151.5]$ °C. Fig. 4.6(b) shows the powder bed thermal profile at $t = 200$ s. The deviation between the maximum and minimum temperature is 4.5 °C, which is larger due to the vignetting effect of the camera[1]. If evaluating the area in the dashed box in Fig. 4.6(b), the deviation is 3.4 °C, which is close to the deviation of the chosen nine sampling points. This shows that the deviation of the sampling points is a good estimation of the powder bed temperature distribution magnitude.

With proper powder bed temperature control, the melting and solidification rates of the part at different locations are more consistent. Its impact on part quality is illustrated in Fig. 4.7. Without

[1]The temperature measurement is lower around the periphery of the FOV.

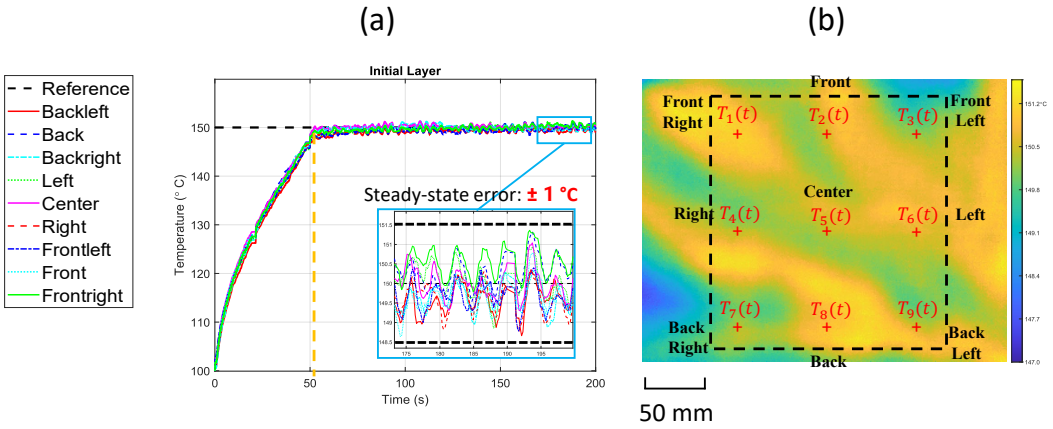

Figure 4.6: Preheating result using multi-zone control for initial layer. (a) Temperature evolution for all sampling locations. (b). Thermal profile of the powder bed at the steady state.

heating control, the large internal residual stress of the part caused severe wrapping (Fig. 4.7(a)). On the contrary, with proper preheating, the printed part in Fig. 4.7(b) is flat with a smooth surface finish.

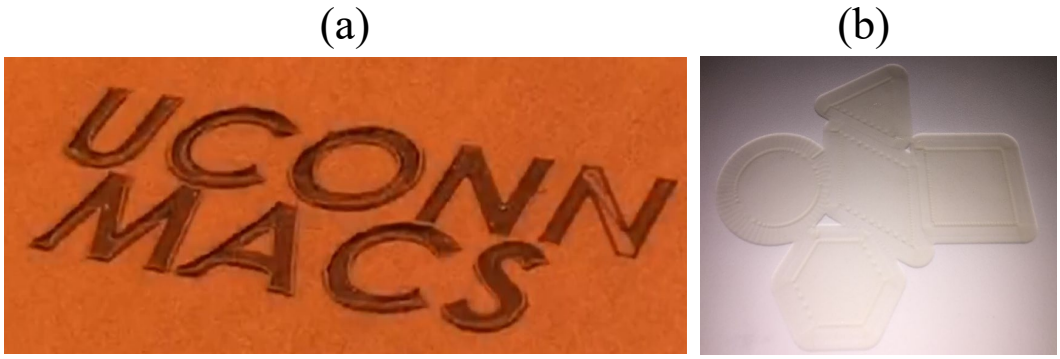

Figure 4.7: Impact of powder bed temperature control on part quality. (a) Part warping w/o proper control. (b) Finished part with proper heating.

4.4.3 Preheating control algorithms comparison

Fig. 4.8 shows the preheating results using the three control schemes described in Section 4.4.1 when the cross-layer thermal disturbance from previously processed area is located around the center (Fig. 4.5(b)).

Before the center zone temperature reached the target level:

- Both single-loop and multi-zone methods operated all heating zones with the full power of 4.5 V.
- MPC operated center zone with full power but limited some control efforts of non-center zones.

After center zone temperature reached the target level:

- The proposed multi-zone control was able to effectively turn off the unnecessary center heating (illustrated by the blue arrow in Fig. 4.8).
- MPC reduced the power of the center zone gradually and turned it off completely when all sampling locations reached the reference temperature.
- Single-loop control continued to operate the center zone at full scale until all sampling locations reached the reference temperature.

As a result, the single-loop control, the multi-zone control, and MPC have heating speeds in descending order. The zoomed-in plot in Fig. 4.8 shows the peak temperature errors at the center zone. Both the multi-zone control and MPC mitigated the unnecessary heating power of the center zone and have comparable peak errors. On the contrary, the single-loop control generated a much larger overshoot, which can potentially cause the powder to melt before laser exposure, in which case the fabrication has to be aborted.

At the steady state, we can see that the proposed multi-zone control has similar or even superior accuracy as well as variance compared with the optimization-based MPC. This is verified by

calculating the mean absolute error for each zone and the average standard deviation for all heating zones between 125 s and 150 s. The results are listed in Table 4.3. We also see that the steady-state performance of single-loop control is significantly inferior. This is because the control action is not discretized at each moment. In the scope of a narrow time window (around 2 s), each zone experiences temporary overheating or cooling.

Table 4.3: AVERAGE ABSOLUTE ERROR AND STANDARD DEVIATION IN STEADY STATE

Sampling Location	**MPC**	**Multi-zone**	**Single-loop**
Average Absolute Error (°C)			
Back left	0.61	0.34	1.21
Back	0.38	0.23	0.65
Back right	0.88	1.13	0.86
Left	1.03	0.42	2.12
Center	8.11	7.67	7.71
Right	0.36	0.27	0.68
Front Left	1.07	0.28	1.27
Front	0.39	0.56	0.65
Front Right	0.47	0.27	0.76
Average Standard Deviation (°C)			
	0.39	0.30	0.76

4.4.4 Adaptive add-on tuning for multi-zone control

When there are previously fused layers, as in the cases of Fig. 4.5(b) and 4.5(c), we propose an adaptive parameter tuning scheme building on the multi-zone control. Specifically, the geometry of previous layers can be obtained from the CAD model. Therefore, the location of the high-temperature area is available to the controller before the heating starts for each layer. We can then limit the control power for the heating zones that are most close to this area. In Fig. 4.5(a), this corresponds to the center zone, and in Fig. 4.5(b), this corresponds to the backleft and back zones. Moreover, when the temperature of these heating zones reaches the reference temperature, we further limit the control power of other heating zones to mitigate the impact of the latent heat. As a result, in Fig. 4.9(a), we see that with the proposed tuning, the peak temperature error of the center zone was reduced from 12 °C to 10 °C; similarly, we observe a reduction from 12 °C to 9 °C in the other case from Fig. 4.9(b). However, the heating time was increased as a trade-off. Regarding the steady-state error, the multi-zone control achieves comparable results for all the different configurations.

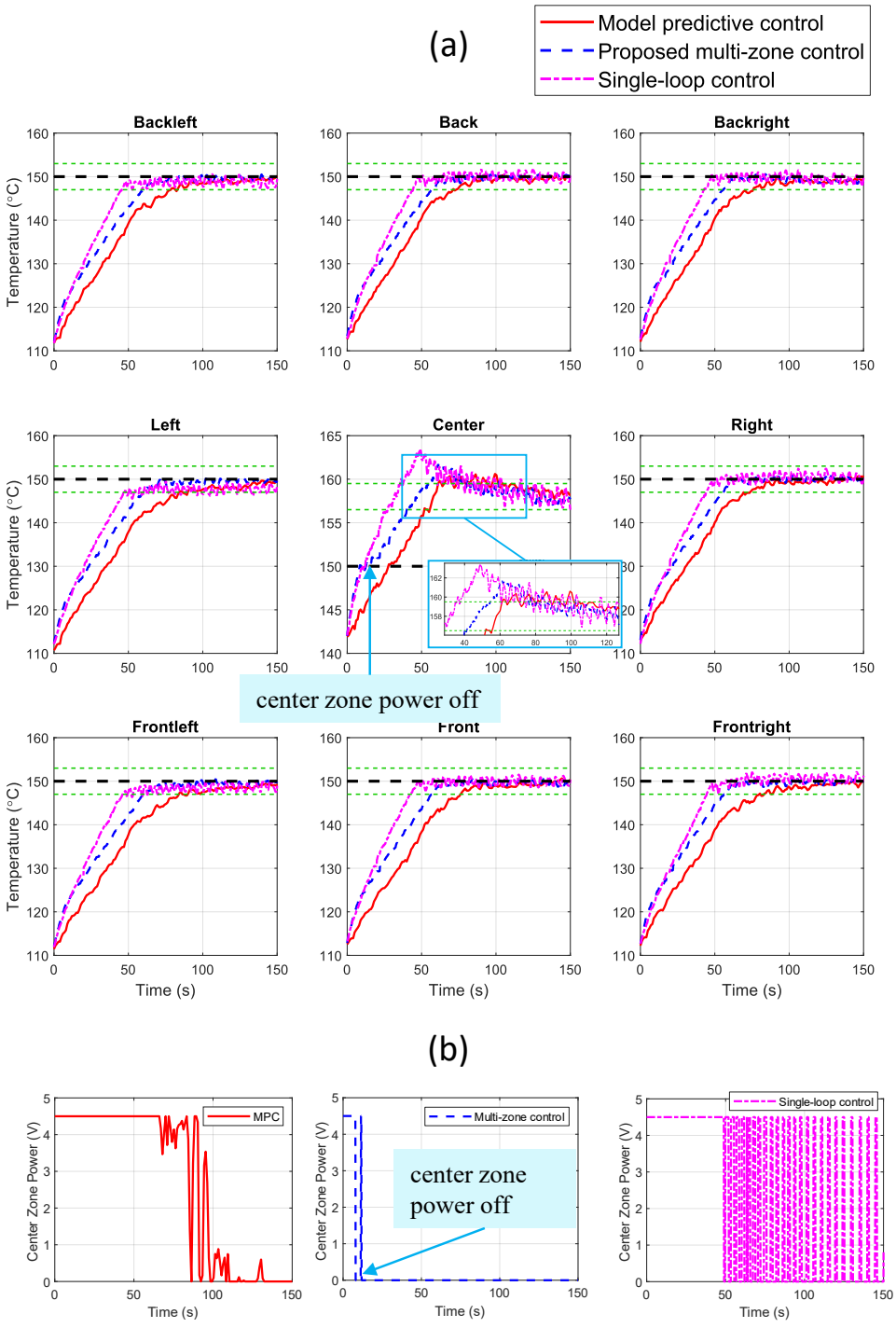

Figure 4.8: Comparison of heating control algorithms. (a). Temperature evolution of the sampling locations on the powder bed. (b). Center zone heating power.

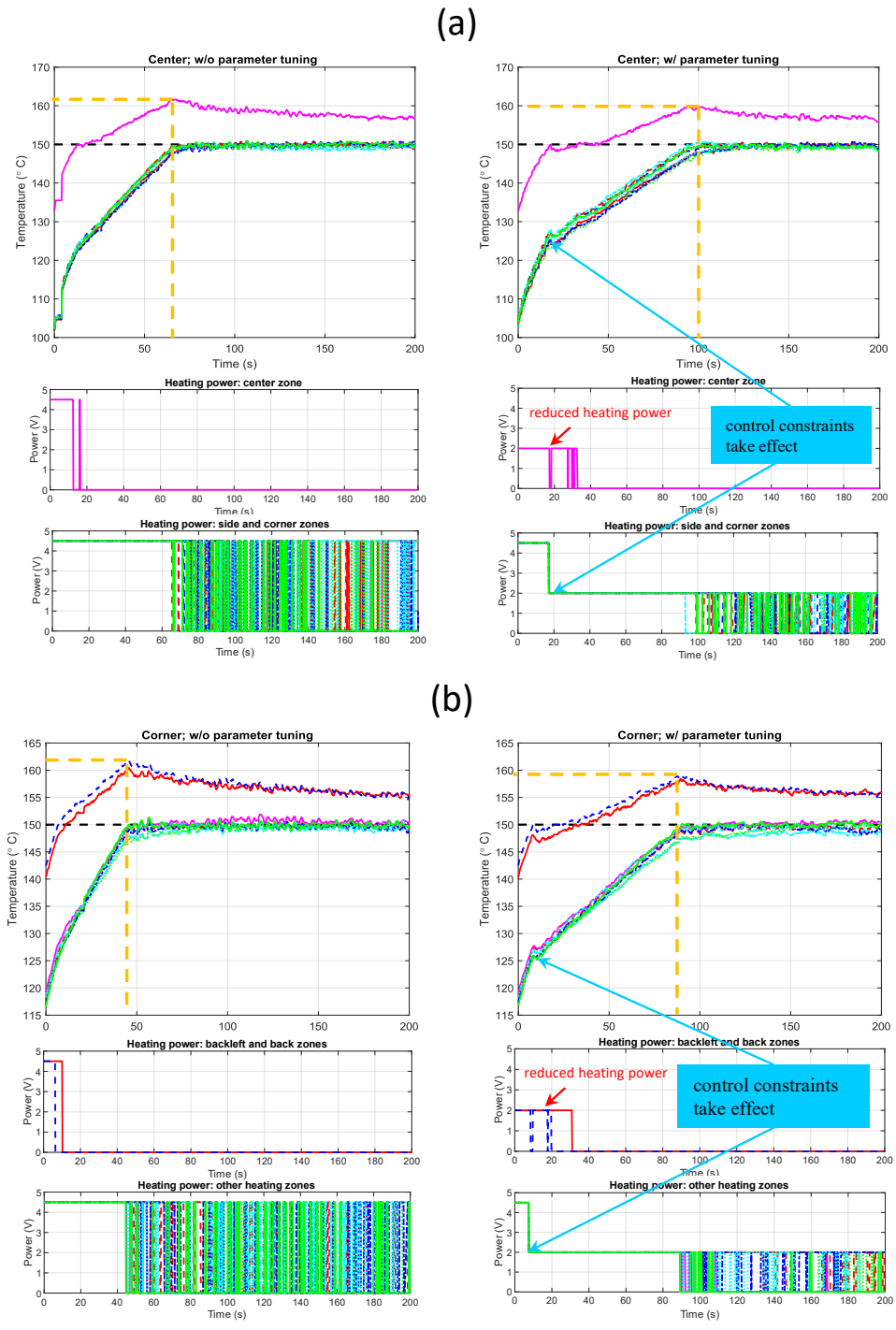

Figure 4.9: Multi-zone control with add-on tuning. (a). Cross-layer thermal disturbance around the center. (b). Cross-layer thermal disturbance around the back corner.

Chapter 5

IMAGE ANALYTICS FRAMEWORK FOR DEFECT DETECTION AND FUSION PROCESS CONTROL

5.1 Introduction

The consensus in the LPBF literature is that the process can benefit from process monitoring and feedback control. There is an imperative need to develop a robust process monitoring and control framework (1) to monitor system health and flag potential issues to abort builds or make corrections, (2) to detect and predict defects to guide or replace ex-situ/post-process inspection, and (3) to ultimately enable adaptive model-based closed-loop control of process parameters to reduce part-to-part variation and assure quality.

The architecture of LPBF feedback control is straightforward. Taking image-based coaxial monitoring as an example (Fig. 5.1), the multi-physical laser-material interaction is monitored by the camera with a high sampling rate. The captured image is then processed to extract process signature $m(t)$, which reflects key process information of part quality, defect formation. Its difference with the reference $r(t)$ (e.g., melting pool dimension) forms the error signal $e(t)$ that can be used by a feedback controller (e.g., PID) to tune process parameters (e.g., laser power, scan velocity).

However, only a handful of control efforts for LPBF have been experimentally demonstrated [75], major reasons being: (1) the architecture of the commercial LPBF machines remains closed and prohibitively difficult to test systematically and (2) correlations between process measurements, process parameter settings, and quality metrics are not well understood.

The first challenge is addressed by the control-oriented process monitoring mechatronic design described in Section 2.2.2. Fig. 5.2 shows the developed hardware implementation of the control scheme in Fig. 5.1.

This chapter describes the contribution of this thesis to the second challenge. We focus on

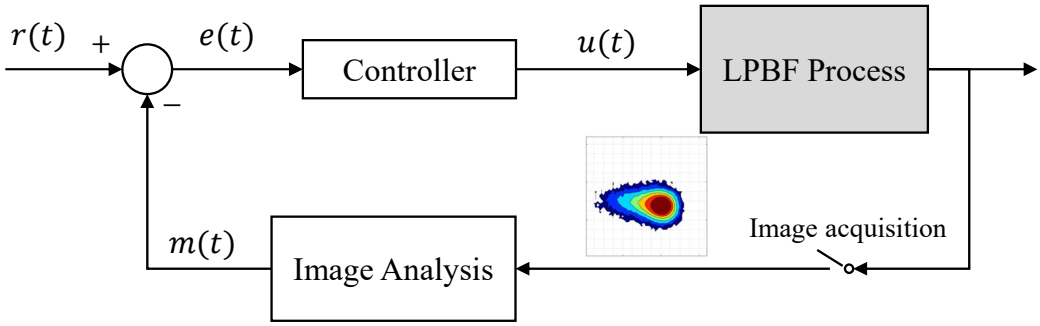

Figure 5.1: Schematic diagram of image-based LPBF feedback control.

developing an efficient image processing infrastructure for extracting significant information that reflects the multi-physics evolution of the melting pool, laser-material interaction characteristics, and potential process imperfections. This is especially non-trivial for the polymer LPBF and light-colored melt pools due to the challenging surface features. In metal AM, it is unchallenging to distinguish the laser-processed zone from surrounding materials in the collected data, either captured by a visual camera or a thermal camera. Due to the significant temperature differences between the melt pool and the unprocessed powder, a simple pixel-level thresholding algorithm works well [76]. Such a distinction is not available in polymer LPBF and similar low-contrast AM except for using middle-wave or long-wave thermal cameras. However, there are several limitations of using an IR camera for real-time control of LPBF:

1. The frame rate of the infrared camera is not comparative with the visual camera due to the high computation cost.

2. The CO_2 laser wavelength is within the operating wavelength range of the thermal camera, which creates difficulty for the coaxial optical path design. There is no coating available that allows the dichroic optic to work as a bandpass/bandstop filter for CO_2 laser.

3. The cost of a thermal camera is significantly higher than a visual camera with the same sampling rate and resolution. A high-end thermal camera can be prohibitively expensive and

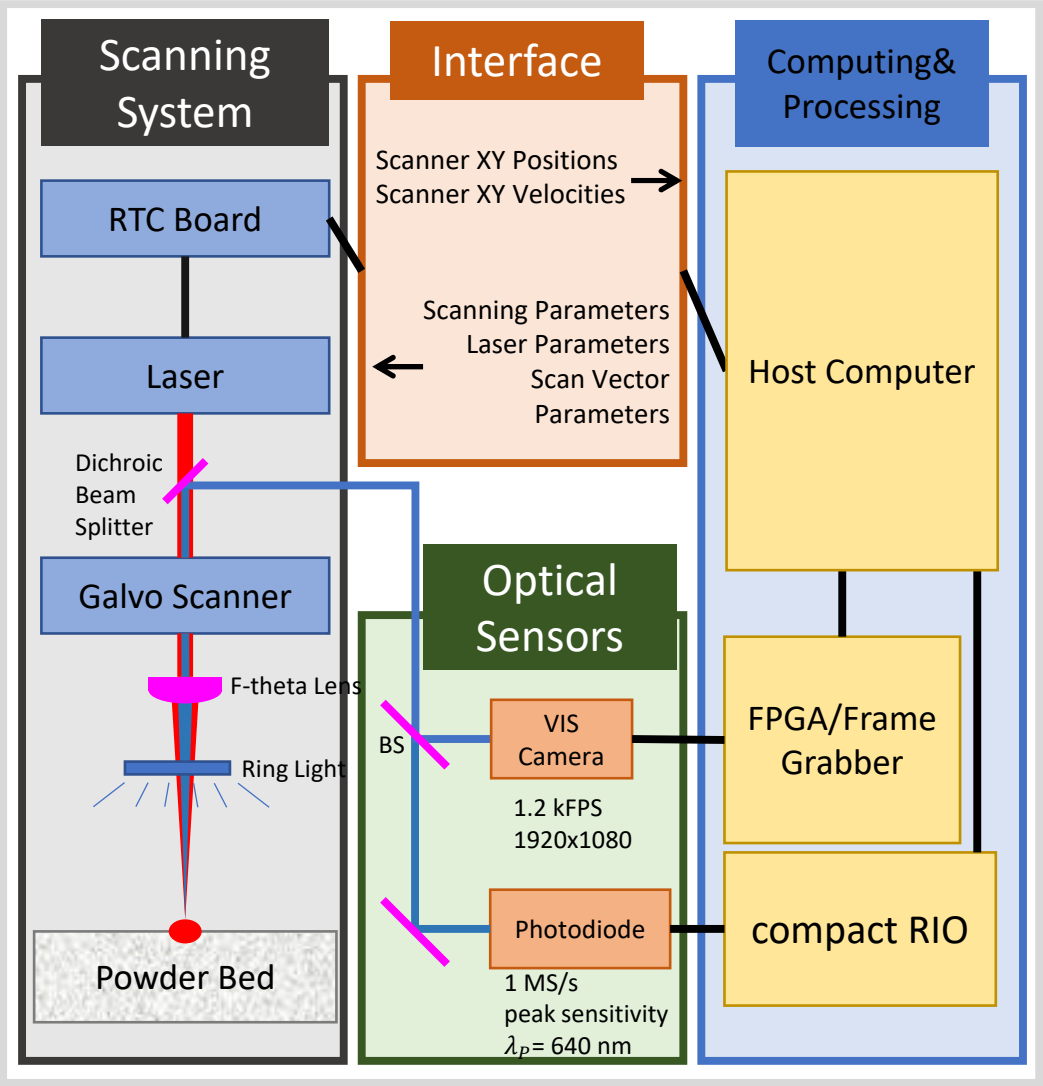

Figure 5.2: Scheme of the image-based LBPF control implementation in the developed platform: BS = beam splitter, DBS = dichroic beam splitter, VIS = visible, MS/s = million sample per second.

is not practical to be broadly used in the industrial production environment for AM.

In the in-situ monitoring literature, minimal studies report the techniques on process zone identification, signature extraction, and defect detection using visual cameras. Even fewer focus on problems involving light contrasted edges and smaller temperature differences over the surface

layer. This is the motivation as well as one of the main contributions of this work.

Targeting first at addressing issues of raw images such as dust noise particles, uneven illumination, and low powder-part contrast, we propose to utilize a combination of pre-processing algorithms, including morphological operation, imaging field correction, and adaptive histogram equalization methods. Using a graph-based segmentation, our approach isolates the area that interacts with the power source from the unprocessed powder bed. Along with the segmentation results, we further provide geometrical dimensions and justification for defect formation. With the quantitative dimension signature, we further

- propose two novel features that can be extracted from the image processing result and correlate them to the printed part quality and process parameters.

- reduce the noise level of the measured signal with Kalman filter.

In conclusion, with our tailored analysis platform and in-house developed database, we developed the full framework to realize the feedback path in Fig. 5.1.

The remainder of this chapter is organized as below. Section 5.2 presents the image analytic framework. Section 5.3 proposes data interpretation methods building upon the results from Section 5.2.

5.2 Image Analytics Framework

5.2.1 Image data acquisition setup

As shown in Fig. 5.3(a), in the experiment, we monitored the melting pool area when processing a single-layer geometry that is composed of a square (29 mm × 29 mm) and a triangle using PA12 powder material. The fusion performed on a thick powder bed so that the melt pool never reached the underlying solid substrate. This is to investigate the melt pool behavior during the fusion of an unsupported overhang, where anomalies and defects can be triggered by the differing thermal conditions present due to the low thermal conductivity of the unfused powder. Before printing, the powder bed was preheated to 150 °C. To ensure adequate light exposure, we used a relatively low

camera frame rate of 50 fps. The scanning speed was set as 6 mm/s, and the laser power varied from 0.4 to 1.0 W, leading to a linear energy density from 0.067 to 0.167 W·s/mm. Over the course of a single print, approximately 1500 frames of data were collected.

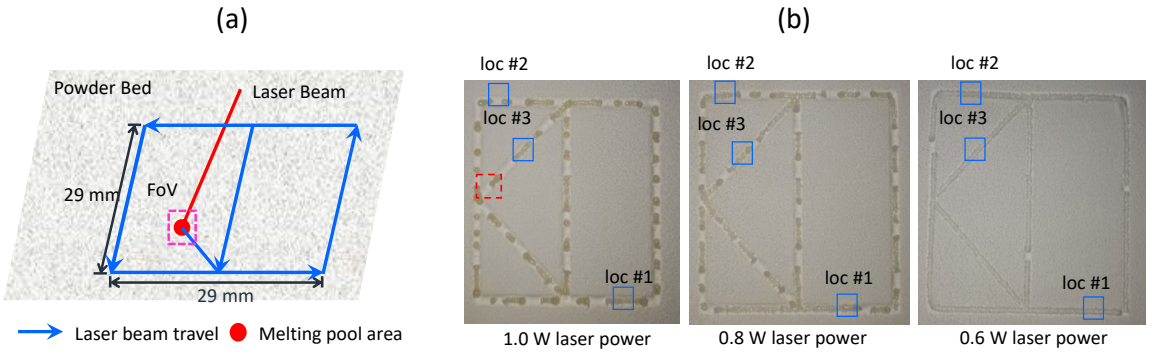

Figure 5.3: Experiment setup and result. (a) Schematic diagram of the fusion geometry. (b) Solidified parts with different laser power parameters.

An example of the captured images when printing with light-color material is shown in Fig. 5.4. Several salient challenges may be seen in this raw image:

1. Noise due to dust on optics and sensors, characterized by small–yet dark–particles.

2. Uneven background intensity, as the right part of the image is brighter than the left because of uneven illumination.

3. Low contrast between the processed zone and surrounding raw powder.

5.2.2 Image pre-processing

We propose to utilize a combination of pre-processing algorithms to address the issues discussed in the previous section. Specifically, we use morphological image processing to remove the dust particle noises, use flat-field correction (FFC) to compensate for the inconsistent illumination,

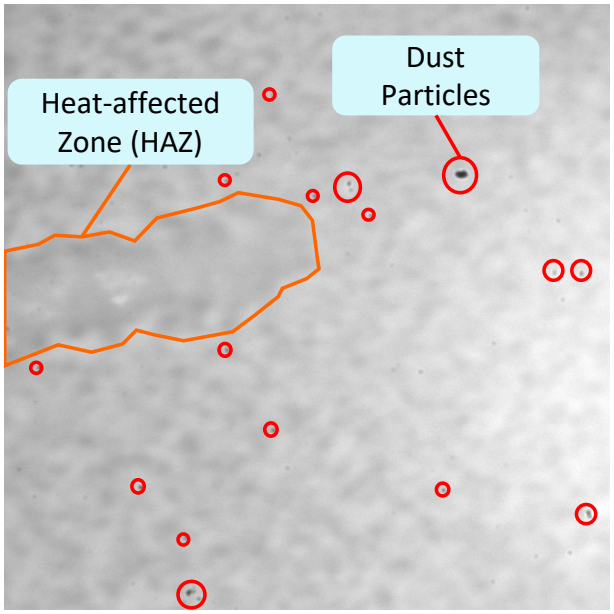

Figure 5.4: A sample coaxially captured image for light-color PA12 material.

and improve the contrast between the processed zone and the surrounding unmolten powder with contrast limited adaptive histogram equalization (CLAHE).

Morphological image processing

Morphological image processing is a collection of non-linear operations related to the shape or morphology of features in an image. Most morphological operations involve a combination of set operations based on structuring elements (SE)–shapes used to probe an image understudy for properties of interest. The specific algorithm we propose to remove the dust particle noise is grayscale closing–a combination of grayscale dilation and erosion:

$$f \cdot b = (f \oplus b) \ominus b$$

where f is the image under study, b is a structuring element, and $\oplus/\ominus$ denote, respectively, grayscale dilation and erosion.

Geometrically, the closing of image f by a flat structuring element b can be interpreted as

pushing a flat disk down from the top against the upper surface of the intensity profile while being translated to all locations. The result is constructed by finding the lowest points reached by any part of the SE. As a result, the bright details and background in f are relatively unaffected, but the dark features are attenuated, with the degree of attenuation depending on the relative sizes of the features compared with the SE.

Fig. 5.5 shows the result of applying grayscale closing on the raw image with a disk SE that has a diameter of 17 pixels. Size 17 is a balanced choice for the captured image database. To remove most of the particle noises, the mask has to be large enough. On the other hand, the bright details and edge definitions will be lost if the mask gets too large. This value may be different for the imaging data from other systems and has to be tuned before applying the proposed morphological operation. Most of the noise dust particles in Fig. 5.4 are attenuated except for one that is bigger than the SE. At the same time, the profile and texture of the laser-processed zone remain relatively intact.

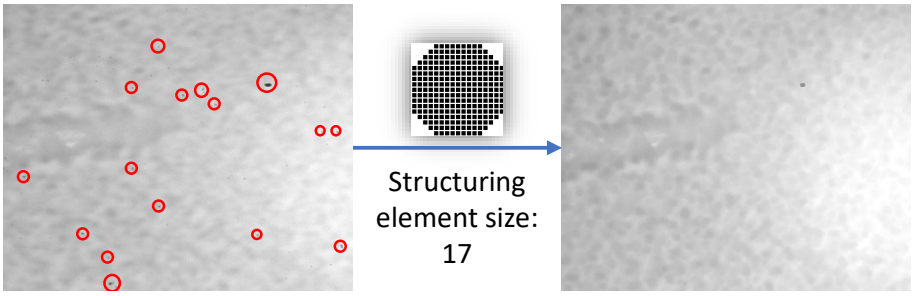

Figure 5.5: Illustration of removing particle noises with grayscale closing.

Flat field correction

FFC is used to compensate for the inconsistent illumination in the raw image. The algorithm starts with estimating a flat field image, which represents the background intensity. This is realized by surface fitting a two-dimensional polynomial model on the image intensity. With the estimated flat field image, each pixel of the original image is adjusted. As a result, the background intensity of the

corrected image distributes evenly across the whole image (Fig. 5.6).

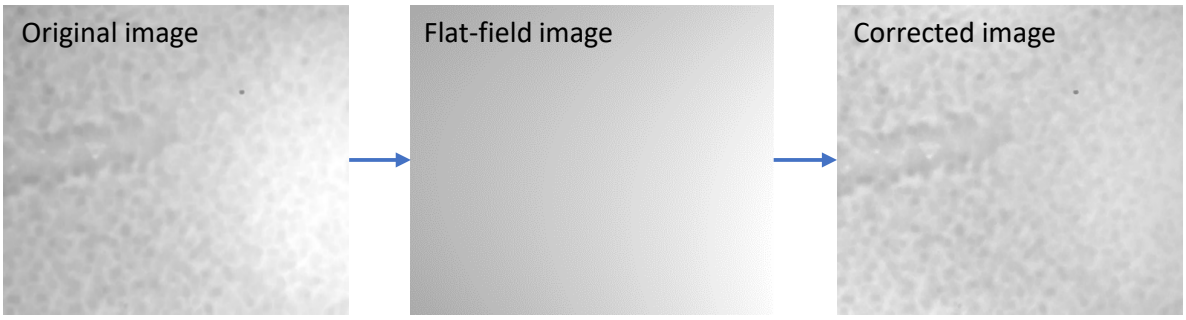

Figure 5.6: Illustration of correcting background intensity with FFC.

Contrast limited adaptive histogram equalization

We propose to use CLAHE to improve contrast in the image. The term "adaptative" indicates that the histogram equalization is implemented locally. It is therefore suitable for enhancing the definitions of edges in the local regions of an image. As shown in Fig. 5.7, the contrast between the laser-processed zone and surrounding powder zone is improved for both dark- and light-color materials using CLAHE.

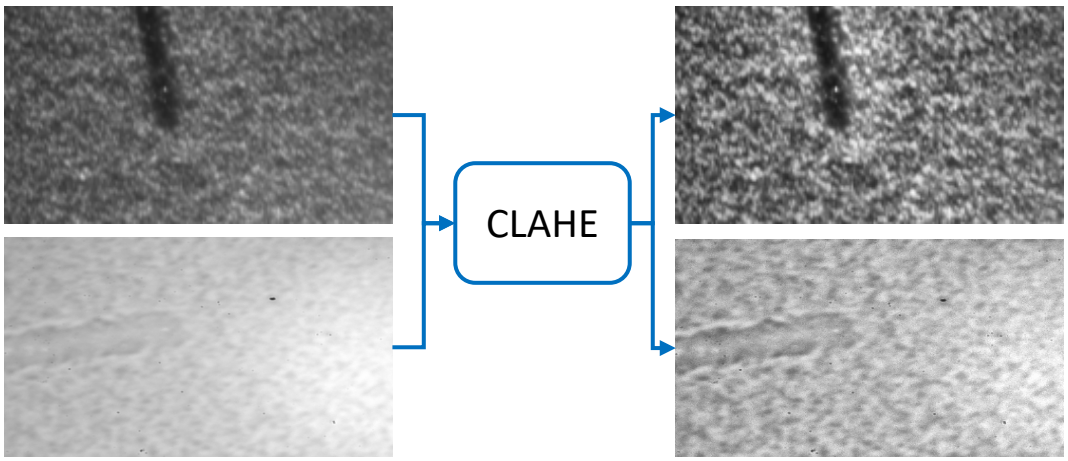

Figure 5.7: Illustration of improving contrast with CLAHE.

5.2.3 Laser-processed zone identification

Thresholding algorithm limitation

For dark-color material, the grayscale value between the powder and the processed zone is relatively large. We can isolate the laser-processed zone by:

1. Converting the grayscale image into a binary image by global thresholding

2. Removing the small objects using morphological processing (binary opening) as shown in Fig. 5.8(a)-(c).

However, the same procedure will not work for light-color material, as can be seen in Fig. 5.8(d)-(f). On the one hand, in this scenario, the grayscale intensity of the processed zone varies in a broad range, and thresholding cannot extract it as a complete part with a dominating size. On the other hand, because the powder region is not smooth (particle size varies in the range of 50 to 100 μm), polymer particles appear as large, connected components in the binary images. Moreover, areas with low illumination intensity (corners in Fig. 5.8(e) and 5.8(f)) have similar gray level values with the processed zone. As a result, it is not possible to distinguish the processed zone from the binarized image based on area size/shape. This applies to both global and local thresholding. Therefore, for light-color materials, we need an algorithm that can identify the intrinsic characteristics of the processed zone.

Processed zone identification

The technique we propose to identify the processed zone is efficient graph-based image segmentation [77]. To perform the segmentation, the original image is first transformed into a graph $G = (V, E)$, where each node $v_i \in V$ corresponds to a pixel in the image, and the edges $(v_i, v_j) \in E$ connect certain pairs of neighboring pixels. A weight $w((v_i, v_j))$ is associated with each edge, which is defined as the absolute grayscale difference between elements v_i and v_j. The corresponding diagram is shown in Fig. 5.9. Using this representation, the algorithm then defines a predicate for measuring

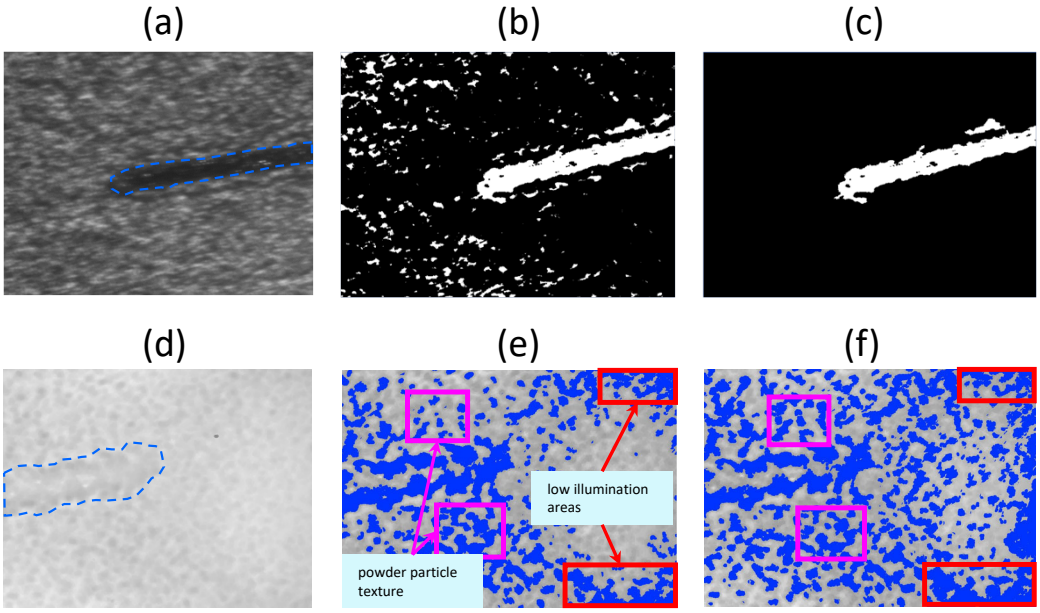

Figure 5.8: Processed zone identification with simple thresholding algorithm. (a) Dark-color material image. (b) Global-thresholding. (c) Morphological opening. (d) Light-color material image. (e) Global-thresholding. (f) Local thresholding.

the evidence for a boundary between two regions. Based on this predicate, the segmentation can be created by pairwise region comparison. The method has a complexity of $O(n \log n)$ for n image pixels and generally runs in a fraction of a second on an average desktop computer for a 320×240 image. Leveraging the parallel computation advantage of the FPGA, this can be reduced to milliseconds.

Fig. 5.10 illustrates the procedure of processed zone identification with graph-based segmentation. The raw image is first pre-processed (Fig. 5.10(b)) with the algorithms discussed in the previous section to attenuate noises and enhance contrast. In the segmentation output (Fig. 5.10(c)), we see that the boundaries of the processed zone are accurately identified along the scanning direction. The front edge of the melting pool is not found here because the melting pool area had not solidified yet when the frame was grabbed, and the grayscale intensity difference with surrounding powder is

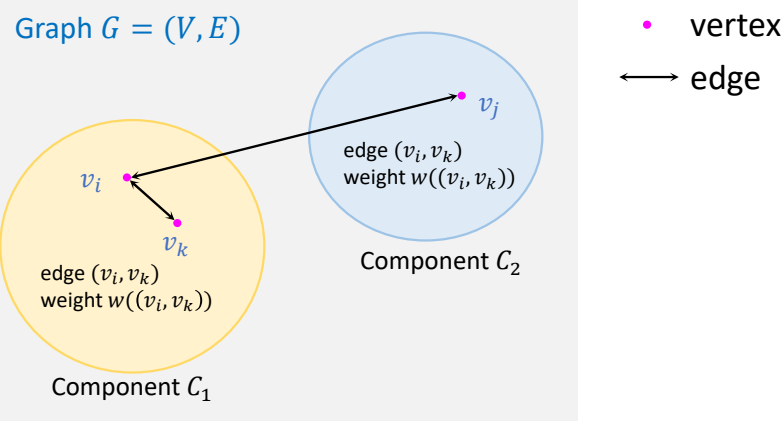

Figure 5.9: Graph-based segmentation diagram.

minimal (it is difficult to identify this edge even with human perception). However, thanks to the coaxial optical design, the melting pool center location remains unchanged for each frame and is available *a priori*. With a predicted melting pool diameter (from, e.g., the processed zone width in the previous frame), we can estimate the front edge and use it to split the component that coincides with the current scanning vector. As a result, we accurately extracted the processed zone (Fig. 5.10(d)) from the original noisy and low-contrast raw image.

5.3 Defect Detection, Quality Evaluation, and Process Signature Filtering

With the proposed image processing framework, we can collect defect formation dynamics related to material melting and solidification, and extract important process signatures as metrics correlated to process parameters and final part quality.

Detection of overheating defect

The solidified geometries with different laser power settings are shown in Fig. 5.3(b). We observe that when the energy density is excessively high, as in the case with a laser power of 1.0 W, the processed material consolidates so fast that the balling effect is very significant and the fused tracks

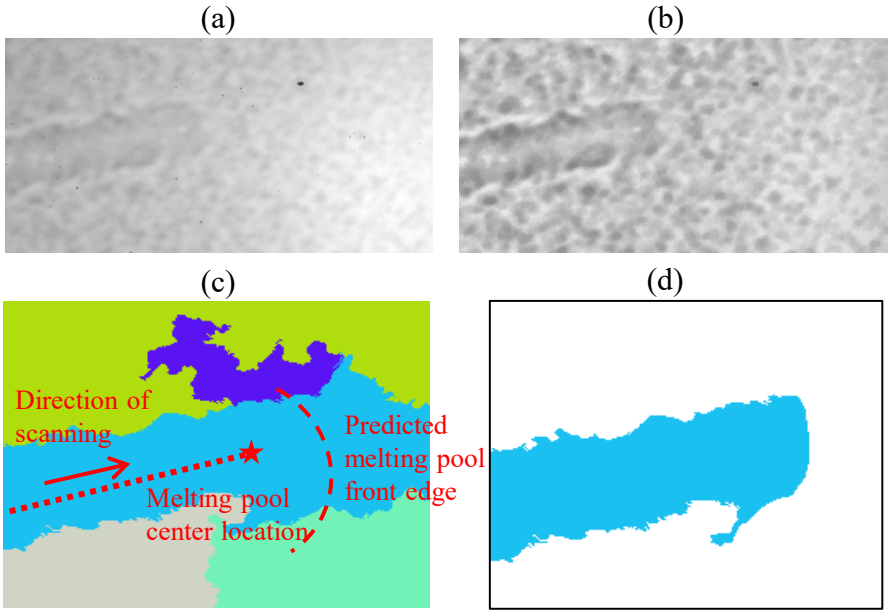

Figure 5.10: Proposed zone identification with graph-based segmentation. (a) Raw image. (b) Pre-processed image. (c) Segmentation result. (d) Identified processed zone.

break into short segments. When reducing the power to 0.8 W, the overheating is improved with mitigated balling and discontinuities. However, the contour of the tracks is still irregular. In the case of 0.6 W laser power, the balling effect disappears, and the breaks only happen occasionally. Besides, the track contour is smooth and straight with a consistent width of the processed zone. When the power is 0.5 W or less, the powder material did not melt due to lack of energy density.

These post-process observations are correlated to the signatures in the processed image data. The break defect can be easily detected with the segmentation result. As an example, the image in Fig. 5.11 corresponds to the location denoted by the dash red box in Fig. 5.3(b). A line from the center of the melting pool to the edge of the image along the travel direction[1] intersects with three different components. This indicates that the processed zone is divided into parts, and therefore, evinces a break in the processed zone.

[1]Recall Fig. 5.2, this is the information transferred from host PC to RTC5 and is available *a priori*.

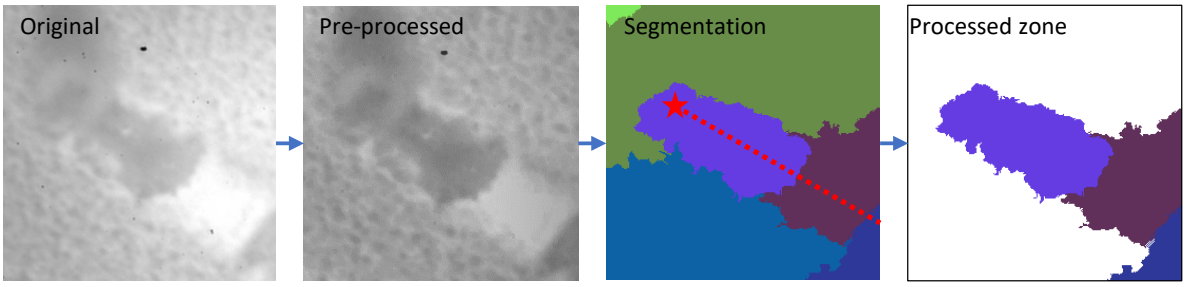

Figure 5.11: Break defect identification using segmentation result.

Part quality evaluation

We next propose features that can be correlated with part morphology and process parameters. We select three sample locations, Loc #1, Loc #2, and Loc #3 on the fused part for all three power levels, as denoted by the solid blue boxes in Fig. 5.3(b). For each location, the raw image, the pre-processed image, the extracted processed zone, and the estimated width distribution along the traveling direction (from image boundary to melting pool) are shown in Fig. 5.11. At first glance, as the power increases, the contour of the processed zone becomes more irregular, with a larger variation of the component width along the travel direction. This is verified by calculating two quantitative process signatures. The first one is the ratio between the component perimeter and the length of the scanning vector, as plotted in Fig. 5.12(a). We see that this ratio increases for all three sampling locations as the laser power increases. A similar relationship is observed in the plot of the component width variance (Fig. 5.12(b)). Therefore, these two features can be used to evaluate the possibility of overheating, which is a major defect source when printing structures with overhang surfaces. Note that at Loc #2 and Loc #3 of the 1.0 W print, the solidified track breaks. This is not directly detected by counting the segmentation components as the processed zone remains as a single part at the moment of capturing the frame. However, both the proposed features, especially the covariance, are significantly high here. This suggests that we may use them to predict break defects by setting proper thresholds.

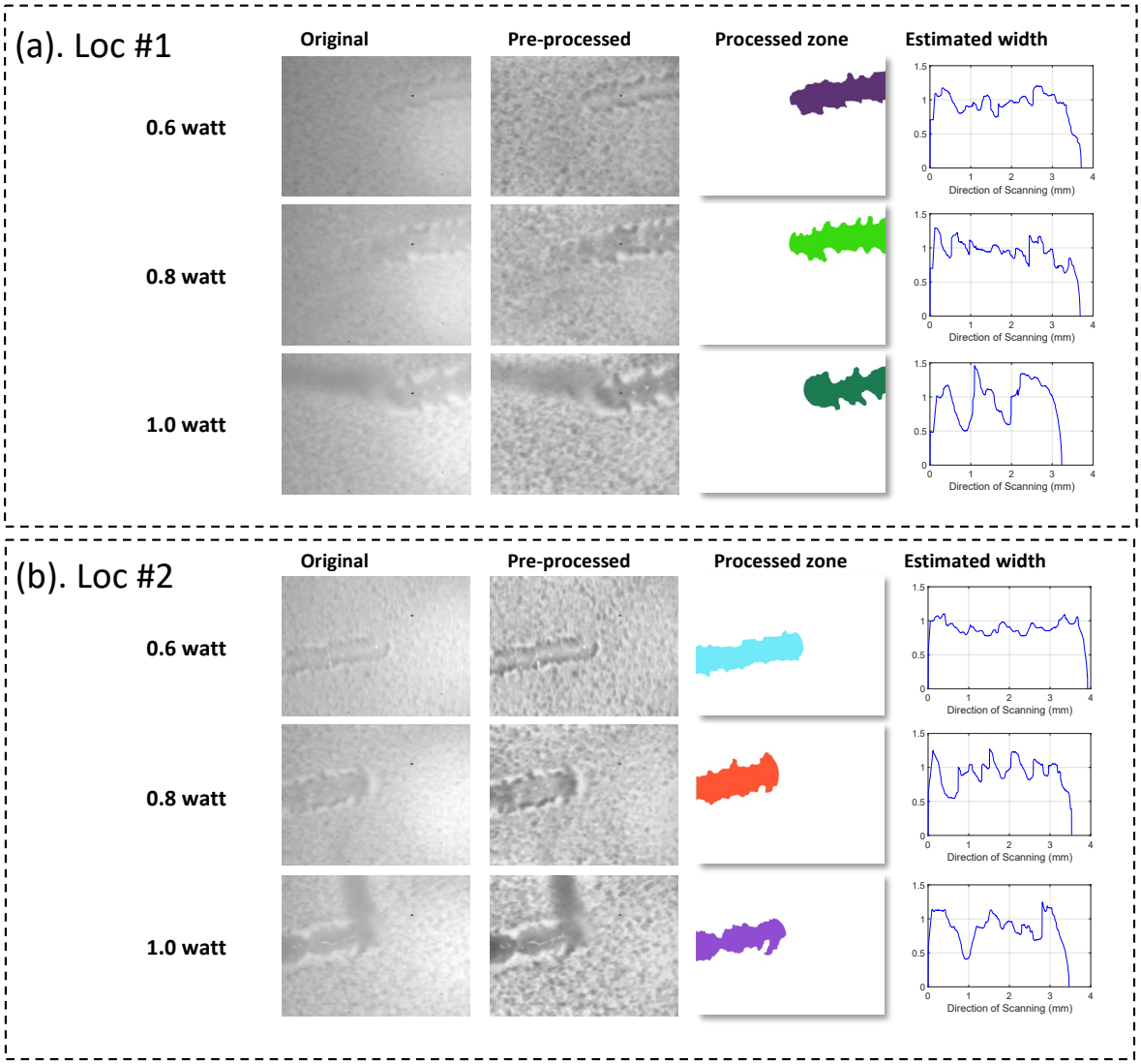

Melting pool width signal filtering

From Fig. 5.11, it can be seen that even with proper process parameters, the raw melting pool width signal from the image segmentation result is still noisy and can not be directly used in closed-loop control. This is an intrinsic result of the laser-material interaction process. Specifically, because the powder is not 100% packed, during sintering, if a particle is closed enough to the laser spot boundary, it will be melted and included in the processed zone. On the other hand, if a particle is far enough from the laser spot, it will not be attached to the processed zone, as Fig. 5.13(b) shows. As

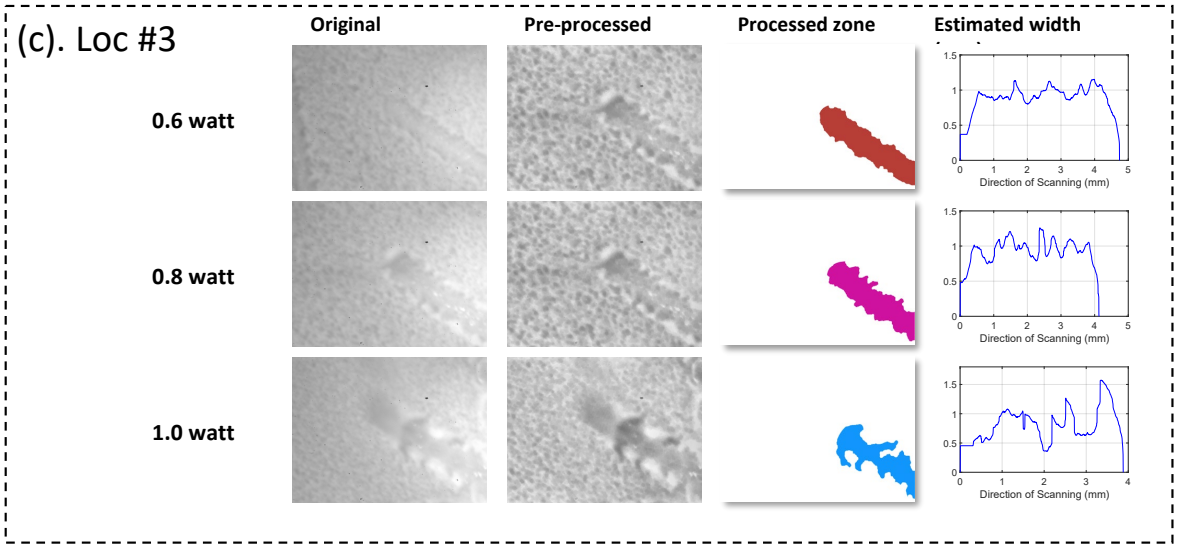

Figure 5.11: Processed zone identification results for different power levels. (a). Loc #1, close the start of the printing. (b). Loc #2, intermediate location. (c). Loc #3, close to the end of the printing.

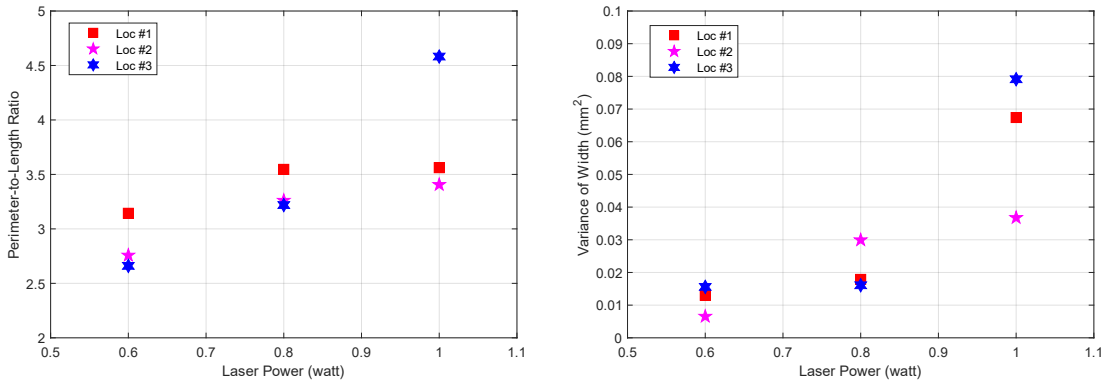

Figure 5.12: Extracted process signatures from the segmentation results. (a). Ratio between component perimeter and length. (b). Variance of component width.

a result, the boundary of the processed zone shows a variation with magnitude around 100 μm (Fig. 5.13(a)), which is closed to the maximum diameter of the PA12 polymer particle.

Therefore, the melting pool width signal has to filtered to reduce the noise level before injecting

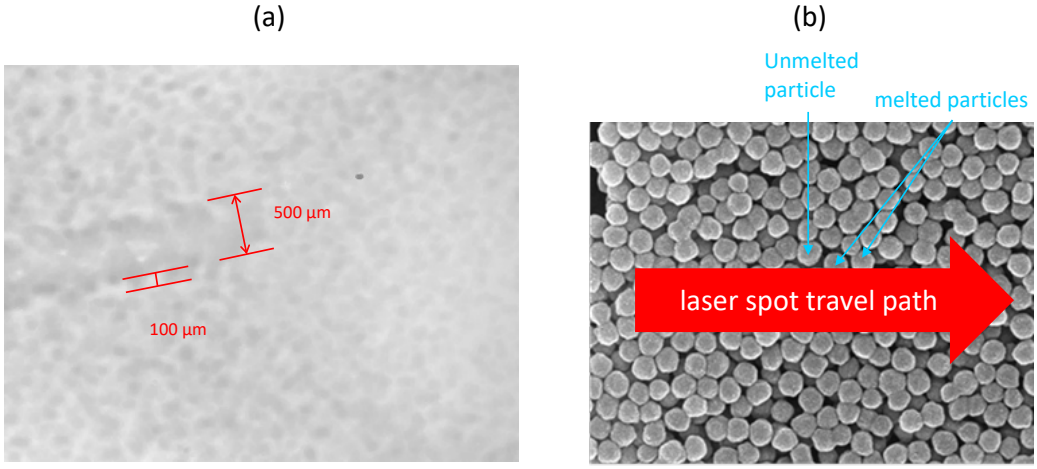

Figure 5.13: Melting pool width noise source analysis. (a) Dimension annotation on captured image. (b) Laser and powder interaction around the boundary.

back to the closed loop in Fig. 5.1.

As the majority of pixel- and imaging-related noises are inherently Gaussian [78], we apply a Kalman filter to filter the measurement signal.

In LPBF, the boundaries of the surface layer are approximately adiabatic (zero temperature gradient). Both the temperature and the geometry of the melt pool have empirical first-order dynamics [4]. Therefore, we propose the transfer function of melting pool width as

$$W(s) = \frac{k_{dc}}{1+\tau s} E(s)$$

where W is the melting pool width (m), E is the deposited energy density (watt·s/m), defined as the ratio between the laser power and the scan velocity, k_{dc} is the system gain, and τ is the time constant (s).

After transforming, the continuous time state space model of the Kalman filter is

$$\begin{aligned} \dot{w(t)} &= -\tfrac{1}{\tau} w(t) + \tfrac{k_{dc}}{\tau} e(t) + \omega(t) \\ y(t) &= w(t) + \gamma(t) \end{aligned},$$

where $\omega(t)$ is the process noise, which is a white noise signal with zero mean and covariance Q, and

$\gamma(t)$ represents the measurement noise with covariance R. Kalman filter with large process noise Q generates larger error at steady state and faster disturbance compensation speed.

Before the implementation of the Kalman filter, we need to obtain several parameters of the process model. The system gain k_{dc} can be decided by calculating the ratio between the steady-state melting pool width and the energy density. We obtained the time constant τ from the experimental data. Fig. 5.14 shows all image frames from the start of the print to the moment when the melting pool width is stable, with a downsampled frame rate of 70 fps. In frame #6, the melting pool size evolves to a dimension that is close to 63.2% of the steady-state value. Therefore, the time constant τ is about $5/70 = 71.4$ ms.

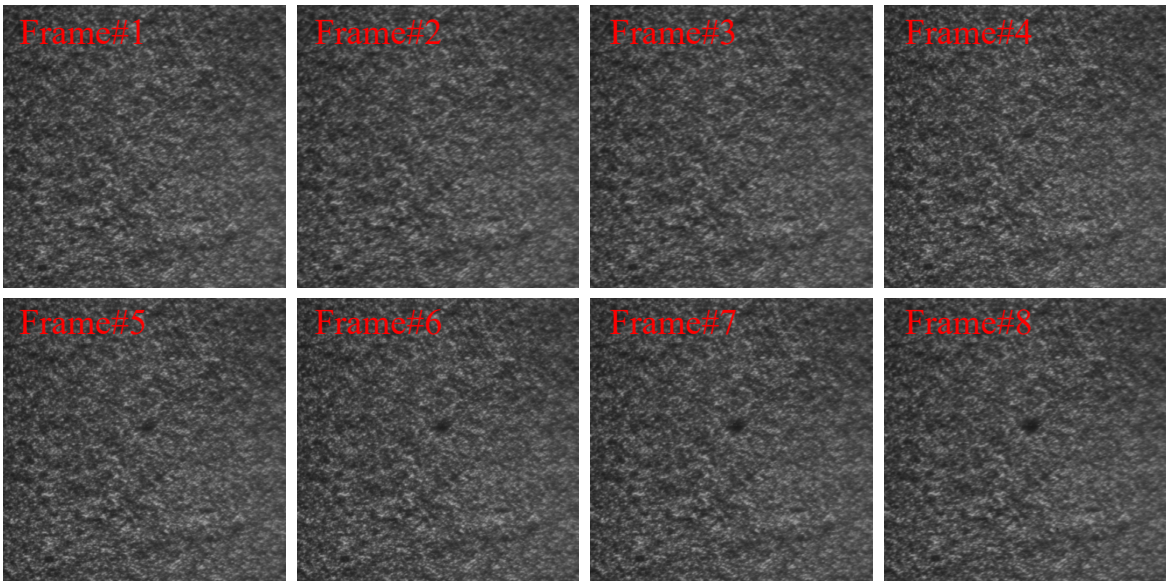

Figure 5.14: Processed zone evolution.

In Fig. 5.15, we plotted the raw melting pool width measured from 128 consecutive frames as the solid magenta curve and the filtered signal with different Kalman filter parameters. As illustrated in Fig. 5.15(a), as R increases from 0.01σ to σ, where σ is the deviation of the measurement signal, the filtered signal exhibits fewer variations. On the other hand, when Q increases, the filtered signal is noisier (Fig. 5.15(b)). The tuning of Q and R need to balance the signal variation and sensitivity

to abnormal signal. In the presented case, we may choose $R = \sigma$ and $Q = 0.1R$.

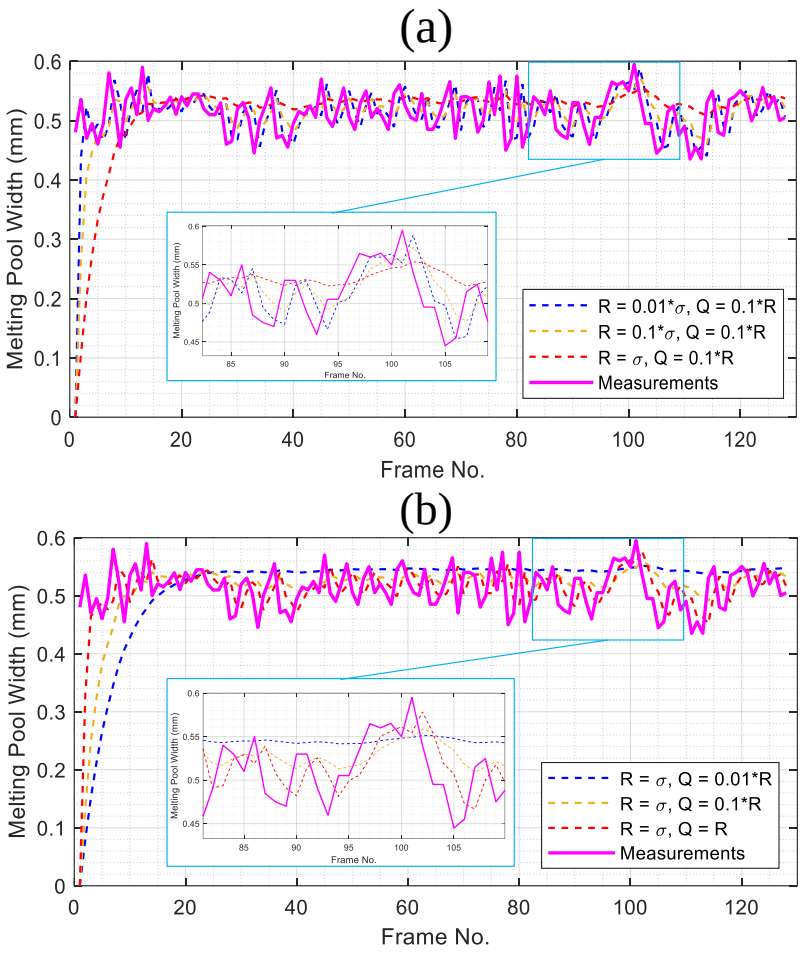

Figure 5.15: Melting pool width estimation with Kalman filter. (a) Tuning of measurement noise covariance R. (b) Tuning of process noise covariance Q.

Chapter 6

CONCLUSIONS AND FUTURE WORK

This dissertation developed an LPBF platform with a control-oriented mechatronic design for quality assurance. With multiple sensing modalities, the platform provides opportunities to access and control various process parameters and create high-fidelity numerical models.

Leveraging the feedback-centric features of the platform, we investigated control algorithms and data interpretation frameworks for attenuating mechanical vibrations, thermal transfer fluctuations, and laser-material interaction imperfections. We draw the following conclusions from our study and present some potential avenues for future work.

Loop-shaping Control for Laser Scanning Vibration Disturbance

We introduced an inverse-free FMSDOB for disturbance rejection for the galvo scanning process. By designing an FIR filter that inverts the plant dynamics locally at the needed frequency regions, the proposed scheme avoids explicit inverse plant models in conventional high-performance disturbance compensation schemes and is hence particularly useful for plants containing unstable zeros or when a stable plant inversion is prohibitively expensive over the entire frequency range. We provide both narrow- and wide-band filter designs to, respectively, reject disturbances concentrating at individual frequencies (e.g., vibration from system cooling fans) and spanning over wide bands (e.g., environmental vibration). Also discussed are methods for controlling the fundamental waterbed effect limitation. Under different complexity levels, simulation and experimentation on the galvo scanner platform in LPBF show significant performance gain for disturbance attenuation.

However, the performance improvement has only been verified on the scanner level but not on a part level. In the future, we can integrate the proposed scheme into the firmware of the developed LPBF platform to evaluate the part quality improvement. Specifically, this can be performed on two

different scales:

1. *Local melting pool scale*: Leveraging the coaxial monitoring system, we can analyze the motion of the laser spot and evaluate the level of local residual position error. We can utilize machine vision algorithms such as optical flow to obtain real-time motion direction for each frame.

2. *Global part scale*: Benchmark parts can be fabricated with and without the compensation scheme in the presence of vibration disturbance. An example of such a part is shown in Fig. 6.1. Features of different sizes, such as walls, holes, beams can be used to evaluate the dimension accuracy.

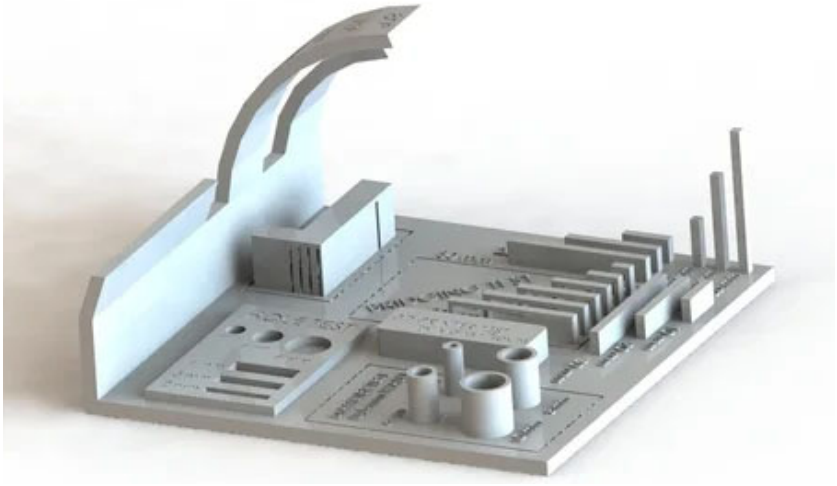

Figure 6.1: Benchmark part for evaluating 3D printer performance [3].

Multi-zone Control for Powder Bed Thermal Disturbance

We proposed a multi-zone control method for minimizing the powder bed temperature distribution error in the presence of part-geometry-induced thermal disturbance. Building upon the thermal transfer model of the preheating process, the control algorithm is a decoupled MIMO design.

Experimental results for PA12 preheating show that the residual powder bed temperature deviation is minimal when there is no thermal disturbance. When the initial thermal profile contains temperature disturbance transferred from previously processed layers, the proposed method outperforms the state-of-the-art SISO algorithm by providing lower maximum temperature overshoot and higher steady-state accuracy.

The impact of powder bed heating control on part quality should also be systematically studied in future to evaluate the effect size of the proposed scheme. Fig. 4.7 demonstrated a qualitative improvement regarding part geometry defect. The validation can be performed by both in-process monitoring and post-process measurement.

Specifically, using the proposed image analytics framework discussed in Chapter 5, we can extract the melting pool width from the captured images at different powder bed locations and evaluate its variance. Then the effect size of the proposed scheme can be evaluated by the difference of the variances with different control methods discussed. For post-porcess measurement, the effectiveness of the proposed control may be characterized by metrics such as microstructure of single layer part, the mechanical strength of test part such as tensile bar, and the dimensional accuracy of benchmark part. It is anticipated that with the multi-zone control method, the microstructure of the part should be more homogeneous, and the mechanical strength should be higher.

Image Analytics for Defect Detection and Fusion Process Control

A fundamental challenge for implementing online feedback control for the laser-material interaction process of LPBF is to establish the correlations between process measurements, process parameter settings, and quality metrics. This dissertation contributes to this issue by developing an image analytics framework for defect identification, part quality evaluation, and process signature filtering. A highlight of this study is that it targets the application of monitoring the LPBF of light-color low-melting-pool-intensity materials using the visual camera, which is a missing piece in existing literature.

Pioneering data analytics with morphological image processing, imaging field correction, and histogram equalization, we addressed key issues induced by contaminated optics, inconsistent

illumination, and low contrast between raw materials and the built parts in the noisy grayscale raw images. By utilizing graph-based segmentation, our approach leads to an innovation to isolate laser-fused materials from the unprocessed powder. By evaluating the isolated component, the dissertation proposed methods and features for detecting and predicting an overheating defect. We also discussed filtering the melting pool width with Kalman filter for implementing online feedback control.

One limitation of the proposed framework is the reliability of the image segmentation algorithm. The graph-based image segmentation algorithm requires careful parameter tuning to identify the processed zone. The same parameter set may not work well for all geometrical features. For example, one parameter set can accurately identify straight trajectory but not corner trajectory. We are currently investigating machine learning-based image segmentation method. Fig. 6.2 demonstrates the segmentation results using ResNet-50. More details are described in [79].

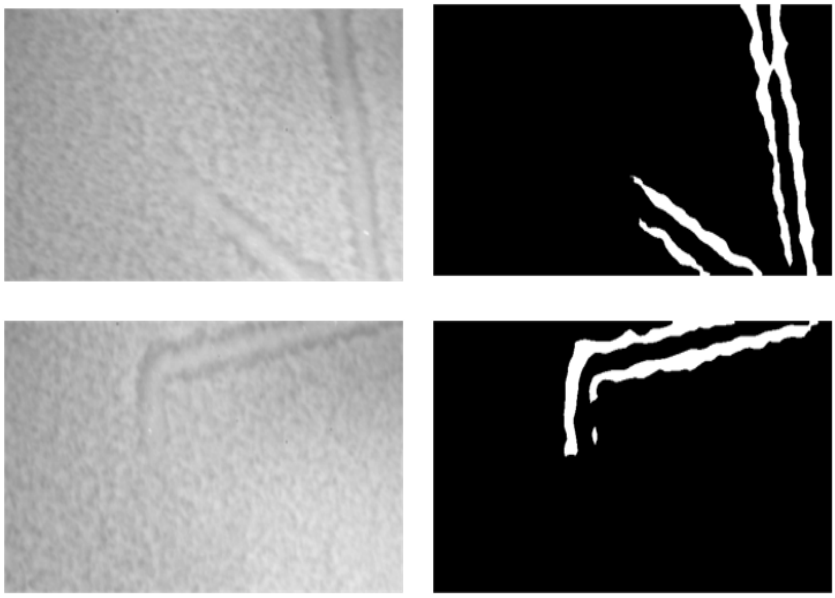

Figure 6.2: Processed zone identification result with the machine learning method.

Another path of future work is the validation of the proposed framework in real-time feedback control. This is contingent on efficient implementation of analytics algorithm on high-performance

FPGA. With the filtered melting pool width signal as feedback, we can use a PID controller to control the laser power. Specifically, recall Fig. 4.8 and Fig. 4.9, although the interlayer thermal disturbance can be attenuated by the proposed temperature control algorithm, it can not be fully rejected due to intrinsic physical limitation. The impact of the residual thermal disturbance on the current layer can be further rejected by in-process feedback control. Various test conditions should be used to validate the effectiveness of the image-based feedback control. For example, we may use different preheating temperatures, layer thickness, and scanning velocities.

BIBLIOGRAPHY

[1] L. Sun, T. Jiang, and X. Chen, "Adaptive loop shaping for wide-band disturbances attenuation in precision information storage systems," *IEEE Transactions on Magnetics*, vol. 53, pp. 1–13, May 2017.

[2] LaserFX, "How laser shows work - scanning system."

[3] MakerBot, "All in one 3d printer test."

[4] I. Gibson, D. Rosen, and B. Stucker, *Additive Manufacturing Technologies: 3D Printing, Rapid Prototyping, and Direct Digital Manufacturing*. Springer, 2nd ed., 2015.

[5] K. Bullis, "A more efficient jet engine is made from lighter parts, some 3-d printed," *MIT Technology Review*, 2013.

[6] D. Sheynin and Y. M. Bovalino, "A treat for the avgeeks: an inside look at ge's 3d-printed aircraft engine," tech. rep., GE, 2017.

[7] T. G. Spears and S. A. Gold, "In-process sensing in selective laser melting (slm) additive manufacturing," *Integrating Materials and Manufacturing Innovation*, vol. 5, no. 1, pp. 1–25, 2016.

[8] J.-P. Kruth, G. Levy, R. Schindel, T. Craeghs, and E. Yasa, "Consolidation of polymer powders by selective laser sintering," in *Proceedings of the 3rd International Conference on Polymers and Moulds Innovations*, pp. 15–30, 2008.

[9] T. Craeghs, F. Bechmann, S. Berumen, and J.-P. Kruth, "Feedback control of layerwise laser melting using optical sensors," *Physics Procedia*, vol. 5, pp. 505–514, 2010.

[10] M. Grasso and B. M. Colosimo, "Process defects and in situ monitoring methods in metal powder bed fusion: a review," *Measurement Science and Technology*, vol. 28, no. 4, p. 044005, 2017.

[11] D. Bourell, M. Leu, and D. Rosen, "Roadmap for additive manufacturing-identifying the future of freeform processing. the university of texas at austin, laboratory for freeform fabrication," *Advanced Manufacturing Center*, vol. 32, 2009.

[12] M. Mani, S. Feng, L. Brandon, A. Donmez, S. Moylan, and R. Fesperman, *Measurement science needs for real-time control of additive manufacturing powder-bed fusion processes*. CRC Press, 2017.

[13] N. Gupta, C. Weber, and S. Newsome, "Additive manufacturing: status and opportunities," *Science and Technology Policy Institute, Washington*, 2012.

[14] W. E. Frazier, "Direct digital manufacturing of metallic components: vision and roadmap," in *21st Annual International Solid Freeform Fabrication Symposium, Austin, TX, Aug*, pp. 9–11, 2010.

[15] M. Pavlov, M. Doubenskaia, and I. Smurov, "Pyrometric analysis of thermal processes in slm technology," *Physics Procedia*, vol. 5, pp. 523–531, 2010.

[16] J. Zur Jacobsmühlen, S. Kleszczynski, D. Schneider, and G. Witt, "High resolution imaging for inspection of laser beam melting systems," in *2013 IEEE international instrumentation and measurement technology conference (I2MTC)*, pp. 707–712, IEEE, 2013.

[17] F. Bayle and M. Doubenskaia, "Selective laser melting process monitoring with high speed infra-red camera and pyrometer," in *Fundamentals of laser assisted micro-and nanotechnologies*, vol. 6985, p. 698505, International Society for Optics and Photonics, 2008.

[18] Y. Gao, J. Xing, J. Zhang, N. Luo, and H. Zheng, "Research on measurement method of selective laser sintering (sls) transient temperature," *Optik*, vol. 119, no. 13, pp. 618–623, 2008.

[19] A. Wegner and G. Witt, "Process monitoring in laser sintering using thermal imaging," in *SFF Symposium, Austin, Texas, USA*, pp. 8–10, 2011.

[20] J. Hoffman and Z. Szymański, "Time-dependent spectroscopy of plasma plume under laser welding conditions," *Journal of Physics D: Applied Physics*, vol. 37, no. 13, p. 1792, 2004.

[21] A. Neef, V. Seyda, D. Herzog, C. Emmelmann, M. Schönleber, and M. Kogel-Hollacher, "Low coherence interferometry in selective laser melting," *Physics Procedia*, vol. 56, pp. 82–89, 2014.

[22] J. A. Kanko, A. P. Sibley, and J. M. Fraser, "In situ morphology-based defect detection of selective laser melting through inline coherent imaging," *Journal of Materials Processing Technology*, vol. 231, pp. 488–500, 2016.

[23] G. Guan, M. Hirsch, Z. H. Lu, D. T. Childs, S. J. Matcher, R. Goodridge, K. M. Groom, and A. T. Clare, "Evaluation of selective laser sintering processes by optical coherence tomography," *Materials & Design*, vol. 88, pp. 837–846, 2015.

[24] A. D. Lewis, N. Katta, A. B. McElroy, T. E. Milner, S. Fish, and J. J. Beaman Jr, "Understanding and improving optical coherence tomography imaging depth in selective laser sintering nylon 12 parts and powder," *Optical Engineering*, vol. 57, no. 4, p. 041414, 2018.

[25] H. Rieder, A. Dillhöfer, M. Spies, J. Bamberg, and T. Hess, "Online monitoring of additive manufacturing processes using ultrasound," in *ECNDT*, pp. 6–10, 2014.

[26] H. Wu, Z. Yu, and Y. Wang, "A new approach for online monitoring of additive manufacturing based on acoustic emission," in *International Manufacturing Science and Engineering Conference*, vol. 49910, p. V003T08A013, American Society of Mechanical Engineers, 2016.

[27] S. Clijsters, T. Craeghs, S. Buls, K. Kempen, and J.-P. Kruth, "In situ quality control of the selective laser melting process using a high-speed, real-time melt pool monitoring system," *The International Journal of Advanced Manufacturing Technology*, vol. 75, no. 5-8, pp. 1089–1101, 2014.

[28] T. Childs, C. Hauser, C. Taylor, and A. Tontowi, "Simulation and experimental verification of crystalline polymer and direct metal selective laser sintering," in *Proc. SFF Symp., Austin*, pp. 100–109, 2000.

[29] A. Foroozmehr, M. Badrossamay, E. Foroozmehr, and S. Golabi, "Finite element simulation of selective laser melting process considering optical penetration depth of laser in powder bed," *Materials & Design*, vol. 89, pp. 255–263, 2016.

[30] J. Smith, W. Xiong, W. Yan, S. Lin, P. Cheng, O. L. Kafka, G. J. Wagner, J. Cao, and W. K. Liu, "Linking process, structure, property, and performance for metal-based additive manufacturing: computational approaches with experimental support," *Computational Mechanics*, vol. 57, no. 4, pp. 583–610, 2016.

[31] E. Weissman and M. Hsu, "A finite element model of multi-layered laser sintered parts," in *1991 International Solid Freeform Fabrication Symposium*, 1991.

[32] W. King, A. T. Anderson, R. M. Ferencz, N. E. Hodge, C. Kamath, and S. A. Khairallah, "Overview of modelling and simulation of metal powder bed fusion process at lawrence livermore national laboratory," *Materials Science and Technology*, vol. 31, no. 8, pp. 957–968, 2015.

[33] K. Zeng, D. Pal, and B. Stucker, "A review of thermal analysis methods in laser sintering and selective laser melting," in *Proceedings of Solid Freeform Fabrication Symposium Austin, TX*, vol. 60, pp. 796–814, 2012.

[34] N. Hodge, R. Ferencz, and J. Solberg, "Implementation of a thermomechanical model for the simulation of selective laser melting," *Computational Mechanics*, vol. 54, no. 1, pp. 33–51, 2014.

[35] J. Mireles, C. Terrazas, S. M. Gaytan, D. A. Roberson, and R. B. Wicker, "Closed-loop automatic feedback control in electron beam melting," *The International Journal of Advanced Manufacturing Technology*, vol. 78, no. 5-8, pp. 1193–1199, 2015.

[36] D. T. Pham, K. Dotchev, and W. Yusoff, "Deterioration of polyamide powder properties in the laser sintering process," *Proceedings of the Institution of Mechanical Engineers, Part C: Journal of Mechanical Engineering Science*, vol. 222, no. 11, pp. 2163–2176, 2008.

[37] L. A. Slattery, N. L. Guckert, C. E. Shell, and R. R. Neptune, "The influence of post-sls-build annealing on nylon 11 material properties," in *Solid Freeform Fabrication Symposium*, 2012.

[38] S. Berumen, F. Bechmann, S. Lindner, J.-P. Kruth, and T. Craeghs, "Quality control of laser- and powder bed-based additive manufacturing (am) technologies," *Physics procedia*, vol. 5, pp. 617–622, 2010.

[39] X. Chen and M. Tomizuka, "A minimum parameter adaptive approach for rejecting multiple narrow-band disturbances with application to hard disk drives," *IEEE Transactions on Control Systems Technology*, vol. 20, pp. 408 – 415, Mar. 2012.

[40] J. Zheng and R. de Callafon, "Recursive filter estimation for feedforward noise cancellation with acoustic coupling," *Journal of Sound and Vibration*, vol. 291, pp. 1061–1079, Apr. 2006.

[41] R. Ehrlich, J. Adler, and H. Hindi, "Rejecting oscillatory, non-synchronous mechanical disturbances in hard disk drives," *IEEE Transactions on Magnetics*, vol. 37, pp. 646 – 650, Mar. 2001.

[42] J. Zheng, G. Guo, Y. Wang, and W. E. Wong, "Optimal narrow-band disturbance filter for pzt-actuated head positioning control on a spinstand," *IEEE Transactions on Magnetics*, vol. 42, pp. 3745 – 3751, Nov. 2006.

[43] M. Steinbuch, "Repetitive control for systems with uncertain period-time," *Automatica*, vol. 38, no. 12, pp. 2103–2109, 2002.

[44] C. Li, D. Zhang, and X. Zhuang, "A survey of repetitive control," in *Proceedings of 2004 IEEE/RSJ International Conference on Intelligent Robots and Systems*, vol. 2, pp. 1160–1166, 2004.

[45] I. Landau, A. Constantinescu, and D. Rey, "Adaptive narrow band disturbance rejection applied to an active suspension-an internal model principle approach," *Automatica*, vol. 41, no. 4, pp. 563–574, 2005.

[46] I. D. Landau, M. Alma, J. J. Martinez, and G. Buche, "Adaptive suppression of multiple time-varying unknown vibrations using an inertial actuator," *IEEE Transactions on Control Systems Technology*, vol. 19, pp. 1327 – 1338, Nov. 2011.

[47] I. D. Landau, A. C. Silva, T.-B. Airimitoaie, G. Buche, and M. Noe, "Benchmark on adaptive regulation—rejection of unknown/time-varying multiple narrow band disturbances," *European Journal of Control*, vol. 19, no. 4, pp. 237–252, 2013.

[48] A. Karimi and Z. Emedi, "$\mathscr{H}_\infty$ gain-scheduled controller design for rejection of time-varying narrow-band disturbances applied to a benchmark problem," *European Journal of Control*, vol. 19, pp. 279–288, July 2013.

[49] Q. Zheng and M. Tomizuka, "A disturbance observer approach to detecting and rejecting narrow-band disturbances in hard disk drives," in *2008 10th IEEE International Workshop on Advanced Motion Control*, pp. 254–259, 2008.

[50] X. Chen and M. Tomizuka, "Overview and new results in disturbance observer based adaptive vibration rejection with application to advanced manufacturing," *International Journal of Adaptive Control and Signal Processing*, vol. 29, no. 11, pp. 1459–1474, 2015.

[51] H. W. Bode, *Network Analysis and Feedback Amplifier Design*. van Nostrand, 1945.

[52] G. Stein, "Respect the unstable," *IEEE Control Systems Magazine*, vol. 23, no. 4, pp. 12–25, 2003.

[53] J. Doyle, B. Francis, and A. Tannenbaum, *Feedback control theory*. Courier Corporation, 2013.

[54] X. Chen, T. Jiang, and M. Tomizuka, "Pseudo youla-kucera parameterization with control of the waterbed effect for local loop shaping," *Automatica*, vol. 62, pp. 177–183, 2015.

[55] F. Ben-Amara, P. T. Kabamba, and A. G. Ulsoy, "Adaptive sinusoidal disturbance rejection in linear discrete-time systems–part i: Theory," *ASME Journal of Dynamic Systems, Measurement, and Control*, vol. 121, pp. 648–654, Dec. 1999.

[56] F. Ben-Amara, P. T. Kabamba, and A. G. Ulsoy, "Adaptive sinusoidal disturbance rejection in linear discrete-time systems–part ii: Experiments," *ASME Journal of Dynamic Systems, Measurement, and Control*, vol. 121, no. 4, pp. 655–659, 1999.

[57] R. A. de Callafon and C. E. Kinney, "Robust estimation and adaptive controller tuning for variance minimization in servo systems," *Journal of Advanced Mechanical Design, Systems, and Manufacturing*, vol. 4, no. 1, pp. 130–142, 2010.

[58] X. Chen and M. Tomizuka, "Selective model inversion and adaptive disturbance observer for time-varying vibration rejection on an active-suspension benchmark," *European Journal of Control*, vol. 19, pp. 300–312, July 2013.

[59] B. Haack and M. Tomizuka, "The effect of adding zeroes to feedforward controllers," *Journal of Dynamic Systems, Measurement, and Control*, vol. 113, no. 1, pp. 6–10, 1991.

[60] M. Tomizuka, "Zero phase error tracking algorithm for digital control," *Journal of Dynamic Systems, Measurement, and Control*, vol. 109, no. 1, pp. 65–68, 1987.

[61] J. Butterworth, L. Pao, and D. Abramovitch, "Analysis and comparison of three discrete-time feedforward model-inverse control techniques for nonminimum-phase systems," *Mechatronics*, vol. 22, no. 5, pp. 577–587, 2012.

[62] K.-S. Kim and Q. Zou, "A modeling-free inversion-based iterative feedforward control for precision output tracking of linear time-invariant systems," *IEEE/ASME Transactions on Mechatronics*, vol. 18, no. 6, pp. 1767–1777, 2012.

[63] J. S. Dewey, K. Leang, and S. Devasia, "Experimental and theoretical results in output-trajectory redesign for flexible structures," *Journal of dynamic systems, measurement, and control*, vol. 120, no. 4, pp. 456–461, 1998.

[64] D. S. Bernstein, *Matrix mathematics: theory, facts, and formulas with application to linear system theory*. Princeton University Press, 2005.

[65] K. S. Ramani, M. Duan, C. E. Okwudire, and A. Galip Ulsoy, "Tracking control of linear time-invariant nonminimum phase systems using filtered basis functions," *Journal of Dynamic Systems, Measurement, and Control*, vol. 139, pp. 011001–11, Jan. 2017.

[66] J. v. Zundert and T. Oomen, "On inversion-based approaches for feedforward and ilc," *Mechatronics*, vol. 50, pp. 282–291, Apr. 2018.

[67] D. Youla, J. d. Bongiorno, and H. Jabr, "Modern wiener–hopf design of optimal controllers part i: The single-input-output case," *IEEE Transactions on Automatic Control*, vol. 21, no. 1, pp. 3–13, 1976.

[68] V. Kučera, "Stability of discrete linear feedback systems," *IFAC Proceedings Volumes*, vol. 8, no. 1, pp. 573–578, 1975.

[69] K. Hirano, S. Nishimura, and S. Mitra, "Design of digital notch filters," *IEEE Transactions on Circuits and Systems*, vol. 21, no. 4, pp. 540–546, 1974.

[70] R. L. Burden and F. J. Douglas, *Numerical Analysis*. Cengage Learning, 8th ed., 2004.

[71] B. Wu and E. Jonckheere, "A simplified approach to bode's theorem for continuous-time and discrete-time systems," *IEEE Transactions on Automatic Control*, vol. 37, no. 1797-1802, 1992.

[72] X. Chen and M. Tomizuka, "Discrete-time reduced-complexity youla parameterization for dual-input single-output systems," *IEEE Transactions on Control Systems Technology*, vol. 24, no. 1, pp. 302–309, 2016.

[73] D. Wang and X. Chen, "A tutorial on loop-shaping control methodologies for precision positioning systems," *Advances in mechanical engineering*, vol. 9, no. 12, p. 1687814017742824, 2017.

[74] X. Chen, T. Jiang, D. Wang, and H. Xiao, "Realtime control-oriented modeling and disturbance parameterization for smart and reliable powder bed fusion additive manufacturing," in *Annual International Solid Freeform Fabrication Symposium-An Additive Manufacturing Conference*, 2018.

[75] G. Tapia and A. Elwany, "A review on process monitoring and control in metal-based additive manufacturing," *Journal of Manufacturing Science and Engineering*, vol. 136, no. 6, 2014.

[76] A. Shkoruta, S. Mishra, and S. J. Rock, "Real-time image-based feedback control of laser powder bed fusion," *ASME Letters in Dynamic Systems and Control*, vol. 2, no. 2, p. 021001, 2021.

[77] P. F. Felzenszwalb and D. P. Huttenlocher, "Efficient graph-based image segmentation," *International journal of computer vision*, vol. 59, no. 2, pp. 167–181, 2004.

[78] C. Boncelet, "Image noise models," in *The Essential Guide to Image Processing*, pp. 143–167, Elsevier, 2009.

[79] J. Xie, T. Jiang, and X. Chen, "Image processing and machine learning for melt pool segmentation in coaxial laser power bed fusion monitoring," in *IEEE American Control Conference (ACC)*, 2022 (under review).